Electrochemical Growth of CuBTC

Improving the synthesis toolkit through mechanistic understanding

Philipp Schäfer

Max-Planck Institute for Polymer Research

Dissertation zur Erlangung des Grades eines
'Doctor rerum naturalium (Dr. rer. nat.)' der Fachbereiche:
08 - Physik, Mathematik und Informatik
09 - Chemie, Pharmazie und Geowissenschaften
10 – Biologie
Universitätsmedizin
der Johannes Gutenberg-Universität

Max-Planck Graduate Center

I hereby declare that I wrote the dissertation submitted without any unauthorized external assistance and used only sources acknowledged in the work. All textual passages which are appropriated verbatim or paraphrased from published and unpublished texts as well as all information obtained from oral sources are duly indicated and listed in accordance with bibliographical rules. In carrying out this research, I complied with the rules of standard scientific practice as formulated in the statutes of Johannes Gutenberg-University Mainz to ensure standard scientific practice.

Dekan/in: [redacted]

1. Berichterstatterin/in: [redacted]

2. Berichterstatterin/in: [redacted]

3. Berichterstatterin/in: [redacted]

Tag der mündlichen Prüfung: 28.04.2017

Abstract

Metal-organic frameworks (MOFs) are crystalline, nanoporous materials that consist of metal cations and organic linker molecules with multiple functional moieties. The sheer infinite amount of possible metal ion-linker combinations makes MOFs in principle ready to be synthesized and tuned to desire for a large variety of applications as gas sensors, gas separation materials or as substrates for catalysis. Lack of synthesis predictability due to missing knowledge about the physicochemical processes during MOF production until now prevents their widespread industrial use.

One specific synthetic pathway, namely the electrochemical synthesis, promises fast and versatile MOF synthesis. The electrochemical potential gives an easily controllable parameter that can be exploited to tune material properties such as the crystal size to desire. To exploit the full range of possibilities the electrochemical synthesis offers, deep understanding of the molecular processes underlying MOF synthesis is necessary.

This thesis aims to gain this understanding on the archetypical MOF CuBTC. CuBTC, as one of only few MOFs, shows direct growth on the surface of the electrode used, a desirable property for facile production of i.e. gas separation membranes. Using a variety of physicochemical methods such as Raman spectroscopy, UV/VIS spectroscopy and cyclic voltammetry the mechanism of electrochemical CuBTC growth is investigated in depth. We investigate the oxidation mechanism of the copper electrode during the synthesis. To facilitate future development of surface-bound MOF coatings, we study the molecular-level reason for the on-surface growth of CuBTC. Finally, we are able to answer the question about the high rate of electrochemical MOF production compared to the classical pathway of homogeneous nucleation from solution.

We unravel a two-step oxidation process from copper to Cu^{2+} with cuprite as a necessary intermediate. Based on our insight we develop an easy fabrication method for patterned MOF coatings. Additionally, we investigate the specific interaction between the linker molecule BTC and electrified Cu surfaces. We find a strong potential-dependent adsorption of BTC that could explain why CuBTC specifically forms surface-bound MOF coatings contrary to the majority of electrochemically synthesized MOF materials. Lastly, we study the kinetics of CuBTC growth in solution. We find an unexpected inverse relation between the concentration of linker molecules and the growth rate of CuBTC. We develop a chemical reaction model including the formation of an overcoordinated BTC species that shows a good qualitative fit with the experimental results. Our model can yield an explanation for fast electrochemical growth in which the chemical equilibria are shifted to favor CuBTC growth instead of the overcoordinated species. Finally, we summarize our results and give possible directions for future research.

Zusammenfassung

Metall-organische Gerüstverbindungen (MOFs) sind kristalline, nanoporöse Materialien, die aus Metall-Kationen und polyfunktionellen organischen Linkermolekülen bestehen. Die nahezu unendliche Anzahl möglicher Metall-Linker Kombinationen ermöglicht es, MOFs für eine große Vielfalt an Anwendungen als Gassensoren, in der Gasseparation und der Katalyse zu synthetisieren. Ein Mangel an rationaler Planbarkeit der Synthese neuer Materialien liegt im fehlenden Wissen über die molekularen Prozesse während der Synthese begründet und verhindert verbreitete industrielle Anwendung von MOFs.

Die elektrochemische Synthese ist ein schneller Weg zur Produktion von MOFs. Das elektrochemische Potential ist ein einfach zu kontrollierender Parameter, der ausgenutzt werden kann, um die Materialeigenschaften (bspw. die Kristallgröße) nach Belieben zu beeinflussen. Um die Möglichkeiten der elektrochemischen Synthese besser auszunutzen, ist ein grundlegendes Verständnis der physikochemischen Prozesse, die dem MOF Wachstum zu Grunde liegen, nötig.

In dieser Arbeit möchten wir dieses Verständnis am archetypischen MOF CuBTC erlangen. CuBTC ist eines der wenigen MOFs, die direktes Wachstum auf der Elektrodenoberfläche zeigen. Die direkte Beschichtung von Substraten ist eine erstrebenswerte Charakteristik von MOF Synthesen um die einfache Produktion von, zum Beispiel, Gasseparationsmembranen zu ermöglichen. Mit Hilfe von Raman und UV/VIS Spektroskopie sowie zyklischer Voltammetrie wird der Mechanismus elektrochemischen CuBTC Wachstums untersucht. Wir untersuchen den Mechanismus der Oxidation der Kupferelektrode, welche dem MOF Wachstum zugrunde liegt. Um die Entwicklung weiterer oberflächengebundener MOF Beschichtungen zu vereinfachen, suchen wir nach dem chemischen Grund für das Wachstum von CuBTC auf der Oberfläche. Schlussendlich beantworten wir die Frage nach der im Vergleich zur klassischen Synthese hohen Geschwindigkeit der elektrochemischen Synthese.

Wir decken einen zweistufigen Oxidationsprozess von Kupfer zu Cu^{2+} mit Kuprit als Intermediat auf. Auf Basis unserer Entdeckung entwickeln wir einen einfachen Weg, strukturierte MOF Beschichtungen herzustellen. Anschließend untersuchen wir die spezifische Interaktion zwischen dem Linkermolekül BTC und Cu Oberflächen, an die eine Spannung angelegt wird. Wir beobachten eine potentialabhängige Adsorption von BTC, die eine Erklärung für das Oberflächenwachstum von CuBTC liefern kann. Zuletzt untersuchen wir die Kinetik des Wachstums von CuBTC in Lösung bei Raumtemperatur. Wir beobachten eine inverse Proportionalität zwischen der Konzentration des Linkers in Lösung und der Wachstumsgeschwindigkeit von CuBTC. Wir entwickeln ein chemischen Reaktionsmodell, das die Bildung einer überkoordinierten Kupfer-BTC Spezies beinhaltet und gute qualitative Übereinstimmung mit den experimentellen Daten zeigt. Unser Modell kann eine Erklärung für das schnelle elektrochemische Wachstum liefern. Während der elektrochemischen Synthese ist zu erwarten, dass die chemischen Gleichgewichte zu Gunsten der Bildung von CuBTC (im Vergleich zur überkoordinierten Spezies) verschoben werden. Abschließend fassen wir unsere Ergebnisse zusammen und geben Vorschläge für weiterführende Forschung auf dem Gebiet.

Table of contents

Chapter 1

Introduction

Rationally planned syntheses in which the outcome of a chemical reaction can be exactly predicted through use of the right reagents and synthesis conditions are the ultimate goal of synthetic chemistry. In organic chemistry molecular reaction mechanisms that form a new molecule out of the reagents are routinely investigated and discussed. While organic chemists to date still fight a certain degree of unpredictability in their syntheses (leading to unwanted side products or sometimes completely failed syntheses), the detailed knowledge about reaction mechanisms allows for a certain degree of rational synthesis planning.[1,2] Organic chemistry could therefore develop to be one of the backbones of today's society with large-scale industrial production facilities producing large varieties of chemical compounds with predictable purity and properties.

As a further development of organic chemistry, polymer chemistry has transformed our daily lives. Comparably simple chemical reactions to link organic molecules are used to build macromolecules with predictable chemical structure, connectivity and size. The choice of the monomer(s), length of the polymer chain and other chemical properties such as the termination of the polymer influences the properties of the material with regards to chemical/physical stability, malleability and even conductivity.[3] Their versatility and easy processability makes polymers perfect materials for the design of everyday objects. Polymerization chemistry is very well understood[4,5] and the development of entirely new synthesis methods has decreased considerably since the existing reactions can predictably produce almost any polymer material imaginable.

Coordination chemistry in which Lewis basic ligands form coordinative bonds with Lewis acidic metal cations is a similarly well understood field of chemistry. Based on the works of Alfred Werner in the late 19th and early 20th century we investigated and understood why different metal cations show differences in their preferred coordination geometry and how the chemical and geometrical structure of ligands influences the coordination compounds they form.[6,7] As with polymers and organic molecules, we are usually able to predict the structure and to a degree the properties of a new coordination compound that forms out of a specific combination of metal cation and ligand(s). Coordination chemistry has become another pillar of industrial scale chemical reactions with coordination compounds playing important roles as catalysts in organic and polymer synthesis.[8–10] Advances in i.e. dye-sensitized solar cells promise a bright future for coordination compounds as sensitizers for solar energy production.[11]

Coordination polymers are to coordination chemistry what conventional polymers are to organic chemistry. Coordination polymers are materials that are linked through repeating metal-coordination bonds. Single ligands can bind to multiple metal cations and can therefore link several units to each other.[12] One of the first examples of such a coordination polymer is Prussian blue (iron(III)-hexacyanoferrate(II)). In the late 1990s a new class of these coordination polymers was discovered, metal-organic frameworks (MOFs).[13]

MOFs are hybrid materials. They consist of metal cations that are bridged by organic molecules (linkers) with multiple, often symmetrically distributed moieties for coordinative bonds to the metal. Due to the order induced by the symmetry of the organic linker and the geometrical restrictions imposed due to metal-complex chemistry, MOFs are highly crystalline structures. The materials are nanoporous and thus offer interesting possibilities for applications in i.e. molecular sensing,[14] drug delivery,[15] gas sieving[16,17] or catalysis.[18–22] A wide variety of combinations between different metal ions and organic linkers can be combined into a sheer infinite number of possible frameworks that all exhibit unique properties.[23] The pore sizes, for example, can vary ($\approx$ 0.4 - 2 nm) depending on the choice of the linker or post-synthetic modifications.[24] The large variety in possible materials makes MOFs in principle ready to be tuned to desire for specific applications. Therefore, rational planning of MOF synthesis to target the production of very specific materials is a desirable goal to achieve.[25–27]

Despite their promising possibilities for industrial applications such as gas purification, gas separation/storage or catalysis[28] MOFs rarely find use in industrial facilities.[29] The issue preventing widespread use is that until now we cannot completely predict the outcome of a new MOF synthesis. Both the chemical nature of a newly synthesized material (crystal structure, pore size) and the mesoscopic properties such as crystal sizes and i.e. coverage of a substrate can still rarely be accurately predetermined. Our inability to reliably bring MOF crystals into the desired 'shape' limits our possibilities to exploit the theoretically infinite tunability of MOF materials for specialty applications like i.e. gas sensing or catalysis. One of the main reasons for this lack of predictability is that, contrary to i.e. polymers, the physicochemical processes during MOF synthesis and crystal growth are poorly understood.

Surface-bound MOF coatings are of special interest because of their potential applications as membranes in for example the separation of industrial gases[30,31] and liquids.[32] Recently, MOFs have also found increasing use in the fabrication of adsorption driven heat-pumps.[33,34] Coating surfaces with the MOF that is to be used as the adsorbent promises improved heat- and mass-transport properties of the functional device. For optimal loading of the surface with active material, strategies to produce binder-less MOF coatings are needed.[33] MOF coatings are also potentially interesting for molecular sensing applications.[14] A chip that is coated with a MOF specific for an adsorbate can be quickly read out i.e. electrochemically.[35] Universal synthesis strategies to produce surface-bound MOF coatings are, however, not available. Finding more reliable ways to synthesize MOFs on surfaces would open up new possibilities to use them in the above mentioned applications.

This thesis aims to shed light into the molecular-scale processes during MOF growth. We want to convert the insight gained into new tools for the synthetic chemist's toolkit that will expand the possibilities of MOFs to be used in functional devices. We base our investigation on the electrochemical synthesis route of a showcase MOF, CuBTC. The electrochemical route to CuBTC offers fast synthesis throughput, tunability of the final product through the electrochemical potential and the possibility to easily synthesize MOF surface coatings and as such is an interesting starting point. Our insight will help generalize these advantages specific to CuBTC to a larger variety of MOFs.

1.1 Structure of metal-organic frameworks

The crystal structures of newly synthesized MOFs are routinely investigated and unraveled using for example X-ray diffraction experiments.[36,37] Often, the crystal structure can be reduced to a specific secondary building unit (SBU) that describes the interaction between the linker and the metal cation as well as the symmetry of the metal-linker building unit. They can be understood as the analogue to a repeating unit in a polymer. These building units can be constructed by taking into account the preferred coordination geometry of the metal cation (quadratic planar, tetrahedral, etc.) and the angles and distances between the linker's functional moieties that bind to the metal cations.[38]

One example of such a SBU is the paddlewheel structure found in many MOFs that include aromatic carboxylic acids as the linker molecules and divalent metal cations.[39] Four carboxylic acids coordinate to two metal cations to form a dinuclear complex as shown in Figure 1.1 on the left. Each oxygen binds to one of the metal cations so that each cation is coordinated in a quadratic planar fashion by linker molecules (the vacant axial positions are commonly occupied by solvent molecules). As the linker molecules themselves have multiple binding moieties, they will be part of several of these building units and serve as their connector (see Figure 1.1 right). The symmetry (angle between the functional moieties and their amount per molecule) and length of the linker will determine how the SBUs can connect to each other. Knowledge of the SBU and their connectivity can therefore help predicting the crystal structures of MOFs and by that the shape and size of the pores in the framework. As the pores largely determine possible applications, the SBU concept is a valuable tool in the development new materials. Rationally planned syntheses that exploit the SBU concept to predict the structure of MOFs are called reticular syntheses.[40]

1.2 Metal organic framework synthesis

Commonly, MOFs are produced using a metal salt and the corresponding linker molecule in a suitable solvent. In the solvothermal synthesis, high temperatures and pressures usually have to be applied for long periods of time (sometimes a week or more) to produce a significant amount of material. Some syntheses with the aim of speeding up the MOF

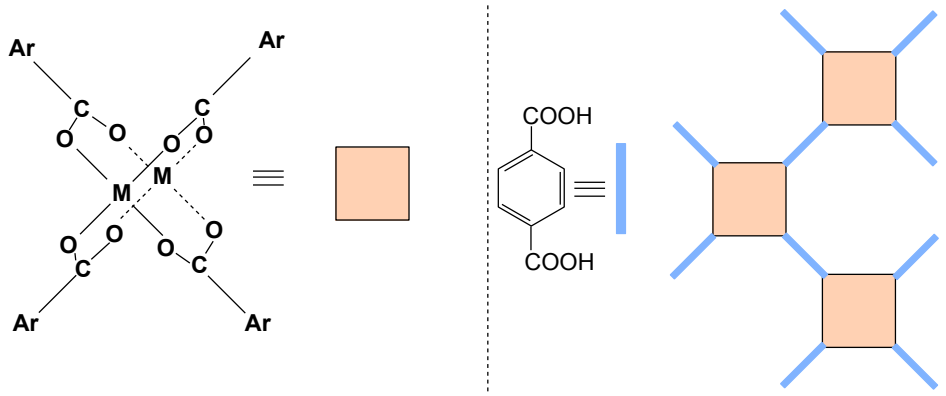

Figure 1.1 Scheme for the concept of secondary building units. left: Sketch of the molecular structure of a single paddlewheel building unit as found in many carboxylate-based MOF structures. Right: Schematic representation of multiple paddlewheel units interconnecting into a network based on the symmetry of the connecting linker.

formation using microwave irradiation or ultrasonication to trigger the crystallization have been developed.[41,42] After these solution based syntheses the material is usually obtained through centrifugation or suction filtering as a crystalline powder of varying dispersity. The crystal sizes range from hundreds of nm to tens of µm. While the so obtained material is suitable for general characterization of a new material, the powder itself is fairly difficult to bring into a more usable form, such as i.e. a gas-sieving membrane, post synthetically.

To produce more functional devices such as substrate bound MOF crystals, instead of dispersing the powder obtained from a classical synthesis on a substrate, the synthesis of the MOF itself is laid out from the beginning so that the crystals nucleate on the substrate. The produced materials are commonly called SURMOFs (Surface MOFs). SURMOF syntheses are often not continuous, involving multiple 'dipping' steps of the substrate into solutions of the linker, washing solvents and the metal ion precursors separately, a procedure commonly called layer-by-layer (LbL) synthesis.[43] Using this concept, some MOFs can be brought to i.e. specifically nucleate and grow on polymeric substrates such as acrylonitrile-butadiene-styrene.[44] Alternatively self-assembled monolayers (SAMs) of alkyl-thiols with functional terminations such as -COOH, -OH or -CF_3 have been shown to enable MOF nucleation on gold substrates.[45] On these SAMs the choice of thiol-termination strongly influences the structure of the first layer of adsorbed metal ions, leading to a preferential orientation of the grown crystals.[46] These methods of producing substrate-anchored MOF crystals usually involve labor- and time-intensive dipping, incubation and washing steps.

Other, less labor-intensive processes based on the solvothermal synthesis exist. These methods involve pre-aging a synthesis solution. In a first step an oversaturated synthesis mixture of linker and metal ions is subjected to conditions similar to the solvothermal synthesis for a short time (2 days - 2 weeks). The aged solution is obtained as a filtrate afterward. In a second step a substrate modified with for example a SAM as in the LbL approach[47] or a polydopamine coating[48] is immersed into the aged solution. The synthesis solution with the immersed substrate is again subjected to solvothermal synthesis conditions. Over multiple days a MOF film grows on the substrate. The synthesis times are usually in the range of a week and rapid throughput synthesis seems impossible. Additionally, the exact conditions for the pre-aging of the solution have to be developed for every synthesis separately.

In 2004 BASF patented a route to electrochemically produce MOFs.[49] Academic research in the field of MOF electrosynthesis followed.[50–52] It was found that the electrochemical synthesis could in the case of some MOFs be used to more easily produce MOF coatings on surfaces in one step. Additionally, the electrochemical synthesis significantly reduced the synthesis times down to tens of minutes, as opposed to days and weeks for the classical solvothermal synthesis.

On one hand, cathodic electrochemical synthesis protocols were developed. The group around Mircea Dincâ for example pioneered an approach using probases to trigger MOF growth.[53] The probase, such as a triethylammonium salt, is used as a proton 'sponge'. Using a negative electrochemical potential the probase can be deprotonated directly at the electrode (and the protons are reduced to hydrogen gas) which in turn enables the deprotonation of a carboxylic acid linker by the probase. The deprotonation itself is an important step in the activation of the linker molecule to enable it to coordinate to the metal cation that is present in the synthesis solution. Modulating the electrochemical potential allows modulation of the local pH in front of the electrode through the probase. With this approach Li and Dincâ were able to deposit stacked biphasic MOF films, comprised of two different MOF structures, on the same electrode in the same solution, by simply changing the electrochemical potential partway through the synthesis.[54]

On the other hand, in anodic electrosynthesis, the metal component of the desired MOF is provided as a pure metal electrode. The metal electrode is oxidized and dissolved at usually

very high electrochemical biases (up to 30 V) in a solution of the linker molecules. An electrolyte is added to the solution to support conductivity. The oxidation and dissolution of the metal provide the necessary metal ions in high concentrations directly in front of the metal surface. Ameloot et al. found that this anodic electrochemical route could not only produce a significant amount of material within only a few minutes of synthesis time but also that one specific MOF, CuBTC, seems to preferentially nucleate and grow on the surface of the copper electrode.[50] So far it is unclear why CuBTC, as well as for example UiO-66,[55] specifically show on-surface growth while the majority of other MOFs like ZIF-8 or MIL-100 grow in solution.[51] It was also found that the current density which can be influenced through the choice of the synthesis potential had a direct influence on the size of the grown crystals. Higher potentials lead to larger crystals, giving an easily controllable parameter that can be tuned during the synthesis to produce a desired material.[51]

Especially anodically synthesized CuBTC, a MOF consisting of Cu^{2+} ions and 1,3,5-benzene tricarboxylic acid, found a variety of uses in the fabrication of micro-structured MOF devices. Due to its on-surface growth, CuBTC could be grown in predetermined shapes and patterns in the micro- to millimeter length scale. For example, a copper net electrode was used to produce a high-surface area device that could function as an efficient gas-separation membrane,[56] whereas others have produced CuBTC out of the micro-structured copper patterns on a printed circuit board.[50] CuBTC can even grow into more elaborate meso-structures, such as a macroporous device (pore sizes in the range of a few µm) made out of MOF crystals in the size range of 100-200 nm (see Figure 1.2 for a schematic illustration).[57] These examples of CuBTC's ability to be brought into specific shapes, makes it an interesting case to study concerning its formation mechanism. Insight gained on the molecular mechanism of CuBTC growth can help inform the development of synthesis procedures that aim to emulate its unique properties (such as the on-surface growth). CuBTC is to date one of the work horses of the MOF community to understand the processes during the synthesis and the interaction with adsorbates.[58,59] It was one of the first MOFs to be synthesized solvothermally[60] and has dominated the literature on electrochemical MOF synthesis.[52]

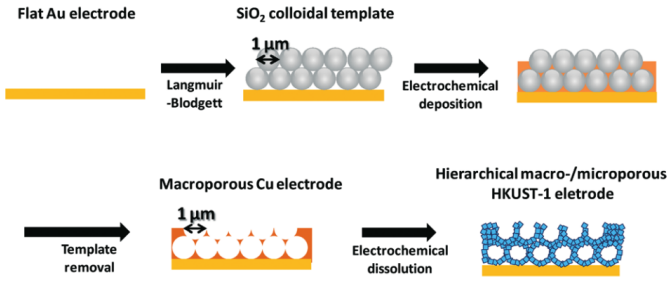

Figure 1.2 Schematic illustration showing the experimental steps performed for the synthesis of the hierarchical macro-/ microporous CuBTC. Adapted from [57] with permission of The Royal Society of Chemistry

1.3 The mechanism of metal-organic framework synthesis

To fully exploit the adaptability of MOFs we do not only need to understand their structure but we also need insight on how they form in the first place. Currently, many new MOFs are found through trial-and-error and their possible applications are usually only discovered afterward. If we aim to make MOFs a universal building block of functional devices in gas adsorption, catalysis and molecular sensing we need to be able to rationally plan the synthesis of these new materials. Additionally, we not only need to be able to predict and influence the chemical structure but also the mesoscopic properties of the material such as the crystal size distribution or the possibility to form surface-bound MOF coatings. Rational synthesis planning requires a deep and thorough understanding of the physico-chemical processes that govern MOF growth.

1.3.1 Understanding solvothermal crystallization processes

Until now, most of the research on MOF growth mechanisms is focused on unraveling the nucleation and crystallization dynamics during the solvothermal synthesis. MOFs show a large variety of different mechanisms for crystal growth.

Zeolitic imidazolate frameworks (ZIFs) are topological isomorphs of zeolites. They are composed of tetrahedrally coordinated transition metals (MN_4-units) and connect through imidazolate linkers. Many different ZIF structures have been found (>100).[61] What seems to combine all of them mechanistically is that the crystals form from amorphous cluster

intermediates. The formation of ZIF-8 has been studied using small- and wide-angle X-Ray scattering.[36] The material crystallizes from cluster-like intermediates with around 1 nm in size. This was confirmed by Patterson et al. who could follow the growth of ZIF-8 in in-situ TEM studies, finding that the addition of those intermediates is the rate-determining step of ZIF-8 formation in solution.[62] Comparably, microrods produced from ZIF-7 are assembled from even larger nano-building blocks (5.5 nm size).[63] ZIFs also generally show a fast formation of these intermediate clusters and the first nuclei, with further growth of the crystals being significantly slower. These findings match the general growth mechanism that has been found for zeolite structures themselves.[64]

The MIL (Material of the Insitut Lavoisier) class of metal-organic frameworks consists of octahedrally coordinated metal cations (such as V, Al, Cr or Fe) and dicarboxylic acids as linker molecules. The coordination sphere around the metal is often composed of four dicarboxylic acid linkers and two oxygen atoms, either from hydroxide (MIL-53) or oxygen (MIL-47). The SBUs connect into one-dimensional rhombic-shaped channels building at times flexible materials that can 'breathe' upon adsorption of molecules.[65] As they form the same structures with different metal cations, they have been investigated as to how the choice of metal ion influences the kinetics of crystal growth. The rate of MOF production for these materials has been found to follow the lability of the metals ($r(\mathrm{V}) > r(\mathrm{Al}) > r(\mathrm{Cr})$, with r the formation rate of the MOF), indicating that MOF growth is still very much connected to classical coordination chemistry.[66] Aluminium and aminoterephthalic acid can form different MOF structures (NH_2-MIL-101 and NH_2-MIL-53) depending on the chosen conditions such as solvent and temperature. Stavitski et al. could show that the formation of NH_2-MIL-101 proceeds through a structurally similar intermediate structure (NH_2-MOF-235).[63,67] The intermediate is the kinetic product of the precursors (Al and aminoterephthalic acid). At high linker concentrations in good solvents for the linker the formation of this intermediate and NH_2-MIL-101 afterward is favorable to the formation of the thermodynamically favorable product NH_2-MIL-53. Both kinetic products can, however, be transformed into the NH_2-MIL-53 at high temperatures. The intermediate itself could be quenched, isolated and investigated. This study indicates the importance of understanding the interplay between the components of a synthesis solution. From this knowledge it is possible to predict the outcome of a synthesis based on the conditions used and different MOFs can

be synthesized from the same starting materials. The formation of many MIL-type MOFs also occurs through an amorphous intermediate/precursor as has been shown for MIL-89(Fe) (with a muconic acid linker)[68] and MIL-53(Fe).[69]

Terephthalic acid (BDC) is a versatile linker that not only forms MIL-type structures but is also used as a building unit for one of the first-reported frameworks, MOF-5, which forms from zinc and BDC.[13] The formation of MOF-5 has been investigated using in-situ time-resolved light scattering. Similar to the ZIF-family, MOF-5 nucleation is fast while the crystal growth is slow in comparison.[70] In-situ AFM was used to follow the growth of MOF-5 crystal facets and it was found that the crystal facets grow in a spiral-like fashion with doubled building units (ZnO_4-clusters) adding onto the existing crystal at a kink site.[71]

The addition of complete building units to an existing crystal has also been observed for CuBTC. In-situ AFM shows a step-by-step growth onto existing CuBTC facets. The height of the emerging steps matches the height of a single CuBTC paddlewheel unit, contrary to attachment of two building units seen for MOF-5.[72,73] CuBTC also shows differences to the previously discussed MOFs as nucleation persists throughout the whole growth phase of the crystals and the kinetics of the synthesis are nucleation dominated.[74,75] CuBTC is also the MOF most commonly produced using the LbL synthesis approach mentioned earlier. The LbL-approach allows to investigate the coated substrate after every growth cycle. Using ex-situ AFM after varying amounts of growth steps allowed Ohnsorg et al. to identify the growth of CuBTC to follow a Volmer-Weber growth mechanism on the surface of a self-assembled thiol monolayer on gold.[76] They observe that higher synthesis temperatures promote the formation of coatings with less surface-roughness. In addition they see that the temperature has an effect on the preferred orientation of the crystals on the solution. Care has to be taken in transferring the insight gained here directly to the homogenous solvothermal growth. The surface acts as a nucleation site and as such the mechanism of the LbL growth might not be directly transferable to the solvothermal synthesis.

The LbL approach has also been realized using flow cells that allow an exchange of the solution over the substrate in-situ. Using quartz crystal micro balance and surface plasmon resonance it was found that while the synthesis of CuBTC on the surface of a gold substrate modified with a thiol-SAM is possible using copper acetate as a copper source, copper nitrate does not promote crystal growth.[77,78] The reason was found in the fact that copper acetate

already exhibits a paddlewheel structure in solution and can therefore add onto the existing crystal surface as a complete copper-acetate SBU during the copper-addition steps of the synthesis. Upon introducing the BTC linker, the acetate ligand gets replaced by BTC that can now serve as the anchor point for the next copper addition step. Copper from copper nitrate seems to not be able to attach to the existing MOF facets on the crystal surface without the BTC linker present, as its solution structure cannot easily transform into the paddlewheel structure without BTC present. Additionally, the (100) facet of CuBTC grows significantly slower than the (111) facet. This is supported by the fact that CuBTC generally quickly grows into octahedral crystals with only (111) facets.

Our brief review above shows that most of the insight gained on the formation of MOFs is focused on crystallization and nucleation. As the commonly used scattering techniques (X-ray and light scattering) can only detect particles in the nanometer range, molecular-level insight into the chemical processes during the synthesis is rare. The insight we do have on the molecular scale shows that CuBTC in general grows by adding complete building units to the outside of an existing crystal.

1.3.2 The electrochemical CuBTC growth mechanism

The electrochemical synthesis has so far not found widespread use in MOF fabrication. The previously detailed advantages of short synthesis times, on surface-growth of (at least some) MOFs and in-situ control over the synthesized material (crystal size and linker-choice) through the electrochemical potential, however, make the electrosynthesis of MOFs a promising field for device fabrication. The issue that prevents the more general use of ec synthesis lies in the generalization of these situational advantages to the whole library of available MOF structures.

Similar to the solvothermal synthesis, we lack knowledge about the molecular processes during electrochemical MOF growth. CuBTC i.e. shows the often-desired on-surface growth and finding the molecular origin of electrochemical surface-growth would facilitate the search for more easily produced MOF films.

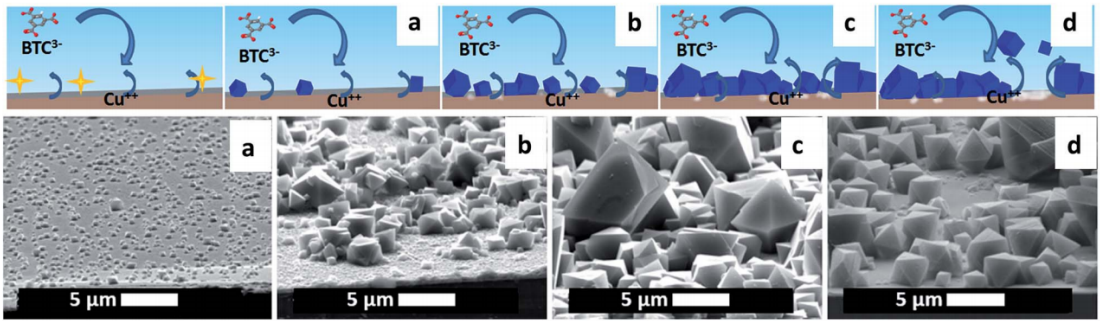

Figure 1.3 Proposed mechanism of MOF anodic electrodeposition and SEM pictures, taken at a 75° angle with the normal, of the four phases: **(a)** initial nucleation, **(b)** growth of islands, **(c)** intergrowth and **(d)** detachment. Copper-coated wafer substrate, 2 V vs. Pt counter electrode, after 10 s, 10 min, 60 min and 125 min. Reproduced with permission from [79] - Published by the Royal Society of Chemistry.

Only few scientists have so far tried to unravel the mechanism of electrochemical CuBTC growth. Initially, it was theorized that the mechanism underlying anodic MOF production is a sequence of metal oxidation and dissolution and subsequent linker coordination in solution. The crystals can then deposit onto the electrode, as the growth is confined to a thin layer in front of the electrode.[51] This would mean that in its essence anodic synthesis follows the same mechanism as the conventional solution-based route discussed before. However, the key differences in reaction rate and on-surface MOF growth cannot be explained by this simple assumption.

Campagnol et al. have identified four stages to anodic CuBTC growth on copper-coated wafer substrates.[79] They differentiate between initial nucleation (a), growth of islands (b), intergrowth (c) and detachment of crystals (d, see Figure 1.3). Electrochemical quartz micro balance studies indicate a potential-dependent induction period for the nucleation in Phase **(a)** that Campagnol attributes to the time needed to build up a critical concentration of Cu^{2+} in front of the electrode.

In Phase **(b)**, the island growth stage, they observe, on top of the growth of existing nuclei, that further nucleation seems to be concentrated around already existing crystals. They attribute the concentrated nucleation to a higher current density around existing crystals, locally increasing the Cu^{2+} concentration above the critical nucleation concentration. Phase **(c)**, the intergrowth phase, shows the for CuBTC observed self-closing nature of the electrochemical synthesis. Since CuBTC is an electric insulator, crystals attached to the surface passivate

parts of the electrode. CuBTC can only grow where there is significant concentration of Cu^{2+} available, meaning it will preferentially grow on the non-passivated parts of the electrode surface, since this is where most of the Cu^{2+} is produced. Therefore, over time, the electrode area will start closing off leading ultimately to the formation of a compact, insulating layer of CuBTC. During the last step, phase **(d)**, crystals start to detach from the surface. The exact reason behind this detachment is unknown. Campagnol et al. attribute the detachment to the crystals falling off as the Cu support underneath the CuBTC slowly dissolves to form more Cu^{2+}.

Most of Campagnol's conclusions also only concern the growth of crystals on the mesoscale. To fully understand electrochemical CuBTC synthesis we need to gain molecular level insight on the exact oxidation mechanism of copper to Cu^{2+} and the assembly of the linker and the copper ions. Finding the chemical reason behind the on-surface growth of CuBTC will support the engineering of MOFs toward applications in i.e. thin-film devices. Understanding the origin of the vastly increased speed of electrochemical MOF synthesis can inform improvements in solvothermal synthesis protocols as well as guide the scale-up of MOF production. In this thesis, we will provide the necessary molecular-scale insight and answer these questions to expand the synthetic toolkit for the production of functional MOF materials.

1.4 Thesis outline

This thesis sets out to give a comprehensive insight into the molecular-level physicochemical processes during electrochemical CuBTC synthesis. We explain the redox chemistry during the initial oxidation of copper and find a reason for the on-surface nucleation and growth of CuBTC. Finally we present new insight into the solution chemistry of CuBTC synthesis which helps answer the question about the rapid growth of electrochemically synthesized CuBTC when compared to classical synthesis routes.

Chapter 2 gives an introduction into the physico-chemical principles and methods used in the course of this work and their significance to our scientific questions. The methods we use are cyclic voltammetry, in- and ex-situ optical as well as vibrational spectroscopies and scanning electron and atomic force microscopies. We show the characterization of a typical CuBTC

sample, synthesized using the electrochemical pathway, which will serve as a basis for the discussion of the later results.

Chapter 3 presents our results on the oxidation mechanism that yields Cu^{2+} from the copper electrode. We will show that a Cu(I) oxidation state in the form of Cu_2O is a necessary intermediate to ultimately produce Cu^{2+}. Chemically disabling pathways to produce Cu_2O leads to a failure to produce CuBTC. We use the insight gained to develop an easy procedure to produce patterned MOF coatings.

In chapter 4 we investigate the molecular-level interaction between BTC and the copper electrode under electrochemical conditions using cyclic voltammetry and vibrational spectroscopy. We see the potential-dependent formation of an adsorbed layer of BTC on the surface of copper. The closer the applied potential is to the synthesis potential of CuBTC, the denser the adsorbed BTC layer becomes. Above the synthesis potential of CuBTC, we observe the slow transition of this adlayer into a surface bound coating of CuBTC. We conclude that the strong adsorption of a BTC layer onto the Cu surface not only helps with rapid nucleation of CuBTC in front of the electrode but that the BTC self-assembled monolayer could also serve as a seeding layer onto which the first CuBTC crystals nucleate. We propose using other metal-linker pairs that show similar strong specific interactions to narrow down the search for other surface-bound MOFs.

In chapter 5 we use kinetic data obtained through UV/VIS absorption spectroscopy during the homogeneous nucleation/growth of CuBTC from copper-nitrate and BTC to gain insight into the coordination chemistry between Cu^{2+} and BTC and into the kinetics of CuBTC growth. We find that, contrary to intuition, high concentrations of BTC have an adverse effect on the rate of CuBTC growth. Based on our observations, we propose a chemical reaction sequence including an overcoordinated, slow-reacting Cu-BTC species that hinders CuBTC growth at high linker-concentrations. We numerically simulate our model and find qualitative agreement between the model and the experimental data. We synthesize CuBTC under different concentration conditions both solvothermally as well as electrochemically. While we do not find significant difference in the mesoscopic properties of the solvothermally produced samples, the electrochemical synthesis shows differences in crystal size and surface coverage of the synthesized material. The properties of the synthesized material can be explained with our reaction model. Our results help answer the question about the rapid

growth of electrochemically synthesized CuBTC and help inform further development of solvothermal synthesis protocols.

Chapter 6 summarizes our results and finishes by providing guidelines for possible future research.

Chapter 2

Principles and techniques

In this chapter, we will briefly explain the physicochemical principles and techniques used in chapters 3-5. We will show the procedure for the electrochemical synthesis of a CuBTC sample and show a characterization of this sample which will serve as a basis for discussion in later chapters.

2.1 Electrochemistry

The field of electrochemistry studies chemical changes induced by an electrical current or the production of electrical current by chemical reactions. An electrochemical system typically consists of two electron conducting electrodes and an ionic/mass conducting electrolyte. A bias applied between the two electrodes can trigger spatially separated reduction/oxidation reactions. The electrode at which reduction reactions take place is called a cathode, the electrode at which oxidations take place is called an anode.[80,81]

2.1.1 Electrode potential and electrochemical equilibrium

The electrode potential is the fundamental concept of electrochemical research. When a potential is applied to an electrode the Fermi level of the electrode is changed. The Fermi level denotes the electronic energy level that, at thermodynamic equilibrium, has a 50%

probability of being occupied. Therefore it is also equal to the energy needed to transfer an additional charge from vacuum into the solid phase.

As the electrode potential is changed, and thus the Fermi level of the electrode changes, chemical changes at the electrode and in the surrounding medium can be triggered. Redox reactions, in which a chemical species either loses an electron (oxidation) or gains an electron (reduction) are one of these possible processes.[80] The electrode supplies/takes up the necessary electrons for the reaction. The thermodynamic equilibrium condition at a specific electrode potential E can be described using the Nernst equation

$$E = E^0 - \frac{RT}{nF} \sum v_i \ln a_i \tag{2.1}$$

with v_i the stochiometric numbers (positive for products/reduced species and negative for reagents/oxidized species) of the active species, a_i the activities of the active species, R, T, n and F the universal gas constant, the temperature, the amount of electrons transferred during the reaction and the Faraday constant respectively. E^0 is the standard reduction potential for the specified reaction which is usually measured and reported versus a normal hydrogen electrode (NHE), with all species at unit activity. The Gibbs free energy difference for the reaction, relative to the NHE reference reaction, is given by

$$\Delta G^0 = -nFE^0 \tag{2.2}$$

For every applied potential E a specific chemical equilibrium between the chemical species will establish at the interface between the electrolyte and the electrode in order to fulfill equation (2.1).[80]

Molecular adsorption/desorption or reorientation processes can also be triggered using the applied potential.[82] An adsorption process is generally connected to at least a partial charge transfer between the molecule and the metal:

$$A^z \longleftrightarrow A_{ad}^{z+\lambda} + \lambda e^- \tag{2.3}$$

With A^z a molecule in the electrolyte with charge z, $A_{ad}^{z+\lambda}$ the adsorbed molecule and λ the charge transferred during the adsorption process. λ can be a positive or negative rational number and z a positive or negative integer (or 0). Conceptually, adsorption/desorption or

reorientation can therefore be understood in the same way as redox reactions. As partial charges are transferred, the applied potential will influence the equilibrium between the free species A^z and the adsorbed species A_{ad}.[80]

As the thermodynamic equilibrium is formed at the electrode/electrolyte interface a certain amount of electrons needs to be transferred to/from the electrode. In order to keep the overall charge balance of the system the electrons will originate from a counter-reaction at the second electrode. The electrons transferred through the connecting wires between the electrodes can be measured as a current. Most electrochemical measuring techniques are based around measuring the current originating from the processes at the electrochemical interface at an electrode of interest upon changing the applied potential. The opposite experiment is also possible, where the system is forced to supply a certain current and the effective potential at the electrode of interest is measured, giving insight into the thermodynamics of the reactions taking place.

Large currents passing through an electrode can change its effective potential. In a two-electrode system, the potential is applied between the same two electrodes between which the current flows. This leads to inaccuracies in the determination of the actual potential at the electrode of interest (commonly called the working electrode, WE). As the potential is set as a bias between the electrodes, changes in the electrode potential of the second electrode due to large currents will also influence the potential at the WE. The potential reference point becomes undefined and absolute potential information is lost.[80] To overcome this limitation, which is especially prevalent in electrode dissolution reactions with high currents, a three-electrode setup can be used. Here, three electrodes are introduced into the electrochemical cell: the WE, the processes at which we want to study. The counter electrode (CE) through which the current flows and a reference electrode (RE) against which the potential of the WE is set. As now current and potential measurements are separated from each other, the potential at the WE can be accurately determined.

In this thesis all potentials are reported versus a copper reference electrode as the MOF literature on electrochemical CuBTC growth mostly uses copper reference/counter electrodes. The potential of the pseudo Cu reference is around 0.21 V vs NHE.

2.1.2 Cyclic voltammetry

Cyclic voltammetry is one of the primary electrochemical measurement methods. It gives information about the thermodynamics of the investigated system as well as the kinetics of the electron transfer processes and is therefore usually the starting point of any in-depth electrochemical characterization.[81] The principle behind cyclic voltammetry is that the potential of the WE is scanned at a constant rate $v = \frac{dE}{dt}$, with E the applied potential and t the time, back and forth between a lower and an upper vertex potential. The current I passing through the WE is measured over time and then plotted versus the applied potential.[80] Peak positions in the current vs potential curve give indication about the energetics of electron transfer processes, electrochemical modifications of the electrode itself (such as oxidation) or molecular adsorption/desorption/reorientation. If the triggered process is a simple reduction/oxidation reaction of a chemical species in solution, a current peak forms due to diffusion limitation. The chemical species being consumed in the electrochemical interface has to diffuse from the bulk to the electrode. At some point the diffusing supply cannot keep up with the amount consumed at the electrode leading to a drop in the current. For processes involving a change of the electrode itself, such as surface oxidation of the metal, peaks can form due to a passivation of the metal surface by the formed oxide. When the coating that is formed is non-conductive the current drops as more and more electrode area is passivated.

2.2 Spectroscopy

Spectroscopy, the study of the interaction between electromagnetic radiation and matter, is a valuable tool to understand molecular processes without being able to directly visualize them. Vibrational spectroscopies, such as Raman spectroscopy, allow identification of inorganic materials and organic molecules. In organic molecules specific moieties can be distinguished and through changes in the energies of vibrational modes we can learn about the interaction of these moieties with other molecules/materials. Optical spectroscopy in the ultraviolet/visible (UV/VIS) range gives us access to the valence electronic states in transition metal complexes (and organic molecules) as UV/VIS light can excite electronic transitions.[83] The electronic

states contain information about i.e. the coordination sphere (number of ligands, ligand shell geometry) around the central metal ion in transition metal complexes. UV/VIS spectroscopy therefore allows us to investigate the ligand shell of these complexes.

As MOFs are the result of specific interaction between transition metal centers and organic moieties both kinds of spectroscopies yield important insight into the molecular processes during MOF formation. We use Raman spectroscopy to identify CuBTC in synthesis products to investigate the interaction of BTC with its surroundings (see Chapters 3 and 4). In addition UV/VIS spectroscopy gives us valuable insight into the coordination sphere around the Cu^{2+} centers during the synthesis of CuBTC (see Chapter 5). Here, we provide a basic theoretical background for both techniques that will help understand the results we present later.

2.2.1 UV/VIS Absorption spectroscopy

When matter absorbs light in the UV/VIS range usually electrons are being excited into a higher electronic energy state.[84] As such, UV/VIS spectroscopy is able to probe, for example, the energetic difference between the HOMO (highest-occupied molecular orbital) and the LUMO (lowest unoccupied molecular orbital) in a chemical species. In transition metal complexes the energetics of the HOMO-LUMO gap are mainly determined by the geometry and composition of the ligand sphere around the central metal ion. A conceptual model to envision the energy levels involved in the HOMO-LUMO transition is crystal field theory (CFT).[85,86]

In essence, CFT describes the breaking of degeneracies of electron orbital states in transition metal ions upon spatial approach of complexing ligands. The five-fold degenerated outer d-orbitals of transition metals split their energy levels due to a geometrically distributed static electric field produced by the ligands. This static electric field originates from the negative charge of the ligands - or in the case of an uncharged ligand (such as water), the disturbing field originates from lone electron pairs on the ligands.

Depending on the electronic properties of the ligand, such as i.e. the energy levels of the electronic orbitals, and the geometry in which the ligand shell assembles around the central metal cation, the extent of the d-orbital splitting and how the orbitals split will change. Figure

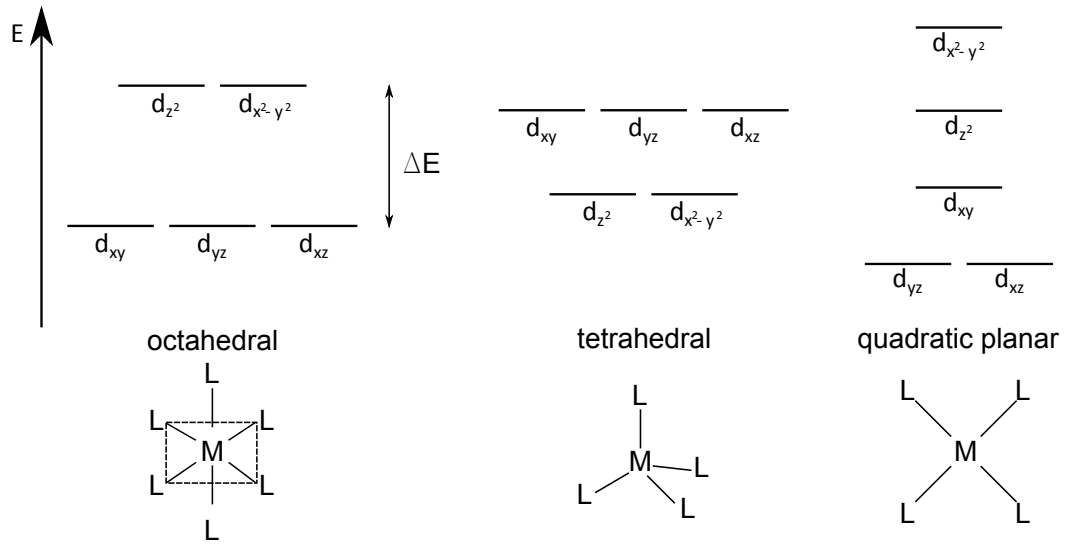

Figure 2.1 Scheme for the d-orbital splitting in transition metal complexes for commonly observed ligand shell geometries (octahedral, tetrahedral and square planar). Below the energy diagrams, a schematic representation of the complexes is shown with M being the metal center and L being the ligands coordinating to the metal.

2.1 summarizes three common ligand shell geometries and shows the respective d-orbital splittings.

The energy difference ΔE between the d-orbitals is usually in the energy range of UV and visible light. If the d-orbitals of a transition metal complex are not completely filled with electrons (as is the case for the d9-ion Cu^{2+} in CuBTC), an electron can be excited from the highest occupied d-orbital into an unfilled orbital. As a specific example: For a Cu^{2+} ion in the quadratic planar configuration in the electronic ground state, the four lowest d-orbitals will each be filled with two electrons (d_{yz}, d_{xz}, d_{xy}, d_{z^2}). The last orbital ($d_{x^2-y^2}$) will be filled with a single electron. A photon with an energy that matches the energy difference of the $d_{x^2-y^2}$ orbital to one of the lower lying orbitals can be absorbed by the complex and excite an electron into the $d_{x^2-y^2}$ level. This can be measured in a UV/VIS experiment as an absorption.[7]

As the exact energetics of the ligand field depend on the metal ion (the element and oxidation state), the coordination geometry of the ligand shell and on the chemical nature of the ligand, the UV/VIS absorbance of complexes with different ligand shells are different. We use

this fact to investigate coordination chemistry of Cu^{2+} and BTC in solution using UV/VIS spectroscopy in chapter 5.

The absorbance $A(\lambda)$ of a sample at a specific wavelength is given by Beer's law.[83]

$$-\log_{10}T = \quad A(\lambda) = d \cdot c \cdot \varepsilon(\lambda) \tag{2.4}$$

$$T = \qquad \frac{I_t}{I_0} \tag{2.5}$$

with T the transmittance of the sample (the quotient of the intensity of light transmitted through the sample I_t and the light transmitted through the standard I_0), d the pathlength through the absorbing medium, c the concentration of a chemical species in the probed medium and $\varepsilon(\lambda)$ the molar absorbance coefficient of the chemical species at the chosen wavelength. ε is a material property. Absorption of multiple chemical species can be summed up to determine the total absorption of a sample if there are no interactions between the different absorbing species. This assumption for example does not hold, when there is energy transfer between the molecules (as in Förster resonant energy transfer).

We use UV/VIS absorption spectroscopy in chapter 5 to get kinetic information about the formation of CuBTC in solution. CuBTC itself has a strong absorption band around 710 nm due to a d-d transition as explained above. Additionally an absorption edge around 350 nm due to a direct charge transfer from the ligands to the metal can be observed.[44,87,88] The absorption spectrum is different to the spectrum of a copper nitrate precursor (λ_{max} = 800 nm) that is commonly used for the solvothermal synthesis of CuBTC. The change in the ligand shell between the solvated Cu^{2+} ion (with usually 4-6 coordination sites) and the dinuclear paddlewheel complex leads to the described change in the absorption spectrum. The spectrum can therefore be used to identify the two different chemical species and even determine their concentrations according to (2.5), which builds the foundation for our kinetic investigation.

Instrumentation

The UV/VIS spectra were measured using an integration sphere setup on a Perkin Elmer Lambda 900 spectrometer. The integration sphere is necessary as growing CuBTC crystals rapidly approach sizes in the range of several hundred nm and thus show increasing elastic

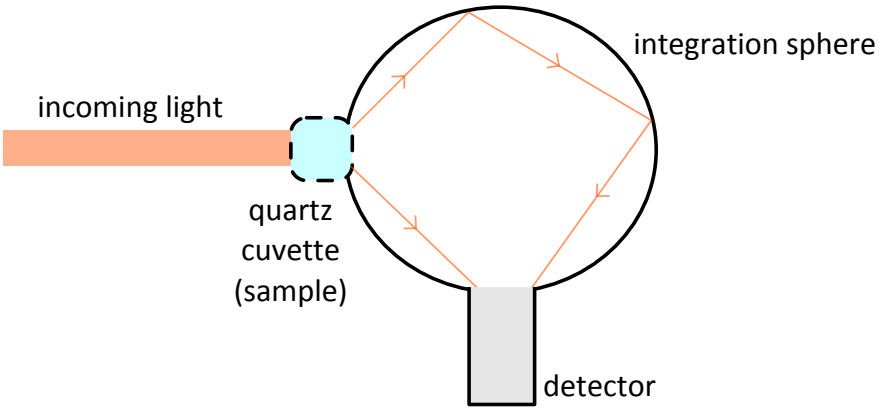

Figure 2.2 Scheme of the operation principle of the integration sphere used for UV/VIS absorbance experiments.

scattering of light. This elastic scattering is wavelength dependent (lower wavelengths are scattered more strongly) and dependent on the size of the particles (larger particles scatter light more strongly). As the elastic scattering occurs in first approximation almost spherical in all directions, in a UV/VIS absorbance experiment particles in size ranges larger than $\approx$ 50 nm will show an apparently higher absorbance than would be expected from pure electronic excitations. The additional absorbance stems from the light scattered away from the detector. To best eliminate the scattering contribution to the measured absorbance of the sample, an integration sphere is used to collect all of the light scattered and transmitted in an almost 180° cone behind the sample cuvette. The sphere redirects the light through diffuse reflection into the detector as shown in Figure 2.2. Still, not all of the scattered light is collectible and as such the data measured from such turbid solutions will inherently show an effective absorbance that is a combination of the absorption due to electronic transitions in the material and elastic scattering. The larger the particles in the measured solution, the larger the absolute induced error will be.

2.2.2 Raman spectroscopy

In 1930 the Indian physicist Sir Chandrasekhara Venkata Raman was awarded the Nobel prize for the discovery of inelastic light scattering of photons by matter.[89] Photons impinging on molecules can (de)excite vibrational and rotational modes when being scattered. The scattered photons therefore have higher energy than the incident photons in the case of a

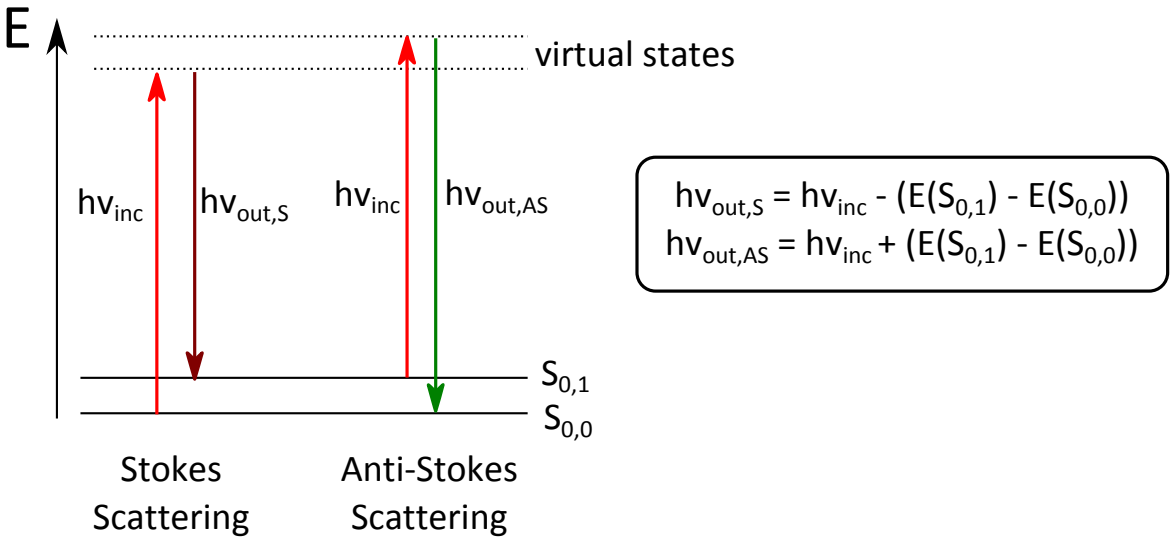

Figure 2.3 Scheme showing the energy levels involved in the Raman process. Generally the frequency of the incoming light ν_{inc} is fixed. The scattered light is detected and the difference between the energy of the incident photons and the detected photons with frequency ν_S or ν_{AS} gives the energetic information about the vibrationally excited state $S_{0,1}$.

molecular deexcitation (Anti-Stokes scattering) or lower energy, when vibrational/rotational[1] modes in the molecule are being excited (Stokes scattering).[90,91] This inelastic scattering process is in contrast to the elastic (Rayleigh) scattering, where the scattered photons have the same energy as the incident photons. Independent of the energy of the incoming photons the energy difference ΔE between incident and scattered light is characteristic to the scattering molecule since it solely depends on the energy difference between the vibrational states of the molecule.

Raman scattering can be visualized using the energy scheme shown in Figure 2.3. As inelastic scattering is an instantaneous process (as opposed to absorption-emission in fluorescence), the intermediate, excited energy state can be a virtual state. Since the transition probability into the virtual state is very low, the inelastic scattering cross sections are small (integrated Raman cross sections: 10^{-29} to 10^{-31} cm^2,[92] compared to i.e. $\approx 10^{-16}$ cm^2 for absorption or fluorescence[93]). Strong light sources (Lasers) are therefore used for Raman spectroscopy and the Rayleigh scattered light has to be filtered from the detected signal.

[1] For ease of reading, we will only mention vibrational modes from here on. This conceptually also includes rotational excitations

A molecule or chemical species that provides an electronic state in resonance with the incoming light, however, presents an actual existing electronic state for the Raman process. The presence of this state can significantly increase the cross section for inelastic scattering as now the transition probability into the excited state is much higher compared to the non-resonant case.[94]

Raman spectra are commonly reported as the intensity of the inelastically scattered light versus the Raman shift in reciprocal centimeters. The Raman shift is defined as $\Delta\omega = \left(\frac{1}{\lambda_0} - \frac{1}{\lambda_1}\right)$ with λ_0 the wavelength of the incident laser radiation and λ_1 the wavelength of the detected scattered light.[94] The Raman shift is directly proportional to the difference in energy ΔE between the two vibrational/rotational states in the chemical species being probed and Raman spectra measured with different excitation wavelengths can be directly compared with respect to their band positions.

The position of Raman bands depend on the molecular vibrations that are being excited. The frequency of these vibrations is correlated with the mass of the atoms involved in the vibration and the strength of the bond between them. Atoms with low atomic weight as well as strong bonds show high Raman shifts.[95] Raman spectroscopy can be used to monitor changes in the environment of molecules. When a molecule binds to another chemical species, electronic density inside the molecule will be redistributed and the strength of the bonds close to the binding site will change. This change in bond strength will manifest in a shift of the Raman bands associated with the bonds.

Raman intensities depend on the amount of scatterers that are being probed and the vibration's cross-section for the Raman process. The cross-section is proportional to the square of the change in the molecule's polarizability during the vibration.[94] Therefore, vibrations that do not change the molecule's polarizability are not Raman active. As mentioned before, Raman cross-sections are low, especially when compared to other optically triggered processes. We therefore often have to rely on measuring bulk samples (i.e. pure substances) as otherwise the Raman signal disappears in the electronic noise of the measuring system. This is an issue, especially when single layers of molecules on surfaces are to be investigated. For some substrates, we can use a method known as Surface-Enhanced Raman Spectroscopy which we will briefly discuss below.

Surface-Enhanced Raman Spectroscopy

About 40 years ago it was discovered that single layers of non-resonant molecules adsorbed to coinage metal surfaces (such as silver, gold or copper) can be studied using Raman spectroscopy without facing issues from too low signals.[96–98] This seems to contradict the general observation of low Raman cross-sections. The basis for the high signals observed in these cases lies in an excitation of localized surface plasmons in rough metal surfaces to enhance local electromagnetic fields near the metal surface. Plasmons are quasi-particles that describe the collective oscillations of the free electron gas in a metal. The resonant frequency of these oscillations lies in the range of visible light for coinage metals. Incoming light with the right energy can, under the right circumstances as described later, excite plasmons at the metal surface. These induced electron oscillations can effectively enhance the local electromagnetic field by up to two orders of magnitude, leading to enhanced Raman scattering from molecules close to the surface. The method utilizing these plasmonic effects is called Surface-Enhanced Raman spectroscopy (SERS).

A perfectly flat metal surface cannot act as a Raman enhancer. Since the dispersion curves of the surface plasmons in the metal and the dispersion curve of light traveling through free-space do not intersect, momentum and energy conservation cannot be fulfilled at once and the plasmon cannot radiate.[99,100] Surface corrugations can act as a grating and localize the surface plasmons. This adds an additional term to the momentum vector of the surface plasmon which enables momentum conservation; the plasmon can radiate and the Raman signal is enhanced.[94]

On a rough metal surface this matching of surface corrugations to enable momentum conservation is a purely statistical probability; some combinations of corrugations on the surface will per chance provide the necessary momentum vector and as such make an efficient coupling of the surface plasmon to the far-field locally possible. This leads to the occurrence of SER hot spots where the Raman scattering is locally enhanced.[101] Only few locations on a metal surface within a roughly 2 μm^2 laser focus spot will fit the requirements to provide the necessary momentum and lead to an enhancement of the Raman scattering. Fang et al. have reported a density as low as 63 sites out of 1 million possible sites.[102] The enhancement effect is confined to only a few nanometers ($\approx$ 10 nm[94]) around the hotspot itself. As such

SERS is inherently a surface sensitive technique and lends itself well to study metal-adsorbate interactions.

The surface plasmon of copper has its resonance wavelength at 573 nm with still a significant contribution at 633 nm, a commonly used Raman excitation wavelength.[103] While a lot of effort has been put forward to engineer improved substrates for SERS,[104–106] even a naturally occuring, rough copper surface can already lead to significant Raman enhancement.[107,108] We can therefore use an illumination wavelength of 633 nm to measure SER data on the commercially available copper foils that we use as a substrate for our CuBTC synthesis as shown in chapter 4.

Electrochemical Surface-Enhanced Raman Spectroscopy

The use of a metal surface as a substrate for Raman spectroscopy opens up even more possibilities than just using the surface plasmons to enhance the signal. By immersing the metal surface into an electrolyte and connecting it to a potentiostat in a three-electrode configuration, we can actively trigger electrochemical processes, such as redox processes or molecular ad-/desorption, at the metal surface by setting a desired potential between the electrodes.

Combining SERS with electrochemical techniques (EC-SERS),[109,110] we can monitor the electrochemical processes as a function of the applied potential. We can learn about i.e. changes in the adsorption density of a molecule on the metal through changes in the intensities. Changes in molecular orientation and strength of the bond between metal and adsorbate can be observed through band position shifts. We combine the surface-enhancement effect for 633 nm illumination on copper with electrochemical techniques to directly monitor the interaction between BTC and copper in chapter 4.

Instrumentation

The Raman spectra presented in this work were measured on two Raman systems. All measurements with 633 nm excitation wavelength were done on a home-built setup with a 35 mW 633 nm Helium-Neon continuous wave-laser. Signal collection was done in back-

scattering by a long working distance (WD) air objective (Olympus LMPlan FL N, 50x, numerical aperture 0.5, WD=11.6 mm) at a 55° angle from the sample normal. The laser power on the sample could be tuned between 150 µW and 25 mW through the use of a set of neutral density filters. The laser power at the sample was set to 2 mW unless stated otherwise. The light scattered from the sample (elastically and inelastically) is passed through a notch filter with a cut-off at ≈ 150 cm^{-1} in our Raman scale to filter out the elastically scattered light. The signal was collected using a nitrogen-cooled camera (Horiba Symphony II). The spectrograph was a Horiba iHR550. Using the coarsest grating available (400 grooves / mm) the camera can only collect a spectral range of roughly 1600 cm^{-1} around a chosen central position. For acquisition of spectra with larger Raman shift ranges, multiple spectra had to be taken with the central grating position changed. I.e. a spectrum spanning 3000 cm^{-1} is stitched together from two to three, depending on the desired overlap, separate spectra that are taken consecutively.

Raman spectra with 488 nm excitation were taken on a commercial Bruker Senterra Raman microscope. Raman excitation and detection are done through the same objective parallel to the sample normal. The laser power on the sample was set to 2 mW unless stated otherwise. The microscope was used for Raman mapping. The Raman maps can be directly correlated to a white-light image, as done in chapter 3.

Raman spectra had cosmic spikes removed by hand. If background correction was needed for band integration, it was performed using an asymmetric least squares algorithm.[111] All data evaluation was done using custom-built Python or Matlab code.

2.3 Imaging techniques

Since CuBTC generally grows into easily recognizable octahedral crystals in the size range of a hundred nanometers up to tens of micrometers, imaging techniques can provide valuable information about the morphology of a CuBTC sample. While the larger crystals (> 1 µm) can even be observed using light microscopy, the most commonly used imaging technique for MOFs of any kind is scanning electron microscopy (SEM). If more information about the actual surface morphology of the crystals is desired, atomic force microscopy (AFM) can be

used. Especially MOF crystals that are oriented parallel to the scanning plane of the AFM are prime candidates for investigation of the topography of single MOF crystal facets as we do in Appendix A.

2.3.1 Scanning Electron Microscopy

An SEM produces images by scanning a sample with a focused electron beam. Electrons impinging on a sample lead to a variety of physical processes that are the basis for different kinds of detectors in the SEM. The signal measured with a chosen detector is then correlated to the position the beam was in at that moment in time and the information is reconstructed into an image of the surface.[112]

SEM images give a close to three-dimensional representation of the sample surface. The very narrowly focused electron beam leads to a large depth of focus (depth in the sample that is in focus at the same time), which allows imaging of even rough samples in single images without the need for z-scanning. Through the detector choice the contrast in the image can be altered to emphasize different materials or differences in topological height of the sample. Secondary electrons for example are emitted due to inelastic scattering of the impinging electrons. The high energy electrons (0.6-20 keV) of the beam eject secondary electrons from the inner shells of the atoms in the sample that have a much lower kinetic energy ($\approx$ 50 eV). Due to the low energy of the ejected electrons they generally originate from within the first few nanometers of the sample. Detection of these electrons gives rise to a strong topographical contrast.

The resolution of SEM far surpasses the diffraction limited resolution of light microscopy of $\approx$ 400 nm due to the low de Broglie wavelength of the accelerated electrons in the range of tens of picometers. As such SEM can routinely resolve features down to 1 nm in size.

All SEM images in this work have been measured on a Zeiss 1530 Gemini Leo at varying acceleration voltages (between 0.7 and 1 keV). For electrochemically produced samples the copper electrodes themselves were investigated as received from the synthesis. Powder samples were isolated by centrifugation and spread on carbon tape for investigation in the

SEM. All images were taken by Gunnar Glasser at the Max-Planck Institute for Polymer Research.

2.3.2 Atomic Force Microscopy

AFM is a type of scanning probe microscopy that uses the detection of short-range ($\approx$ 0.1-10 nm) forces between an ideally atomically sharp tip (commonly made from SiN_3) and a sample surface to construct topographic images of the sample surface. When the AFM tip approaches a sample surface the tip experiences a variety of different possible forces from the sample (and vice versa). At longer ranges (> 1 nm) attractive forces due to e.g. van der Waals interactions dominate. When the tip gets closer ($\approx$ 0.1 nm) Pauli repulsion due to overlapping electron orbitals of tip and sample starts to dominate the interaction leading to a net repulsion of the tip.[113]

The AFM tip is fixed to a cantilever, a flexible lever-like bar. In our measurements we use the constant amplitude measuring mode in which the AFM cantilever is excited to vibrate at its resonance frequency. The amplitude of the vibration is monitored as the cantilever scans over the surface. The amplitude of the vibration changes from changing forces acting on the tip due to surface corrugations or differences in the stiffness of the sample. Feedback electronics adjust the height of the tip to recover a setpoint amplitude and the changes in height allow reconstruction of a topographical image of the surface. This measuring mode is generally favorable to use for soft samples or samples with large height corrugations (such as MOF surface coatings). The short range of the forces between tip and sample as well as the advances in the manufacturing of AFM probes has lead to routine AFM measurements with spatial resolutions below one nanometer, both laterally as well as in height.

In Appendix A we use AFM to investigate the surface of electrochemically and oxidatively grown CuBTC crystals. The AFM measurements were done on a JPK Nanowizard III, using cantilevers with 300 kHz resonance frequency in constant-amplitude mode. All image evaluation was done in Gwyddion.

2.4 Characterization of electrochemically synthesized CuBTC

Here, we want to briefly show the procedure of a close-to-literature electrochemical synthesis of CuBTC and characterize the obtained sample with the methods introduced earlier. This section will serve as a knowledge basis for the discussion in the remaining chapters.

2.4.1 Electrochemical synthesis of CuBTC

For electrochemical synthesis of CuBTC the sacrificial anode (WE) that is oxidized to provide the necessary Cu^{2+} ions is a piece of copper foil (0.5 mm thick, 1x1 cm^2, purity 99.99+%, Mateck). A hole in one of the corners of the square anode is used to connect the anode to a 0.25 mm diameter copper wire which is in turn connected to a potentiostat (Solartron SI 1286). A platinum wire (d=0.25 mm) that has been briefly cleaned with MilliQ water (18.2 MΩ) and then flame-annealed for 15 seconds is wound into a coil and suspended into the solution. The platinum wire is connected to the potentiostat as the CE. As a RE a piece of copper wire (d= 0.25 mm) is connected to the potentiostat and suspended into the solution close (2-5 mm) to the working electrode.

The synthesis solution consists of 0.15 M trimesic acid (BTC, Santa Cruz Biotechnology, > 98%) and 0.032 M of tributylmethylammonium methyl sulfate (MTBS, Sigma Aldrich ≥ 95%) in 96% ethanol (Sigma Aldrich, 99.9 %) with 4% of MilliQ added (by volume). While BTC is the necessary linker for the synthesis of CuBTC, MTBS is added as a supporting electrolyte to ensure the conductivity of the solution. BTC and MTBS, both solid substances, are weighed in and added to a measuring flask that is then filled with the ethanol/MilliQ mixture. The solids are dissolved using ultrasonication for 15 minutes. A typical solution volume is 50 mL.

The home-built electrochemical cell is cleaned in a 5:1 mixture of sulfuric acid (H_2SO_4) and hydrogen peroxide (H_2O_2) over night prior to an experiment. After removal of the mixture the cell is boiled three times in fresh MilliQ water.

Typically a potential between 0.2 and 2 V is applied between the RE and the WE for times ranging between 2 and 20 minutes. In literature the potentials used for maximum synthesis

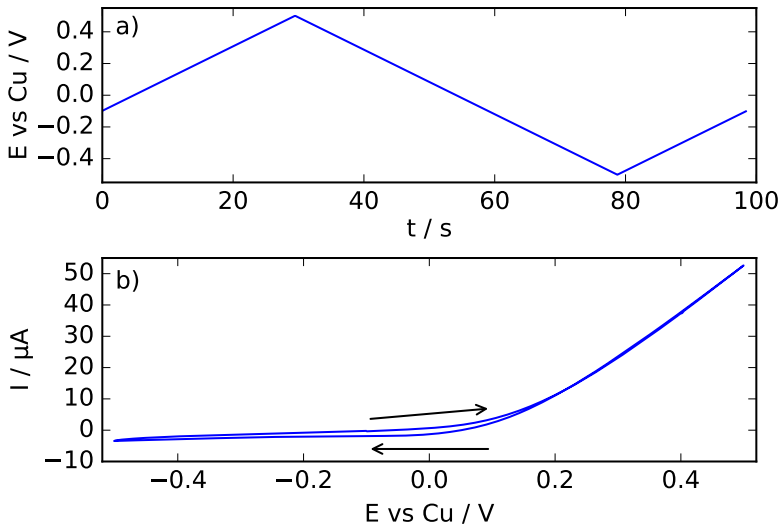

Figure 2.4 An example cyclic voltammetry experiment under conditions commonly used for electrochemical CuBTC synthesis. The electrolyte was 0.15 M BTC and 0.032 M MTBS in 96% ethanol with 4% water. a) shows the potential ramp applied to the working electrode over time. b) shows the current response versus the applied potential. The arrows indicate the scanning direction in the respective half-cycles. $v = 20\,\mathrm{mV\,s^{-1}}$

throughput are up to 30 V.[51] As we are interested in the molecular processes at the WE and not in high throughput, we choose lower synthesis potentials as this will lead to lower current densities, thus lower amounts of copper released from the electrode and slow down the synthesis. After the synthesis the copper anode is rinsed with ethanol and can be investigated using Raman spectroscopy and scanning electron microscopy.

2.4.2 Electrochemical characterization of copper in BTC containing electrolyte

We first want to electrochemically characterize the copper electrode in the synthesis solution using cyclic voltammetry. Afterward we will look at the evolution of the current during the synthesis of CuBTC.

Figure 2.4 shows a cyclic voltammetry experiment of the Cu electrode in the synthesis electrolyte described above (0.15 M BTC, 0.032 M MTBS in 96% ethanol). The RE was a copper wire, the CE a platinum coil. Figure 2.4 a) shows the potential ramp applied versus

time. At the start, the potential was set to -0.1 V and then ramped at 20 mV/s until an upper vertex potential of 0.5 V. The scan direction is reversed and the potential sweeped with the same velocity until a potential of -0.5 V, where the sweep is reversed again until the starting potential of -0.1 V is reached.

Figure 2.4 b) shows the current density I versus the applied potential E. The arrows indicate the potential sweep directions for the two half-cycles. Starting from a potential of -0.1 V vs Cu in positive sweep direction, the current trace starts slightly above 0 µA and stays flat at first. After crossing 0 V vs Cu the current starts increasing considerably. The slope increases until around 0.2 V from where on it stays constant and the current increases linearly with the applied potential. After crossing the upper vertex potential at 0.5 V and reversing the potential sweep, the current decreases linearly with the potential. Below 0.1 V the current starts leveling off, and stays almost constant, slightly negative, from 0 V on. After reaching the lower vertex potential of -0.5 V and reversing the sweep again, the current stays almost constant until the scan is stopped at 0 V.

No peaks form in the current trace. Above 0 V an oxidation process takes place that is neither limited by diffusion of a reactant to the electrode nor by a fast passivation of the electrode surface as indicated by the lack of peak formation. Even increasing the upper vertex potential does not change the voltammogram qualitatively, we still observe a linear relationship between current and applied potential at potentials higher than 0.2 V (not shown). We assume that the current is limited by the low conductivity of the ethanolic electrolyte,[51] meaning that as the current increases the increasing potential is used to overcome the solution resistance R according to $R = \frac{E}{I}$. However, even increasing the solution conductivity has shown to not change the qualitative results of the cyclic voltammetry experiments which shows that the electrochemical process we observe generally does not seem to be limited by either diffusion or surface passivation.

Figure 2.5 shows the current density passing through the copper anode during the course of 20 minutes at an applied potential of 0.5 V vs Cu in the CuBTC synthesis solution detailed above. At the beginning of the trace, a current density of 44 $\mu A\,cm^{-2}$ passes through the electrode. The current density drops slightly over the course of roughly 200 seconds to 41 $\mu A\,cm^{-2}$ after which it stays constant within a range of $\pm$ 0.2 $\mu A\,cm^{-2}$.

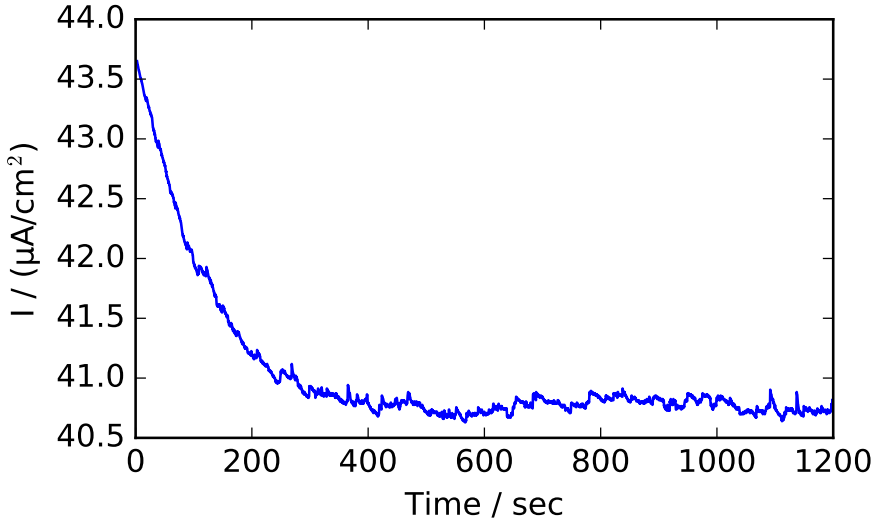

Figure 2.5 Current density over time for a copper anode in 0.15 M BTC and 0.032 M MTBS in 96% ethanol/4% water at 0.5 V vs Cu.

The current trace confirms that the electrode process is not diffusion limited at long time scales. A diffusion limited oxidation process would, according to the Cottrell equation,[81] manifest itself in a constant drop of the current density that is proportional to the square-root of the time. The trace only shows a slight drop in the beginning (which also does not follow a square-root dependence) after which the current stays constant. We attribute the drop in the beginning to a partial passivation of the electrode. We know from literature[51] and the Raman spectra taken after the synthesis (see Figure 2.6) that the oxidation process we observe in our experiment is the synthesis of CuBTC. The copper anode is oxidized to Cu^{2+} and CuBTC forms with the BTC molecules from the solution. CuBTC is an electrical insulator.[79] The fact that we do not see an increasing passivation effect over time could mean that after a while ($\approx$ 200 seconds in our experiment) a close-to-equilibrium situation forms in which the amount of CuBTC that is freshly produced - which passivates the surface - is balanced by continuous detachment of fully grown crystals as already discussed earlier in our literature review.[79] As the crystals detach, new surface area on the electrode is exposed to the electrolyte and can be active in the process again. This growth-detachment equilibrium could also explain the slight current oscillations and jumps that we see in the trace during the current plateau after 200 seconds.

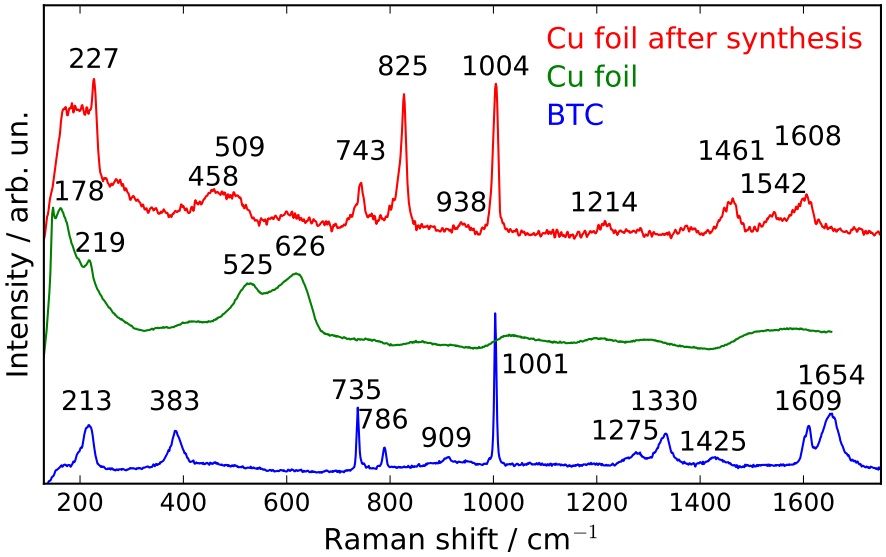

Figure 2.6 Raman spectra of the linker BTC (blue), a copper foil surface (green) and the surface of a copper anode after electrochemical CuBTC synthesis (red). All spectra were measured with 633 nm excitation.

2.4.3 Characterisation of the anode after electrochemical CuBTC synthesis

Figure 2.6 shows typical Raman spectra taken on the surface of a copper electrode before the electrochemical synthesis of CuBTC and the copper electrode after the electrochemical synthesis. We added the Raman spectrum of the bulk BTC powder for comparison.

The spectrum of the copper foil before the synthesis (Figure 2.6 green) shows two broad bands at 525 cm^{-1} and 626 cm^{-1} as well as two sharp bands at 219 cm^{-1} and 178 cm^{-1}. The spectrum matches literature spectra of surface oxides on copper, that are primarily governed by surface-Cu_2O.[117,118] The surface of copper in ambient conditions at room temperature is oxidized by oxygen and humidity to a mixture of Cu_2O, CuO and $Cu(OH)_2$.[119] Cu_2O, cuprite, is the primary product of ambient oxidation of copper, CuO and $Cu(OH)_2$ are present at such a low concentrations that we cannot detect them in our Raman spectra.

On the surface of the copper electrode after the electrochemical synthesis (Figure 2.6 red) we find a Raman spectrum that closely matches the spectra reported for CuBTC in literature.[87] We observe similar spectra for CuBTC and BTC (Figure 2.6 blue) with respect to the rough

Table 2.1 Band assignment for the Raman spectra of BTC, an oxidized copper surface and CuBTC. Numbers are in cm^{-1}. v: stretching, δ: in-plane bending, γ:out-of-plane bending

BTC	Oxidized Copper	CuBTC	Assignment
213			-
	178		-
	219		Cu_2O ($2\,\Gamma_{12}$)[114]
		227	vCuCu[87]
383			-
		458	vCu-O, $vCu_2(\mu-O)_2$[87]
		509	vCu-O, $vCu_2(\mu-O)_2$[87]
	525		Cu_2O ($\Gamma_{25}+$)[114]
	626		Cu_2O ($\Gamma_{15}^{(2)}$)[114]
735			δCO, δCC[115]
		743	γCH_{ring}[87]
786			δCO, δCC[115]
		825	γCH_{ring}[87]
909			-
		938	-
1001		1004	vCC_{ring}[115]
		1214	-
1275			δCH,vCC,δOH[115]
1330			vCO, vCC[115]
1425			vCC, δCH[115]
		1461	$v_{asym}C-O_2$[87]
		1542	$v_{sym}C-O_2$[87]
1609		1608	vCC_{ring}[87]
1654			vC=O[116]

position of the peaks, especially in the higher wavenumber region (above 700 cm^{-1}) which shows that the Raman spectrum of CuBTC is primarily governed by the organic moieties of the BTC. However, in the region between 700 and 850 cm^{-1} the spectral differences between CuBTC and BTC are large enough so that we can use the Raman spectra to unambiguously differentiate between the two chemical species. While we see two peaks in this area both for BTC (at 735 and 786 cm^{-1}) and CuBTC (at 743 and 825 cm^{-1}) they are not only shifted with respect to each other but also show different relative intensities. For both species they are the most pronounced, unique bands. The only band that shows a higher absolute intensity

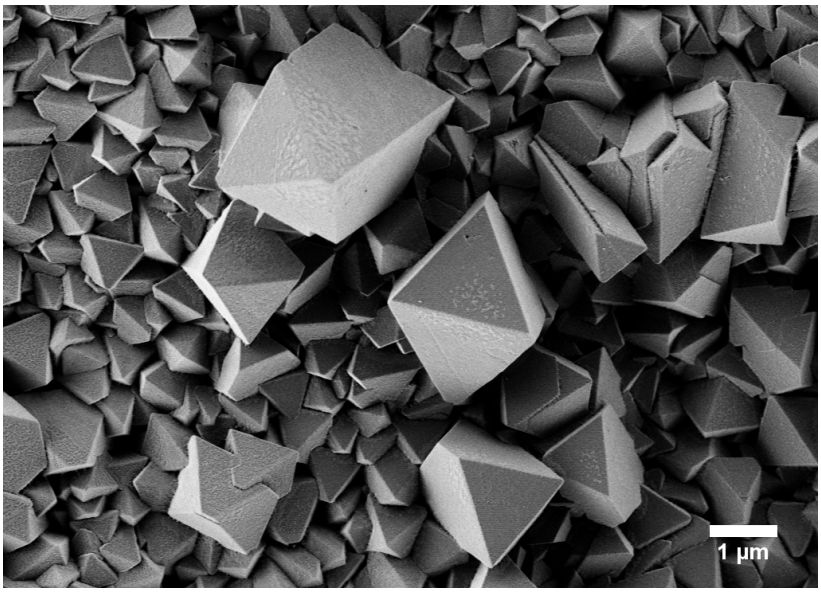

Figure 2.7 Scanning electron micrograph of a CuBTC coating on a copper substrate. Scale bar: 1 µm.

is the ring-breathing mode of the BTC molecule just above 1000 cm^{-1}. This band does not show a strong enough shift between CuBTC (1004 cm^{-1}) and pure BTC (1001 cm^{-1}) to use as clear indication for either substance.

A detailed Raman band assignment based on literature is shown in Table 2.1. We will use the Raman spectra of CuBTC and the copper surface for our discussion in chapter 3. Chapter 4 will give detailed insight into the interaction between copper and BTC under electrochemical conditions based on the Raman spectra of BTC.

The presence of CuBTC on the surface of the electrode is spectroscopically confirmed. We investigate the morphology of the sample using SEM. Figure 2.7 shows a scanning electron micrograph of the surface of the copper anode after the electrochemical synthesis. The image shows a densely packed layer of crystalline particles in the size range of 0.5 - 5 µm. Some of the crystals seem to be intergrown with each other. The primary shape of the exposed crystal facets is a triangular shape. The crystals are randomly oriented. While we do not have a full 3D view of a crystal, the prevailing crystal shape seems octahedral or at least approaching an octahedron. Only a few crystals (mainly the ones that stick further out from the surface) tend to be elongated in one crystal axis direction. As our Raman spectra show, the surface is covered with CuBTC and the particles we observe here are MOF crystals.

CuBTC forms octahedral or close to octahedral crystals with the (111) facets of the crystal structure primarily facing outward.[120] This can be rationalized by the fact that the (111) facet grows faster than e.g. the (100) facet as we have discussed earlier.[77,78]

The provided Raman spectra as well as the SEM image shown will serve as a reference for the discussion of the results in chapters 3 and 4. First, in chapter 3 we want to explore the exact redox-mechanism of the oxidation process we observe above 0 V vs Cu.

Chapter 3

The oxidation mechanism of electrochemical CuBTC synthesis

In this chapter, we unravel the oxidation-reaction mechanism of the electrochemical formation of CuBTC. Despite CuBTC being one of the most extensively studied MOFs,[51,121] its electrochemical formation mechanism has not yet been unraveled. It has been postulated that Cu is anodically oxidized in one step to Cu^{2+} followed by linker coordination in solution.[52] True single-step two-electron transfers are rare[122] and generally two-electron oxidations are comprised of two separate one-electron oxidation steps.[123]

We find that the formation of Cu^{2+} needs an intermediate Cu^{I} oxidation state. Through systematic variation of the experimental parameters we find that the necessary Cu^{I}-species is cuprite, Cu_2O. If the synthesis solution contains no accessible reagents for cuprite formation, such as water or oxygen, the synthesis fails to produce CuBTC. It is possible to enable the formation of CuBTC in solutions without oxide-forming reagents by providing the cuprite in the form of a film on the copper electrode surface. Cuprite itself, in the form of pure cuprite powder, turns out to be an equally good starting material for CuBTC formation. To synthesize CuBTC from cuprite ambient oxygen can be used as an oxidizing agent.

We apply the knowledge about the necessary reaction intermediate state by developing a new method for the fabrication of patterned CuBTC chips. Utilizing the possibility to distinguish between cuprite-covered and cuprite-free surfaces, a piece of copper foil can be patterned

with cuprite prior to the synthesis. The patterning is as easy as placing a droplet of acid on an oxidized copper surface. After removal of the droplet the synthesis is performed using a solution without oxide-forming reagents. CuBTC is selectively synthesized on parts of the sample that were previously not treated with acid.

The following results have been published in *Chemical Communications*, 2016, **52**, 4722-4725.

3.1 Experimental part

The electrochemical syntheses in this chapter have been performed according to the previously discussed protocol (section 2.4.1) with slight changes to the protocol as follows. An Ag/3M KCl/AgCl electrode was used as a reference. The potential of the silver reference is roughly 0.02 V vs a Cu reference. The synthesis time for electrochemical synthesis was generally 20 minutes and the synthesis potential was 1 V vs Ag/AgCl.

If necessary for the experiment, we removed surface oxides from the copper anode (size 1x1 cm^2). Prior to the synthesis, the copper foil was immersed into 20 mL of 25% nitric acid for 3 minutes, rinsed with MilliQ, immersed into 20 mL of 25% hydrochloric acid for 3 minutes, rinsed with MilliQ, rinsed with ethanol and immediately inserted into the electrochemical cell, following a procedure by Hall et al.[124]

Solutions were degassed by bubbling with Argon (99.9999%, Westfalen AG, Münster) for 20 minutes when necessary. The experimental setup was kept in an Argon atmosphere afterward.

The surface of the copper foils used for samples of type C was oxidized prior to the synthesis by applying a potential of 1 V vs Ag/AgCl for 25 minutes in 10 g/L MTBS in 4% H_2O/96% ethanol - the CuBTC synthesis electrolyte without BTC.

To synthesize CuBTC from copper oxide powders 200 mg of Cu_2O or CuO were dispersed in 7 mL of a solution of 0.15 M BTC in ethanol. After 16 hours at room-temperature the dispersion was centrifuged at 6000 rpm for 10 minutes. After removal of the supernatant the residue was re-suspended in ethanol and centrifuged at 6000 rpm for 10 minutes. The supernatant was discarded and the resuspension/centrifugation procedure repeated. After

drying in nitrogen stream the powder product was dispersed on carbon tape for investigation with SEM and was spread on a glass slide for Raman measurements.

For the fabrication of patterned MOF devices, the surface of a piece of copper foil was oxidized in 0.1 M NaOH solution in water. A potential of -0.1 V was applied for 10 minutes. The produced cuprite was selectively removed from the center of the copper foil with a drop of 10% HCl. The drop was carefully removed with a pipette and the foil rinsed with MilliQ water. After drying in a nitrogen stream the foil was used in an oxygen- and water-free CuBTC synthesis.

3.2 Cuprite as a necessary reaction intermediate

By systematically varying the synthesis conditions such as the Cu source and the presence of O_2 we investigate the role that the different components of the synthesis mixture play in electrochemical CuBTC synthesis. The synthesis conditions used are summarized in Table 3.1.

Sample A represents synthesis conditions close to what has been reported in literature.[51] As we are not interested in a high synthesis throughput and want to keep possible electrochemical side reactions (such as solvent oxidation) to a minimum, the synthesis potential is kept low at 1 V. In the synthesis for samples B we eliminated all components of the synthesis mixture that according to the dissolution-coordination mechanism discussed in literature[51,52] should be unnecessary for the successful synthesis of CuBTC. The copper surface is freed of naturally occuring oxides, the solution is degassed to remove dissolved oxygen and absolute ethanol is used, thus no water is present during the synthesis. Sample C is synthesized in similar conditions as example B with the exception that the copper plate is electrochemically oxidized (to cuprite[125]) prior to electrochemical synthesis of CuBTC. Sample D is not produced electrochemically, since the Cu_2O powder cannot easily be incorporated into an electrode. Instead we use a synthesis solution of 0.15 M BTC in ethanol and let the mixture incubate under atmospheric conditions for 16 hours. Sample E is synthesized like sample D, but using $Cu^{II}O$ as a starting material instead of $Cu^{I}{}_2O$. Sample F is produced like Sample D with the

only exception being that the solution was partially degassed, significantly decreasing the amount of oxygen that is dissolved in the solution.

Table 3.1 Overview of the synthesis conditions for samples A-F

Sample type	Cu source	O_2 presence	E / reaction time	successful CuBTC synthesis
A	Cu with natural oxide layer	Yes	1 V / 20 min	Yes
B	Cu, oxide free	No	1 V / 20 min	No
C	Cu with artificial oxide layer	No	1 V / 20 min	Yes
D	Cu_2O	Yes	No / 16 hours	Yes
E	CuO	Yes	No / 16 hours	No
F	Cu_2O	low amount	No / 16 hours	Yes (low amount)

All samples were investigated with SEM and Raman as to their topography and chemical composition. As discussed previously in chapter 2, CuBTC can be identified against other possible parts of the reaction medium by the Raman in-plane ring bending vibrations of the BTC moiety at 743 cm^{-1} and 825 cm^{-1}. In addition CuBTC forms octahedral crystals that are easily recognizable in the SEM micrographs.

Fig. 3.1 shows the SEM micrographs and 3.2 the Raman results for sample types A-D. The results for samples E and F are shown in Figure 3.3 and 3.4 respectively.

Samples A were fabricated under synthesis conditions similar to the synthesis protocols found in literature,[51,126] i.e. starting from a Cu-electrode with a natural oxide layer, ethanol with 4% water content and taking no precautions to avoid the presence of O_2 in the solution. Octahedral crystals of CuBTC of <1 µm to 5 µm in diameter are found in the SEM images (Fig. 3.1A). Electrode coverage is incomplete at 20 particles/100 μm^2, likely due to the low synthesis potential of 1 V. An increased synthesis time could improve surface coverage. The corresponding Raman spectrum in Fig. 3.2A displays the characteristic bending vibrations of CuBTC at 743 and 825 cm^{-1}. The Raman spectrum also shows a significant contribution of Cu_2O with two broad peaks at 525 and 626 cm^{-1}. The SEM image together with the Raman spectra prove that CuBTC was synthesized successfully in samples A.

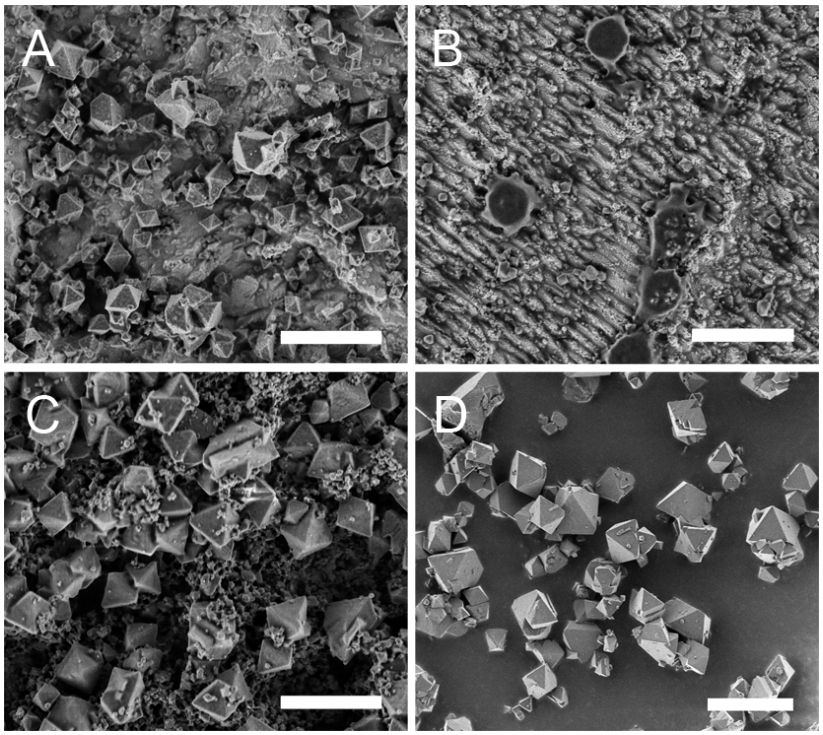

Figure 3.1 Example SEM images of samples A-D. Scalebars are 10 µm

Samples B were produced under oxide-, water- and O_2-free conditions, thus void of all components unnecessary for the simple Cu^{2+} dissolution-coordination mechanism proposed in literature. The SEM image (Fig. 3.1B) shows parallel 'tracks' on the surface of the copper anode due to the acidic etching of the surface prior to the experiment. With exception of only about 1 octahedral particle/100 μm^2 of ca. 0.5 to 1 µm diameter, no octahedral crystals are visible. The CuBTC response in the Raman spectra can hardly be distinguished from the noise (Fig. 3.2B). In addition only a comparatively small contribution of surface-Cu_2O can be seen in the Raman response as evident through the low signal to noise of the cuprite bands at 525 and 626 cm^{-1}. The observations show that CuBTC does not grow under oxygen- and oxide-free conditions. The small amount of particles that are found on the surface can be attributed to residual oxygen contamination in the solution or to partial reoxidation of the copper surface during transport to the electrochemical cell. The oxide response we find in the Raman spectra are most likely due to reoxidation of the surface after the synthesis or during the Raman measurement. Since copper readily oxidizes in ambient conditions and the samples could not immediately be protected against ambient air, some oxide formation could not be excluded.

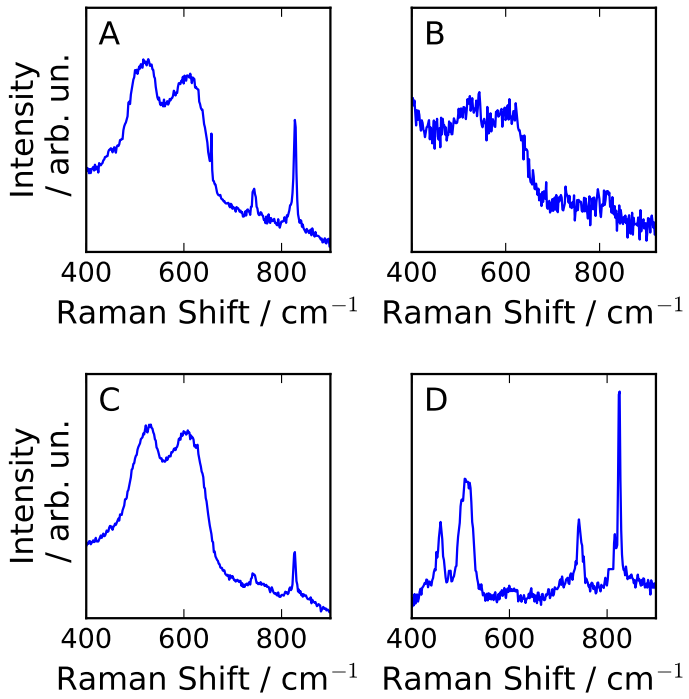

Figure 3.2 Raman spectra of samples A-D. Samples A-C were measured directly on the copper plates used for the synthesis. Sample D was measured as an isolated powder. The spectra have not been corrected.

Since oxygen- and oxide-free conditions failed to produce CuBTC, we now try to find the smallest set of components required to enable CuBTC synthesis. We electrochemically oxidized the surface of the Cu plate on purpose by immersing it in an electrolyte containing only MTBS and dissolved oxygen in 96% Ethanol/4% water. A potential of 1 V vs Ag/AgCl was applied for 25 min to oxidize the surface of the copper anode. Afterwards we performed an O_2-free MOF synthesis (Samples C). Raman spectroscopy confirms the successful synthesis of CuBTC (Fig 3.2C) as the signals at 743 and 825 cm^{-1} can be found. The spectrum additionally shows a significant Cu_2O contribution between 400 and 600 cm^{-1}. The SEM images of samples C show that the copper anode is covered with a mixture of about 5 octahedral crystals of 3 to 5 µm diameter per 100 µm^2 and ca. 50 particles/100 µm^2 in the sub-µm diameter range. At some spots, the smaller crystals cover the larger particles.

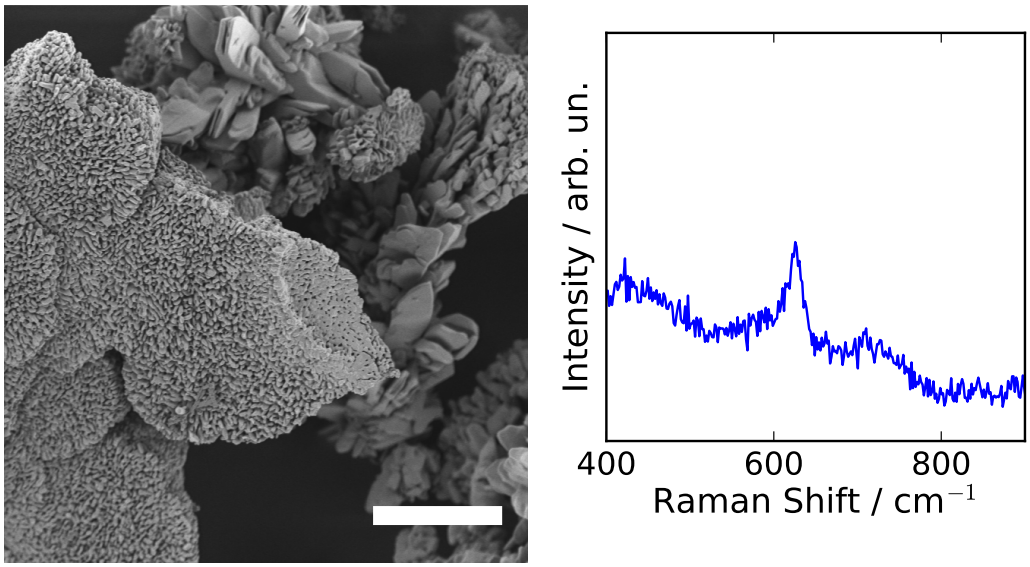

Figure 3.3 Results for a synthesis starting from CuO (Samples E). left: SEM micrograph showing no CuBTC octahedra (scale bar: 5 µm). right: Raman response of the isolated powder

From experiments A to C, we learn that oxygen plays an important role in ec CuBTC synthesis as CuBTC crystals do not grow under oxygen-free conditions (samples B) and Cu_2O is always present on the electrodes in successful CuBTC syntheses, as evident from the Raman spectra. To further investigate the role of oxygen, we used pure oxides as precursors for CuBTC growth. For Samples D, we immersed Cu_2O powder in an ethanolic solution of 0.15 M BTC without any other additions for 16 hrs under ambient conditions. No potential was applied. A blue powder was isolated by centrifugation and characterized. The SEM micrograph in Fig. 3.1D shows octahedral crystals of 1 to 5 µm diameter that are intergrown into larger agglomerates of 10 to 15 µm diameter. Raman spectra (Fig. 3.2D) confirm successful CuBTC synthesis through the presence of the two characteristic CuBTC bands at 825 and 743 cm^{-1}. The other bands visible in spectrum D at 460 and 508 cm^{-1} also belong to CuBTC. They are invisible in the spectra measured for Samples A and B, as the copper oxide signal lies on top of those two bands. As we do not see any residual Cu_2O bands at 525 and 625 cm^{-1} and the SEM images show only octahedral crystals of CuBTC, we can conclude that all cuprite was consumed to produce CuBTC. Interestingly, an analogous experiment with CuO powder as starting material did not produce any CuBTC (Samples E, Fig. 3.3). For Samples E the SEM images (Fig. 3.3, left) show only pristine CuO in the form

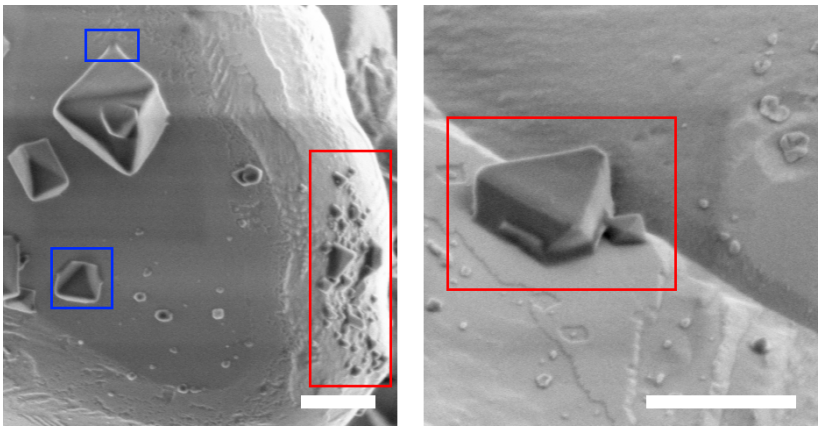

Figure 3.4 SEM micrographs of Samples F. Red: truncated crystals; blue: intergrowth with surface. scale bars: 500 nm.

of scale- and sometimes sponge-like crystals. The Raman spectra (Fig. 3.3, right) show only the spectroscopic response of CuO with a low-intensity peak at 628 cm^{-1}.[117,127]

As the transformation of Cu_2O to CuBTC in sample D occurred without the application of an electrochemical potential, a different oxidation agent needs to be responsible for the oxidation of Cu^I to Cu^{II}. To identify this oxidation agent, Samples F were synthesized like Samples D, but in an O_2-deficient environment. The solution was degassed for 15 min, but during transfer into a glove box, some O_2 could re-dissolve. The SEM micrographs Fig. 3.4 show about 10% of the Cu_2O surface covered with octahedral crystals of diameters between 0.3 and 0.7 µm, and partly with what seem to be incomplete CuBTC crystals with diameters of 100 to 200 nm (Fig. 3.4, red). This is the only sample for which we observe incomplete CuBTC octahedrons. It is unlikely that these crystals deposited onto the Cu_2O substrate during centrifugation; rather they must have grown at the surface, and their growth was halted prematurely due to lack of O_2. Similarly, also the few octahedral crystals (Fig. 3.4, blue) that we detect are visibly attached to the Cu_2O substrate. From these results, we conclude that O_2 is the necessary oxidant for the oxidation of Cu_2O to CuBTC without ec potential, as a reduction in the O_2 content of the solution leads to a significant decrease in synthesis yield. Furthermore, the visible connection between the CuBTC and the Cu_2O indicates that CuBTC nucleation and growth takes place directly at the solid/liquid interface.

Summing up, the first step to ec CuBTC formation is the oxidation of Cu to Cu^I achieved either by electrochemical oxidation of the Cu anode or by providing O_2 and/or H_2O (H_2O

enables CuBTC synthesis even under oxygen-free conditions[56]) as reactant. Furthermore, CuBTC forms directly from Cu^{1+}_2O powder while $Cu^{2+}O$ does not convert to CuBTC under the given experimental conditions.

Cu_2O is the predominant oxidation product of Cu in oxygen or water containing ethanol.[125] As known from literature, Cu_2O can be produced from Cu by the following oxidation reactions with H_2O or O_2:[118,119]

$$2Cu + H_2O \longleftrightarrow Cu_2O + 2H^+ + 2e^- \tag{3.1}$$

$$4Cu + O_2 \longleftrightarrow 2\ Cu_2O \tag{3.2}$$

A positive applied potential facilitates the net release of electrons in reaction (3.1). Excess electrons are transferred to the counter electrode where a not-further specified counter reaction takes place. Reaction (3.2) represents the aerobic oxidation of Cu that takes place in the presence of O_2 and even outside of solutions as evident through the oxide layer that covers copper metal within seconds of being exposed to air. In Samples B, both reactions (3.1) and (3.2) were blocked by using dry ethanol and by degassing the electrolyte with argon. Since all surface oxides were removed by acidic etching, no Cu_2O could be formed and ultimately no CuBTC could be produced.

In absence of O_2 and H_2O, the amount of available Cu^{I}_2O is expected to limit the CuBTC yield. Indeed, for Samples C where the amount of available Cu_2O was fixed, we did not observe continuous detachment of large MOF crystals from the electrode into the solution phase, which is usually visible through a constant stream of blue precipitate from the electrode surface into the solution. The lack of this observation indicates that CuBTC growth stopped after all provided Cu_2O had been consumed.

For the second oxidation step of Cu^{1+}_2O to $Cu^{2+}BTC$, we propose the following ec half reaction:

$$3\,Cu_2O + 4\,H_3BTC \longleftrightarrow 2\ Cu_3BTC_2 + 3\,H_2O + 6\,e^- + 6\,H^+ \tag{3.3}$$

H_2O is a likely product that can be produced from the oxygen released from Cu_2O and the protons released from BTC. In the ec synthesis, this oxidation half-reaction takes place at the Cu anode. (A corresponding, not further specified reduction reaction takes place at the

counter electrode.) With the production of H_2O, the overall reaction should be self-sustaining after a certain threshold H_2O concentration is reached by combining (3.3) with (3.1). For aerobic Cu_2O oxidation (Samples D), CuBTC growth occurs at the Cu_2O/solution interface. CuBTC synthesis from Cu_2O without applied potential is only possible in the presence of O_2, as shown by the greatly reduced amount of CuBTC in Samples E. Likely, O_2 is reduced to H_2O in a counter reaction that can again accommodate the protons released from the BTC molecules upon coordination to copper ions.

$$O_2 + 4\,H^+ + 4\,e^- \longleftrightarrow 2\,H_2O \tag{3.4}$$

Equation (3.3) as the key step in ec CuBTC synthesis as derived from our results is fully consistent with synthesis facts reported in literature: Van Assche et al. showed that CuBTC cannot be produced electrochemically in electrolytes that contain more than 50% H_2O.[56] The suppression of the reaction by too much H_2O is consistent with H_2O formation on the product side of (3.3), leading to an increase of the oxidation potential of the reaction while increasing the propensity for the formation of the H_2O-containing catena-triaqua-μ-CuBTC species that van Assche et al. observe.[56]

It should be noted that $Cu(OH)_2$ has also been shown to readily convert into CuBTC in presence of the linker BTC.[128] While $Cu(OH)_2$ as an intermittent, short-lived reaction intermediate cannot be excluded, our spectroscopic data does not indicate stable $Cu(OH)_2$ formation (i.e. no Raman band at 460 cm^{-1} that could be distinguished from the Cu_2O or CuBTC contributions, Fig. 3.2).

Let us summarize the reaction mechanism for the ec oxidation of Cu^0 to CuBTC: In presence of O_2 and/or H_2O, Cu is oxidized in a one-electron step to Cu_2O. A second oxidation step from Cu^I to Cu^{2+} in the presence of BTC directly converts Cu_2O to CuBTC. Involvement of an intermediate Cu(I) reaction step has not been proposed so far and opens up new pathways to increase control of the synthesis.

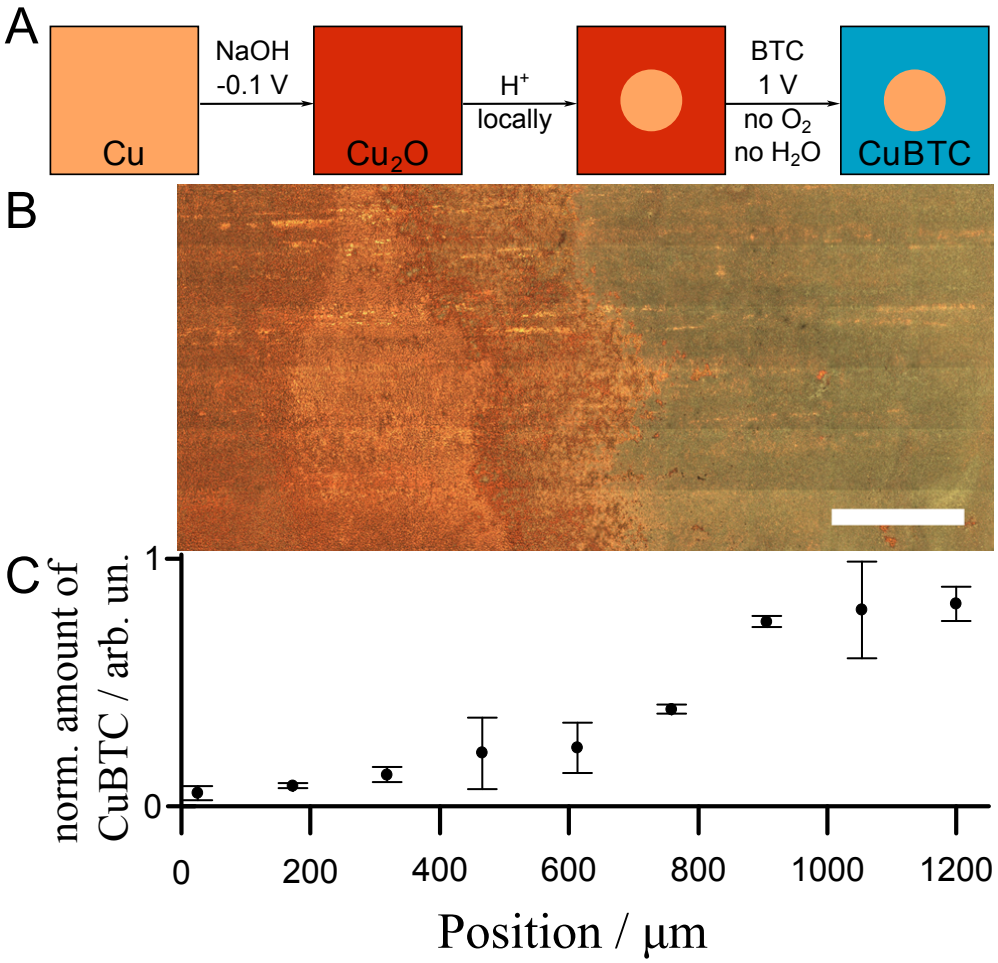

Figure 3.5 A: Scheme for the fabrication of patterned CuBTC devices by oxide patterning; B: light-microscopy image of a Cu sample (left) partly covered with CuBTC (right). Scale bar: 200 µm; C: normalized amount of CuBTC across the sample as taken from the integration of the Raman spectra between 800 and 850 cm^{-1} .

3.3 Fabrication of patterned MOF chips

Our newly gained knowledge that CuBTC crystallization and growth proceeds through intermediate Cu_2O formation allows us to suggest a novel method to fabricate patterned MOF devices (Fig. 3.5A). As a proof of principle, we prepared a Cu substrate with both Cu and Cu_2O present by electrochemically oxidizing the surface in the presence of NaOH.[129] Then, we selectively removed Cu_2O in a spot of ≈1 cm diameter in the centre of the sample by pipetting a drop of 10% HCl. After removal of that drop and subsequent rinsing with

MilliQ and EtOH, the Cu plate was covered with Cu_2O except for the acid-etched blank Cu area.

Under synthesis conditions B (O_2 exclusion, 1V applied potential), CuBTC was grown solely on the oxide-covered part of the sample as discernible in the white-light image taken through a 50x microscope objective (Fig. 3.5B). The left part of the image where surface oxides were removed by acidic etching shows the pristine Cu surface. To the right of the image, outside the area of the acid droplet, CuBTC has visibly grown (as evident through the greenish/blue coating on the surface) and is spectroscopically detectable in a Raman map of the surface. Raman band integration of the 800 to 850 cm^{-1} region provides the relative amounts of CuBTC at different sample positions (Fig 3.5C; error bars are standard errors of the mean of three measurements taken at roughly the top, middle and bottom of the white-light image). The data shows that we successfully prepared a patterned copper chip covered with CuBTC at positions that we can specifically choose prior to the synthesis. The procedure itself is currently rather crude, as for example the boundary between the two areas (MOF covered and MOF free) seems to be a broad continuum instead of a sharp border (see Fig. 3.5B and C) but it can serve as a starting point for new preparation pathways of patterned Cu-MOF devices.

3.4 Conclusion & Outlook

To conclude, we unraveled that CuBTC electrosynthesis proceeds in a two-step oxidation mechanism at the electrode surface: Cu is first oxidized to $Cu^{I}{}_2O$ in the presence of H_2O or O_2. Cu_2O is further oxidized to $Cu^{II}BTC$ in presence of the linker at the cuprite-electrolyte interface. We demonstrated how the gained knowledge can be used for a novel quick and versatile approach to produce patterned CuBTC devices.

Our facile oxide-based pre-patterning approach can serve as starting point to develop improved synthesis protocols for CuBTC patterning. Current patterning approaches require the use of Cu electrodes in the desired shape (i.e. printed circuit boards[50] or Cu meshes[56]). Our approach offers the possibility to subsequently activate parts of a Cu substrate. It is easy to imagine how established ways to deposit Cu_2O as nanoparticles or films[130,131] or

to selectively remove Cu oxide, as shown here, can be converted into a versatile basis for the fabrication of arbitrarily patterned surfaces on nm to mm length scales to create devices covered with MOF crystals of controlled sizes at predetermined spots.

Additionally other electrochemically grown MOFs with multivalent metal cations, such as MOF-5[132] or MOFs from the MIL-53 class,[51] should be investigated as to whether their mechanism occurs similarly to the two-step mechanism of CuBTC. If more MOFs are found, that follow this scheme, our patterning approach would open up the possibility of producing chips with different MOFs at predetermined spots on the sample, which could yield interesting applications in i.e. the preparation of multiplexed sensors.[133]

We now want to further investigate, why the CuBTC coatings we have investigated in this chapter grow on the surface of the electrodes as opposed to in the solution phase. To do this, we will investigate the electrochemical interface during CuBTC growth using EC-SERS as well as study the electrochemical deposition and oxidation of copper in BTC containing electrolyte.

Chapter 4

BTC adsorption on copper as the reason for on-surface growth of CuBTC

In this chapter we investigate the potential-dependent Cu-BTC interactions in EtOH and monitor the transition of BTC from a surface adsorbate on copper to an integral building block of CuBTC. Our study aims to find a molecular-level reason for the on-surface growth of CuBTC.

While some studies on BTC-metal interactions in aqueous electrolytes at different electrochemical potentials exist,[116,134] little is still known about the interaction of BTC with metal surfaces in organic solvents as commonly employed in MOF synthesis. Moreover, the potential-dependent metal-BTC interaction and its possible influence on the resulting framework properties, such as its surface adhesion, are unknown. Such knowledge would provide an important step toward rational planning of syntheses for functional MOF materials.

In order to fill this knowledge gap, we investigated the potential-dependent behavior of the Cu-BTC system. Using Au(111), a well-defined and reproducible substrate for electrochemical investigations, we performed cyclic voltammetry (CV) to observe the effect of BTC on the energetics of Cu electrochemistry ((underpotential-) deposition and oxidation) in EtOH.

We find that BTC has an energetically hindering effect on both copper deposition onto the underpotential-deposited copper layer as well as the oxidation of copper.

We complement our findings with EC-SERS experiments performed on polycrystalline Cu to obtain in-situ information about the potential-dependent adsorption characteristics of BTC on Cu. Starting from negative potentials up until the moment CuBTC formation starts above $E > 0$V we find an increase in the amount of BTC adsorbed to the surface.

Finally, we spectroscopically observe the potential-triggered transition of BTC from a surface adsorbate into an integral building block of a CuBTC above 0 V vs Cu. Over several minutes the amount of BTC adsorbed to the surface decreases while the spectra shift to match the Raman response of CuBTC. We think this gradual change shows that the strong propensity of BTC to adsorb to the copper surface is the reason for the on-surface growth of CuBTC during the electrochemical synthesis.

The following results have been accepted for publication in the Journal of Electroanalytical Chemistry.[1]

4.1 Experimental details

The Au(111) single crystal was obtained from small single crystal beads that were oriented, cut and polished by Clavilier's method.[135,136] The bead was produced by using a very small flame from a hand torch (propane-oxygen) to melt a Au wire and slowly cooling the melted bead.[137]

Electrochemical measurements on Au(111) were performed - with the much appreciated help of Paula Sebastian and Juan Feliu in Alicante, Spain - using a μ-Autolab III potentiostat in the current-integration mode. A Cu wire polished with fine-grit polishing paper prior to immersion in the electrolyte was used as a reference electrode. Flame-annealed Au wire was used as a counter electrode. All glassware was previously immersed in 40 % nitric acid over night and boiled in ultrapure water twice. All potentials are reported versus Cu.

[1] Schäfer et al., Trimesic acid on Cu in ethanol: Potential-dependent transition from 2-D adsorbate to 3-D metal-organic framework, Journal of Electroanalytical Chemistry (2017), DOI: 10.1016/j.jelechem.2017.01.025

The Au(111) working electrode was flame annealed before cooling in the Argon saturated atmosphere over the degassed electrolyte. Degassing was performed for at least 15 minutes. The single crystal was immersed at a potential of 0.6 V vs Cu and experiments were performed in the hanging-meniscus configuration.[138] The supporting electrolyte was 10 g/L MTBS in EtOH. For experiments with Cu^{2+} ions in the electrolyte, the solution contained 0.67 mM $Cu(NO_3)_2$ x 2.5 H_2O. When BTC was part of the electrolyte, the concentration was 75 mM. After every experiment the Au electrode was kept at a potential of 0.5 V for several minutes to remove residual Cu from the surface. The electrode was cleaned with 40% nitric acid, copious amounts of ultrapure water and flame-annealed before storage.

Raman measurements were conducted using a home-built electrochemical Raman cell (material: Kel-F) designed to seamlessly exchange the electrolyte through teflon tubings. The counter- and reference-electrodes were Pt wire. The potential of the Pt-electrode used during the Raman experiments is 0.1 V vs Cu, and the potentials of the Raman experiments have been converted accordingly to the Cu reference. The Raman set-up is detailed in section 2.2.2. Exposure times for the spectra were 10 seconds. A full spectrum was taken every 40 seconds. All reported spectra are background-corrected with an asymmetric least-squares algorithm,[111] normalized to the C-C stretch vibration band of EtOH at 882 cm^{-1} and smoothed with a Savitzky-Golay filter. The background correction was performed in Matlab, all other data evaluation steps were performed with self-written Python code. Potential-dependent spectra are averages of 7 to 10 spectra. Time-series spectra are not averaged.

For the in-situ Raman measurements the polycrystalline Cu working electrode was cleaned with 25 % hydrochloric acid, rinsed with copious amounts of ultrapure water and finally rinsed with EtOH prior to use. The electrolyte consisted of 0.032 M MTBS in 96 % EtOH / 4 % water and optionally 150 mM BTC as indicated. The cell was always first filled with pure MTBS-solution to perform a blank measurement. The electrode was afterwards kept at a constant potential of -0.4 V vs Cu while the electrolyte was exchanged to BTC containing one by hydrostatic pressure. The electrolyte exchange could be monitored through the current at the working electrode. The electrolyte was exchanged for at least 15 minutes before the measurement in BTC containing solution was started. Raman measurements were started within 5 seconds of adjusting the potential to a new value.

4.2 BTC inhibits copper deposition & oxidation on Au(111)

We conducted CV experiments to investigate the influence of BTC on the oxidation and desposition of Cu on gold. As a substrate, we chose a Au(111) single-crystal surface since its surface state can be easily recovered during the experiments by removing all deposited copper at high potentials ($\approx$ 0.5 V), ensuring maximum reproducibility of the results. In Figure 4.1, we show the CV responses of the Au(111) electrode in different electrolytes at a scan rate of 20 mV/s: The supporting electrolyte (grey triangles) is ethanolic MTBS. The corresponding CV shows no prominent features and is governed solely by a small capacitive current in the range of -10 to 10 $\mu A/cm^2$. A lack of strong current increase towards both ends of the CV (0.7 V in anodic direction and -0.7 V in cathodic direction) shows that the electrolyte and the gold electrode are stable in the chosen potential window.

Upon adding Cu nitrate to the electrolyte, the CV changes significantly (Figure 4.1, black line). The scan was started at 0.5 V vs Cu, a potential at which any Cu previously deposited on Au is oxidized so that the Au surface is a pristine Au(111). In the anodic direction, the current is slightly positive and shows a small increase until the scan reversal point at 0.7 V. The cathodic scan is featureless, with a slight negative slope of the current with decreasing potential till about 0.24 V where a small cathodic peak (**A**) is seen. Decreasing the potential further, a cathodic current shoulder appears at -0.1 V (**B**). Below -0.15 V, the cathodic current increases slightly again, forming a small current peak at around -0.25 V. The cathodic current density slightly drops from -0.125 mA/cm^2 at the peak to -0.115 mA/cm^2 where it forms a plateau **C** till reaching the lower vertex potential of -0.5 V. After the scan reversal, the current stays constant at around -0.110 mA/cm^2 until -0.2 V where it starts increasing slowly, showing a slight hysteresis behavior in the potential range from -0.2 to -0.1 V. At -0.05 V, the current increase becomes steeper (0.1 mA/cm^2 increase per 50 mV), leading to the formation of an anodic peak (**D**) at 0.11 V. At 0.32 V, a second anodic peak (**A'**) appears.

Introducing BTC into the solution leads to the CV shown as a grey line in Figure 4.1. Starting at a potential of 0.5 V, at a Cu-free Au(111), the anodic scan shows no features and only negligible anodic current until the first vertex potential at 0.7 V. After the scan reversal, a cathodic peak (around peak **A** for the BTC-free solution) with very low current (-17 $\mu A/cm^2$ vs the baseline of -7 μA) is detected at around 0.29 V. Scanning further, the trace stays flat

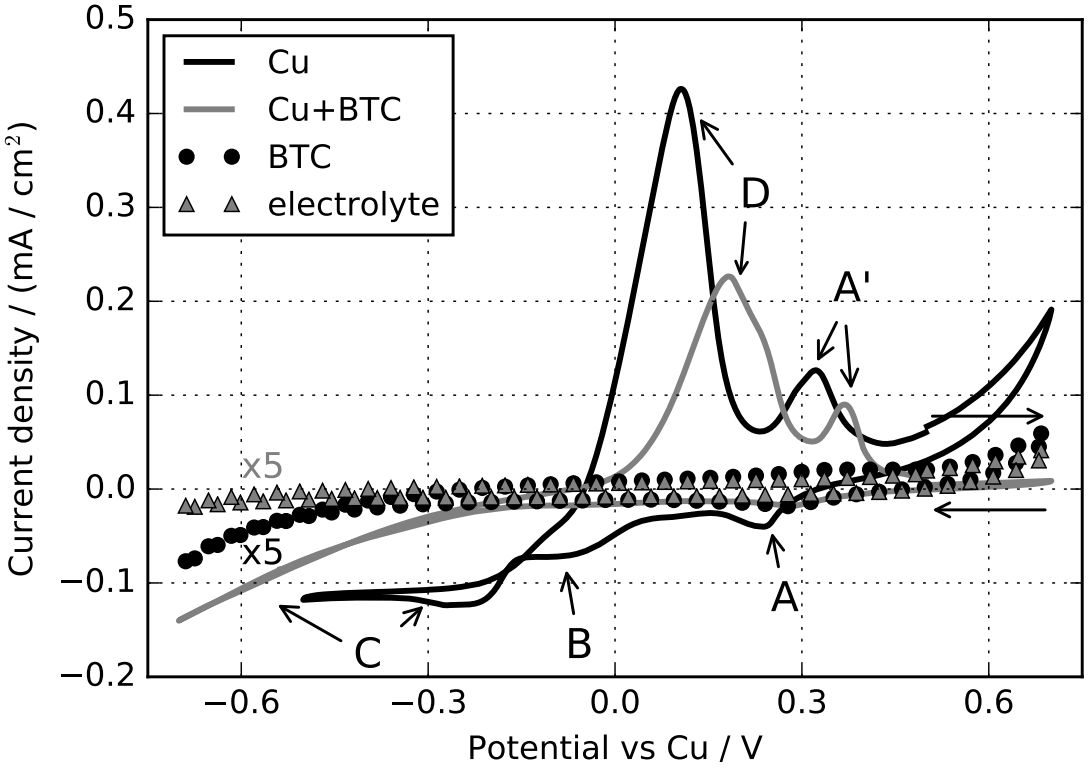

Figure 4.1 CV of Au(111) in supporting electrolyte with different additives. Grey triangles: pure supporting electrolyte (10 g/L MTBS in EtOH). Black line: supporting electrolyte + 0.7 mM Cu nitrate hemipentyhydrate. Grey line: supporting electrolyte + 0.7 mM Cu nitrate hemipentahydrate + 75 mM BTC. Black circles: supporting electrolyte + 75 mM BTC, $v = 20$mV/s. The current densities for the pure supporting electrolyte and for the supporting electrolyte + BTC have been multiplied by 5 for clearer display.

and slightly negative until the cathodic current starts to increase below -0.2 V. The cathodic current increases almost linearly below -0.4 V (**C**) till the lower vertex potential of -0.7 V. The anodic scan shows a similar behavior, with a slowly decreasing cathodic current until around -0.1 V where the trace levels off. Just positive of 0 V, a large anodic peak begins (**D**) which reaches its maximum current at 0.18 V. The anodic flank of the peak shows a slight shoulder, and a second anodic peak (**A'**) appears at 0.37 V.

As 0 V is the equilibrium potential for the oxidation and reduction of Cu^{2+} to Cu in our Cu-referenced system, we conclude that features **B** and **C** in the CVs of Cu nitrate in EtOH (Figure 4.1, black line) concern the reduction of Cu and subsequent deposition on the Au

surface. The shoulder **B** is possibly a prereduction of Cu^{2+} to Cu^{+}. Peak **D** corresponds to the oxidation of this Cu layer on the electrode (most likely to Cu^{2+}). The peak-pair **A** and **A'** are the anodic and cathodic sides of the same reaction, since peak **A'** is absent in experiments that do not scan below 0.3 V (not shown). Both features (**A** and **A'**) are also absent in experiments without Cu as evident from the comparison with the CV in pure electrolyte (Figure 4.1, grey triangles). Therefore these features should also be a reduction and oxidation of copper. As the reduction potential is found at higher potentials compared to the bulk reduction **C**, it is reasonable to conclude that the peaks **A** and **A'** belong to an underpotential deposition (UPD) process of Cu on the Au electrode, similar to what is observed in aqueous Cu salt solutions.[139] An observed deposition potential of 0.24 V vs Cu closely matches the potential of 0.21 V vs Cu/Cu^{2+} previously observed in aqueous sulfuric acid solution.[140] It should be noted that even after multiple scans, the first CV can be reproduced, meaning that the Au(111) surface is free of residual Cu above 0.4 V. If Cu remained on the surface, we would expect changes in subsequent CVs.

The CV features described after introducing BTC into the solution (Figure 4.1, grey line) are similar to the ones that we observe in the solution that does not contain BTC. Noteworthy is the absence of the shoulder **B** and the changes in the deposition peak **A** of the Cu UPD. The small peak observed around 0.3 V in cathodic scan direction where we expect to see the deposition of the Cu UPD is also observed (albeit with lower current density) in solutions containing only BTC and no Cu (Figure 4.1, black circles). The peak observed at 0.3 V could therefore either be the Cu UPD peak, a peak from BTC (or an impurity in the BTC) or a combination of both. The features **C**, **D** and **A'** are assigned to the same phenomena as in BTC-free solution, namely Cu bulk deposition, Cu bulk oxidation and the stripping of the Cu UPD layer.

The comparison of the CVs recorded in presence and absence of BTC reveals differences in the positions of peaks and their general shape. First, the two peaks (**D**, **A'**) are shifted towards more positive potentials and peak at lower current densities. The assigned UPD stripping peak **A'** is found 48 mV higher in the BTC containing case while the Cu oxidation peak **D** is shifted by +75 mV. The current corresponding to Cu deposition (**C**) increases much more slowly in the presence of BTC and the marked plateau features of the BTC-free CV are missing.

The presence of BTC causes an overpotential for both the deposition of Cu, as indicated by the slower and delayed rise of the cathodic currents at negative potentials, and the corresponding Cu oxidation, as evident by the shift of peak **D** to more anodic potentials. The lower anodic currents in all oxidation peaks can be explained by the lower amount of deposited Cu (due to the lower cathodic deposition currents during phase **C**). Likely, the induced overpotential stems from an adsorption of BTC on the Cu surface at potentials lower than 0 V. Adsorption of BTC to the surface below 0 V would explain the delayed and slowed down deposition of Cu, since Cu electrodeposition is known to be diffusion-limited[141] and BTC would act as a diffusion barrier for Cu^{2+} ions, effectively shielding the electrode from the deposition. BTC therefore adds an overpotential to the Cu reduction and deposition, an additional energy contribution needed for the displacement of the BTC. After Cu has been deposited, BTC could adsorb onto the Cu layer, stabilizing the surface and therefore energetically hindering Cu oxidation above 0 V. The shift in the UPD stripping peak **A'** can also be explained through Cu-BTC interactions, assuming that at least part of the BTC is deprotonated upon adsorption. It has been shown that anions that strongly interact with Cu^{2+} ions and Cu can shift the CuUPD process to higher potentials.[142] The possible absence of the UPD reduction peak **A** could be explained by an adsorption of BTC to the Au surface at positive potentials, as has previously been reported for the Au-aqueous electrolyte interface.[134] As the BTC adsorbs onto the blank Au surface, it blocks the monolayer UPD of Cu onto Au(111) similar to the bulk Cu deposition as discussed earlier.

4.3 Potential-dependent adsorption behavior of BTC on Cu

To gain chemical insight into the interaction of BTC with the Cu surface and confirm our theory about the adsorbed BTC layer on Cu, we performed EC-SERS on polycrystalline Cu electrodes. As we want to be entirely sure that we only probe specific interactions between Cu and BTC, we do not perform these experiments on the Cu(UPD)/Au system introduced before. On the Au(111) surface we could not be sure that the spectral response does not also originate from copper-free parts on the surface. The experiments were performed in

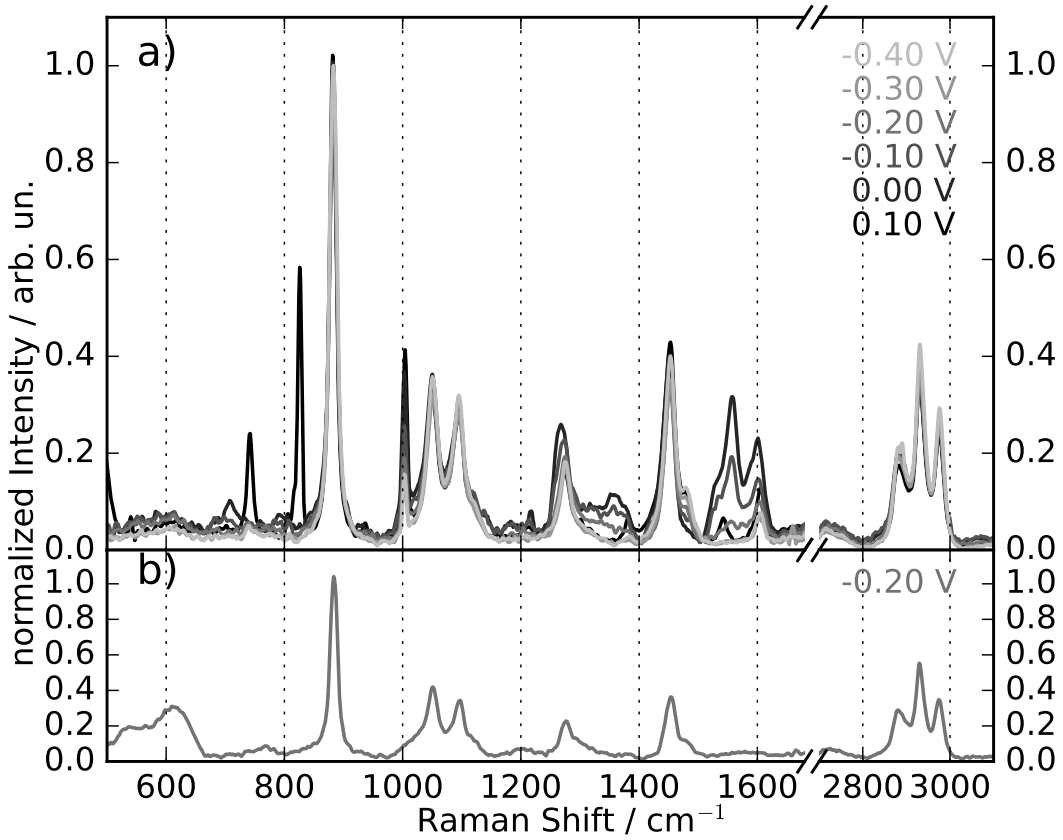

Figure 4.2 a) EC-SER spectra of polycrystalline Cu in 75 mM BTC + 10 g/L MTBS in EtOH with increasing potential (bright to dark). b) EC-SER spectrum of polycrystalline Cu in 10 g/L MTBS in EtOH at -0.2 V. All spectra are normalized to the C-C stretch mode of ethanol at 882 cm^{-1}.

the potential region from -0.4 V to +0.1 V vs Cu, the area in which we see the strongest differences in the CV experiments between BTC containing and BTC-free solutions.

Figure 4.2 a) shows an overview of EC-SER spectra taken at different potentials in BTC containing electrolyte. For comparison, Figure 4.2 b) shows the spectrum of Cu in the BTC-free supporting electrolyte MTBS in EtOH at -0.2 V. The spectrum of the supporting electrolyte does not change with the applied potential in the chosen potential region between -0.4 and 0.1 V. As there is no BTC present, all Raman signals in 4.2 b) originate either from the solvent (ethanol), the supporting electrolyte (MTBS) or the copper surface. We will not discuss these signals in-depth, as we are primarily interested in the interaction of BTC with the copper surface.

We will first generally describe the spectral regions that change upon addition of BTC and with the applied potential and discuss specific bands in detail later (Figures 4.3 and 4.4). There are four areas in the spectrum that show changes in the EC-SER response upon BTC addition to the electrolyte. Between 500 and 650 cm^{-1}, we observe two broad peaks in Figure 4.2 b) that are absent in the corresponding spectra in Figure 4.2 a). Upon addition of BTC, these bands disappear and only reappear with reduced intensity at higher potentials. The second area of interest lies between 725 and 850 cm^{-1}. Here, we observe two bands with high intensity in BTC containing solution at 0.1 V. These bands are undetectable in any spectra between -0.3 V and 0 V and only appear in BTC-containing solution. In the third area of interest between 1530 and 1610 cm^{-1}, we observe new bands at all investigated potentials that are not present in the spectrum of the pure supporting electrolyte. Lastly, at 1002 cm^{-1} we observe a new band in the presence of BTC. The intensity of this band increases with more positive potentials. The changes in the area from 1300 to 1400 cm^{-1} are artifacts of the background removal during data processing and will therefore not be discussed further. We will now first focus on the area between 1500 and 1650 cm^{-1} and describe the potential-dependent changes in the peak structure in depth.

Figure 4.3 a) shows a zoom of the EC-SER spectra obtained at different potentials in the region from 1500 cm^{-1} to 1670 cm^{-1} in BTC containing electrolyte. The spectra show two distinct peaks, one around 1560 cm^{-1} (peak A) that cannot be detected at all potentials, and one around 1605 cm^{-1} (peak B) present in varying intensity at all investigated potentials. The right side of Figure 4.3 shows the peak positions and maximum peak intensities obtained from fitting the bands with two Lorentzian profiles. Figure 4.3 b) and c) show the positions of peak A and B, respectively. Figure 4.3 d) shows the maximum peak intensities of both peaks normalized to their respective maximum intensities in the measured potential window. Peak A cannot be distinguished from the noise at potentials below -0.25 V. The position of peak A shows slight variations between 1555 and 1553 cm^{-1} in the range from -0.25 V to 0 V. After crossing the 0 V threshold, the peak red-shifts to 1541 cm^{-1} at 0.1 V. The general trend of the shift is opposite for peak B. The peak position starts at 1605 cm^{-1} at -0.4 V and gradually red-shifts to 1601 cm^{-1} at 0.0 V. After crossing the threshold, it blue-shifts back to 1605 cm^{-1} at 0.1 V. The shifts of the two peaks span a range of 14 and 4 cm^{-1} for peak

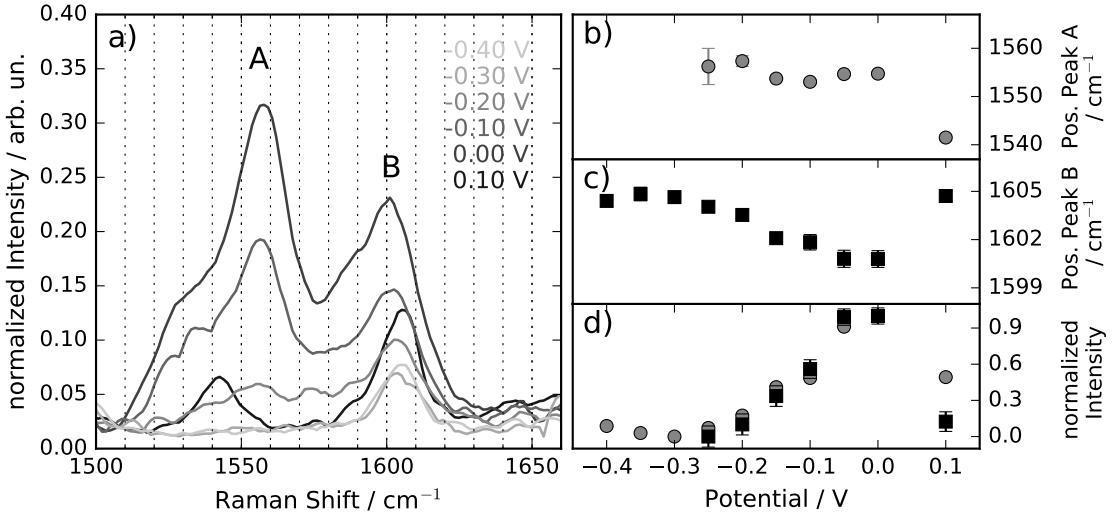

Figure 4.3 a) Zoom of the EC-SER spectra in the area from 1500 to 1660 cm^{-1} at different potentials. Right: Results of a Lorentzian fit of the area from 1500 to 1660 cm^{-1}: **b)** & **c)** fitted peak maximum position of peaks A and B, respectively, as a function of potential. **d)** maximum peak intensity of peaks A (grey, circles) and B (grey, squares) relative to the respective peak's maximum observed intensity in the given potential window. Peaks B in the EC-SER spectra at -0.4 V, -0.35 V and -0.3 V were fitted with a single Lorentzian since peak A is absent in these spectra. Error bars are errors of the fits.

A and B, respectively, meaning that the position of peak A is more strongly affected by the applied potential than that of peak B.

The change in peak intensity with varying potential shows the same trend for both peaks. While peak A can only be distinguished above -0.3 V, both peaks rise monotonously in intensity and reach their maximum intensities at 0 V. At 0.1 V, the peak intensities are significantly lower. The increase of the peak intensity at more positive potentials is reversible in the sense that changing the potential from -0.2 V to -0.1 V and back shows a reversible increase and decrease in the signal (data not shown). We observe that for high intensities (-0.1 V and 0 V in Figure 4.3, left), peak A has a shoulder around 1530 cm^{-1}. The spectra below 0 V and at 0.1 V are stable over the time frame of the experiment (5 minutes). We do not show the fit results of an average spectrum at 0.05 V here since the EC-SER response shows large changes over time which we will describe in detail later (see Section 4.4).

The potential-dependent EC-SER spectra in Figure 4.2 confirm our hypothesis of adsorbed BTC on the Cu surface. Peaks A and B are assigned to the symmetric C-O_2 stretch vibration

and C-C ring vibrations of BTC, respectively.[87] The increase in the band intensities of peaks A and B reflects an increase in the amount of BTC at the electrode at more anodic potentials. The peak at 1002 cm^{-1}, which is assigned to the ring breathing motion of BTC,[116] shows the same behavior as the 1550 and 1604 cm^{-1} bands with increasing intensity at higher potentials (data not shown in detail). From the observed increase in Raman band intensities between 1500 and 1610 cm^{-1} with higher potentials, we conclude that more BTC adsorbs on the Cu surface at more positive potentials. The band position changes of peaks A and B during the formation of the increasingly dense BTC adlayer could reflect adsorption geometry changes such as molecules standing up at more positive potentials as the adlayer needs to accomodate more molecules.[143] The presence of the shoulder at 1530cm^{-1} at high potentials (and thus higher BTC concentrations at the interface) further supports this idea. Assuming the shoulder corresponds to the same molecular vibration as the main peak A, the shoulder could mean that there are actually two kinds of differently adsorbed/oriented BTC molecules at the surface. Different molecular orientations would lead to slightly different bonds of the BTC to the Cu surface with respect to strength of the bond and directionality. As detailed in 2.2.2, this can lead to changes in the position of Raman bands. Especially the vibrations including the C-O_2 group (peak A) are expected to change upon changes in the bond between molecule and metal, as the carboxyl group is the expected binding moiety in the molecule. The changes in the position of peak A are larger (in the range of 14 cm^{-1}) than those of peak B (4 cm^{-1}). For peak B, corresponding to C-C ring vibrations, no strong dependence of the molecular vibration to the bond between the metal and the molecule is expected. The slight changes that we do observe can be explained through the delocalized electrons in the aromatic BTC molecule. Changes in the electron density at the edges of the ring (due to a bond to the metal) can have a small effect on the bonds in the rest of the molecule.

Our observation of an increase of the amount of BTC adsorbed to the Cu at more positive potentials matches previous reports for the Au(111)-electrolyte interface. In aqueous solution, BTC switches from being physisorbed to Au at lower potentials to being chemisorbed at higher potentials.[144] This change coincides with a gradual increase in the surface coverage of adsorbed BTC at more positive potentials. In our system, according to the EC-SER data, the BTC surface coverage is highest in the potential range from -0.05 V to 0 V. Comparing

these potentials of maximum BTC coverage to the steep increase in anodic current in the CVs (Figure 4.1), we see that in BTC-free solution at -0.05 V, Cu oxidation already starts. More importantly, in BTC-free solution, there does not seem to be a potential at which neither oxidation nor deposition of Cu take place. The current trace goes from a slightly decreasing cathodic current just below -0.05 V to a quickly increasing anodic current without a period of low electrochemical activity. In BTC containing solution, however, the change in anodic current is more gradual and the current trace is almost flat around -0.05 V. Only after crossing 0 V, we observe a significant increase in the slope of the current trace. This coincides with the potential range of maximum BTC coverage as observed with EC-SERS at -0.05 and 0 V. We thus conclude that the adsorbed BTC that we observe using EC-SERS stabilizes the surface and induces an overpotential for Cu oxidation, as observed in our CV experiments (Figure 4.1).

It should be pointed out, that the CuUPD investigated in the CV experiments and the bulk Cu substrate in our EC-SERS experiments are not necessarily directly comparable. The behavior of the UPD is expected to lie between the behavior of an Au surface and a bulk Cu surface, as the reason for the occurrence of a UPD is the fact, that the deposition of the first layer of Cu onto Au(111) is energetically favorable compared to the bulk deposition. However, as BTC adsorption has been shown for the Au-electrolyte interface in literature and we have shown the adsorption at the Cu-electrolyte interface based on our EC-SERS measurements, we do believe the CuUPD results to be transferable to the bulk Cu system.

4.4 Potential-triggered transformation of the BTC adlayer to CuBTC MOF

While Figure 4.3 shows a significant change in the EC-SERS response of BTC/Cu after crossing a potential of 0 V, we now want to further investigate what happens just above 0 V. Figure 4.4 a) shows the Raman signal evolving over time at 0.05 V both in the previously explored area from 1550 to 1670 cm^{-1} as well as in the spectral region from 725 to 860 cm^{-1}. A spectrum was taken every 40 seconds. For clarity, only a selected number of spectra are shown in the overview on the left. We can see that in the area from 725 to 860

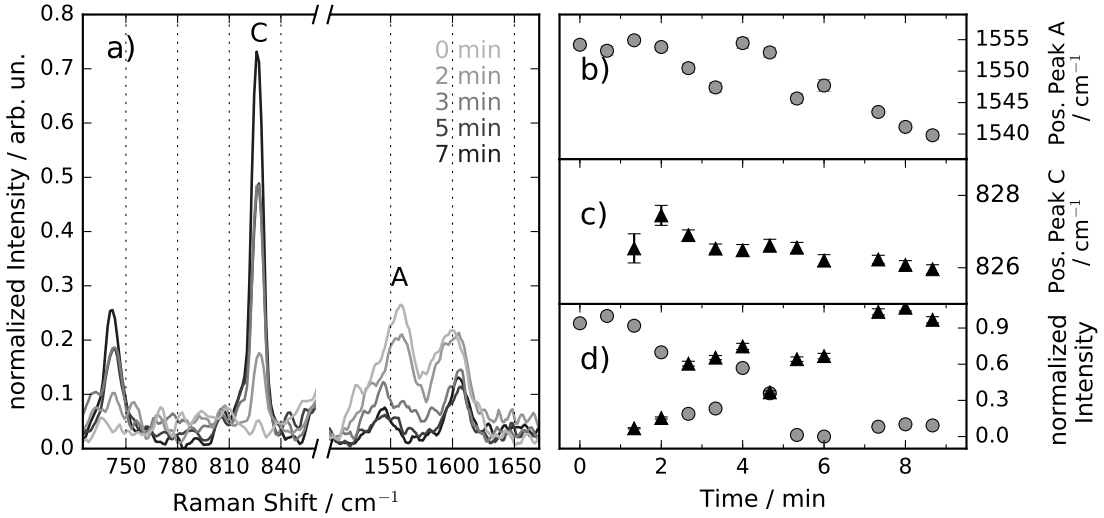

Figure 4.4 a) Zoom of the EC-SER spectra in the areas from 725 to 860 cm^{-1} and from 1500 to 1670 cm^{-1} at different times after switching the potential to 0.05 V. Darker spectra were taken at later times after the potential step. Right: fit results for peaks A and C. **b)** & **c)** Fitted peak-maximum position of peaks A and C, respectively, at different times. **d)** Fitted maximum peak intensities of peaks A (grey, circles) and C (triangles, black), normalized to the respective peak's maximum observed intensity in the experimental timeframe. Error bars are errors of the fits.

cm^{-1}, two peaks appear after 2 minutes and increase in intensity throughout the experiment. Meanwhile in the higher wavenumber region, the previously described peaks A and B change considerably.

Figure 4.4 b) shows the frequency shift of peak A in detail over time. The position of peak A shifts from 1555 cm^{-1} to 1540 cm^{-1} over the 10-minute time period. The intensity of peak A (Figure 4.4 d), grey circles) shows a slow decrease over time. The observed frequency shifts and intensity changes of peak A reflect the transition from the previously discussed spectrum at 0 V to the final spectrum at 0.1 V (Figure 4.3). Figure 4.4 c) displays the time-dependent position of peak C whose changes are within 1 cm^{-1}. The intensity of peak C (Figure 4.4 d), black triangles) increases at a similar rate as the intensity of peak A decreases. In the beginning, peak C is not distinguishable from the noise, and only starts being visible after 80 seconds. The intensity increases with time, albeit not monotonously. After 7 minutes, the intensity stabilizes and shows no significant changes over the last 2 minutes of the experiment.

In fact, the whole spectrum shows only small changes throughout the last two minutes of the experiment.

The EC-SER response (Figure 4.4) allows us to follow the potential-triggered transformation of the BTC adlayer into the crystalline 3D MOF structure of CuBTC in situ. Increasing the potential activates the BTC/Cu interface to form a new hybrid (MOF) structure where the metal ion-molecule complex is the elemental building unit as identified by the bands at 740 and 826 cm^{-1} assigned to characteristic C-H stretch vibrations of CuBTC (see section 2.2.2).

The similar rates in band intensity decrease at 1550 cm^{-1} (adsorbed BTC) and increase at 826 cm^{-1} (BTC in CuBTC MOF) indicate that the MOF is formed at roughly the same rate as the adsorbed BTC is consumed. After 10 minutes reaction time at 0.05 V, peaks A and B perfectly reflect the Raman response of pure CuBTC. The red-shift of the ν_{asym}C-O_2 band during the synthesis of CuBTC can be explained through the influence that coordinated Cu atoms and/or ions have on the C-O_2 bond strength. The Cu in CuBTC is in oxidation state +2, the coordination of BTC to Cu ions pulls electron density out of the C-O_2 bonds. On the Cu electrode surface, BTC coordinates to metallic Cu(0) where the electron pull is much weaker. The change leads to the observed band shift.

It should be noted that we only detect the EC-SER signature of Cu_2O in BTC containing solution with low intensity and at higher potentials. We observe the broad 515 and 615 cm^{-1} bands of Cu_2O clearly in the BTC-free supporting electrolyte (Figure 4.1 b)), but upon flushing the cell with BTC containing electrolyte, the Cu_2O signature disappears. Likely, the slightly acidic linker helps to dissolve the Cu_2O, forming either Cu or Cu^{2+} depending on the applied potential, and water. At higher potentials the spectrum shows a very slight increase in the Raman scattering in the region around the Cu_2O bands. This is consistent with our results on Cu_2O as a necessary intermediate in the electrochemical synthesis of CuBTC (see Chapter 3). The findings presented here suggest that the Cu_2O intermediate is significantly destablized in the presence of BTC as its amount is reduced compared to the BTC-free solution. The protons from the linker molecules most likely help etching the Cu_2O, producing Cu^{2+} in the process which can then form CuBTC.

4.5 Conclusion & Outlook

The potential-dependent interaction of BTC with Cu in ethanolic electrolyte has been investigated. Cyclic voltammetry shows an energetic delay of Cu deposition and oxidation in the presence of BTC, suggesting the formation of a molecular adlayer of BTC at the metal surface that induces an overpotential for the deposition of bulk Cu and the oxidation of the Cu layer. EC-SERS confirms the existence of adsorbed BTC on Cu below 0 V vs Cu. The surface coverage of the adsorbed BTC layer depends on the applied potential where more anodic potentials lead to a higher amount of adsorbed BTC. Above 0 V, we observe a transformation within ten minutes of BTC adsorbed at metallic Cu(0) to complexed BTC-Cu(2+) in the form of CuBTC.

This is to our knowledge the first time spectroscopic insight into the electrochemical interface during electrochemical CuBTC synthesis is presented. Additionally, for the first time, a BTC-metal interaction prior to the oxidation of Cu is reported for this system. The adsorption of BTC at Cu prior to MOF formation could be the explanation for the commonly observed strong adhesion of CuBTC to the Cu electrode, a fairly unique property of electrosynthesized CuBTC compared to other electrochemically produced MOFs.[51] The linker molecules that are adsorbed to the surface could present a seeding layer for the attachment of the first Cu^{2+} ions and therefore inherently link the growing MOF with the surface. We currently do not know, whether a BTC layer also forms on the cuprite intermediate that we observe for the synthesis of CuBTC (see chapter 3) or whether Cu oxidation to Cu^{2+} and attachment to the surface might happen at different positions on the sample simultaneously. While we do observe a slight increase in the signal for Cu_2O at more positive potentials in our EC-SERS spectra, the spatial resolution of EC-SERS ($\approx$ 300-500 nm) does not allow us to distinguish between both Cu_2O and BTC being present at different places in the laser focus or actually occurring together at the same position on the Cu surface. A spectroscopic technique with a better spatial resolution, such as electrochemical Tip-Enhanced-Raman Spectroscopy (EC-TERS)[145,146] with spatial resolution in the range of 10-20 nm, could help answer this question.

In the ongoing search for new surface-anchored, electrosynthesized MOFs, based on our results, we advise looking for other metal-linker combinations where a strong adsorption of

the linker to the surface of the metal (or a metal oxide) is to be expected, such as i.e. amine functionalized linkers on zinc oxide surfaces.[147,148] These combinations could prove to be valuable starting points for the rational planning of MOF coating syntheses.

Until now we have focused on the early stages of CuBTC growth in unraveling the oxidation mechanism of Cu (chapter 3) and the adsorption of BTC to the surface prior to electrochemical growth. We now shift our focus to the solution phase chemistry between Cu^{2+} and the linker to further investigate how the growth proceeds from these early stages. We aim to understand the reason for the high rate of the electrochemical synthesis when compared to other synthesis methods, such as the solvothermal synthesis.

Chapter 5

Kinetics and complex chemistry of CuBTC growth

In this chapter we study the room-temperature growth kinetics of CuBTC in solution and gain insight into the coordination chemistry during the synthesis. In Appendix A we briefly show that we can extrapolate the mechanism of solution-based CuBTC growth to the electrochemical growth. We aim to understand why the electrochemical synthesis of CuBTC is much faster than the commonly used solvothermal approach. In addition our results facilitate the design of more efficient MOF production facilities through insight into the kinetics of the MOF formation mechanism and possible side reactions.

The crystallographic properties of MOFs, such as their morphology and underlying crystal structure, and the coordination geometry within the crystal are routinely investigated when a new material is synthesized.[149,150] The supposedly rich but very hard to assess coordination chemistry during the synthesis of the material is rarely studied. This leads to a gap in our knowledge about the elementary reactions during MOF synthesis, making the development of predictable synthesis strategies difficult to impossible.

While nucleation and growth of CuBTC crystals has been studied in-situ using for example X-Ray diffraction[69] or light scattering[75] little is known about the coordination chemistry during the synthesis. It is, unclear if the copper paddlewheel, the secondary building unit of CuBTC, is the only possible complex that Cu^{2+} and BTC can form in the synthesis solution

or if there might be intermediates/side-reactions to the formation of the paddlewheel and ultimately the MOF. We set out to understand the coordination chemistry during homogeneous CuBTC nucleation and growth from its basic components Cu^{2+} and BTC and connect our results to the electrochemical synthesis. For the first time we study how the interplay of these components can change the kinetics of CuBTC formation.

While previous kinetic investigations have mainly focused on the effect of the synthesis temperature at fixed concentrations,[74] in this chapter, we investigate the effect different reactant concentrations have both on the general kinetics of room-temperature CuBTC growth as well as on the chemical composition of the solution. We combine our experimental data with a chemical reaction model that we numerically evaluate in order to gain clearer understanding about the role of the different chemical species during the synthesis. The model shows good qualitative agreement with the experimental results. Finally we investigate the effect the different concentration conditions have on the final product of both the solution-based synthesis as well as the electrochemical synthesis and explain the results in the framework of our reaction model.

The following results are being prepared for submission to *Chemical Communications*. Appendix B contains supporting information for this chapter.

5.1 Experimental details

We use ethanolic solutions of varying BTC and copper nitrate concentrations and measure their UV/VIS absorbance over a time period of multiple hours with a temporal resolution of 90 seconds. The copper concentrations we used are generally about 2 orders of magnitude below what is usually used in the synthesis of CuBTC (1 mM vs 100 mM) in order to slow down the reaction to match the temporal resolution of our experiment. The UV/VIS spectra were measured using an integration sphere setup (as explained in section 2.2.1).

For each experiment the cuvette was cleaned using first 2% HCl to remove residual CuBTC, then 3 rounds of rinsing with MilliQ water and finally another 3 rounds of rinsing with absolute ethanol. The cuvettes were dried in a nitrogen stream. The cuvette pathlength was 5 mm.

The cuvettes were always filled in the same order: First a certain amount of 0.032 M MTBS in absolute ethanol was filled into the cuvette. Then the necessary volume of 0.013 M $Cu(NO_3)_2$ x 2.5 H_2O in absolute ethanol was added to obtain the final desired concentration of Cu^{2+} ions in solution. Finally a solution of 0.15 M BTC and 0.032 M MTBS in absolute ethanol was added to set the final concentration of BTC. The total final volume prepared and filled into the cuvette was always 1.5 mL. Since the amount of $Cu(NO_3)_2$ solution added is in the range of only 100 µl the MTBS concentration can be assumed to be equal for all experiments and should therefore not have an effect on the reaction. The cuvette was closed with a teflon cap and shaken for 10 seconds before it was placed into the instrument and the measurement was started. The total time between the addition of the BTC and the start of the measurement is below 20 seconds. The blank reference for every measurement was a solution of the same composition without the copper nitrate.

A new spectrum was taken every 90 seconds. Acquisition of one spectrum took roughly 85 seconds since the detector wavelengths were scanned for the measurement.

5.2 Kinetic traces of CuBTC growth from UV/VIS experiments

Figure 5.1 shows results of a time-resolved UV/VIS absorbance experiment measured in a solution containing 1 mM Cu^{2+} and 18 mM BTC. Figure 1 a) shows raw spectra. The first spectrum (shown in the lightest grey hue) shows a UV/VIS spectrum with a single peak with a maximum value around 0.025 abs. un. at 800 nm. As time progresses, the overall intensity of the spectrum increases. The increase is mainly due to the appearance of a second peak around 710 nm that increases in intensity over time ending at 0.1 abs. un. after $\approx$ 100 minutes. The increase in the peaks intensity is accompanied by a rise in the spectrum around 500 nm.

The first spectrum, measured around 20 seconds after mixing the solutions, closely matches the spectrum of a pure $Cu(NO_3)_2$ x $2.5H_2O$ solution of the same concentration (1 mM, see Appendix B Figure B.2). The initial copper species is the same as in a BTC free solution. This species is most likely a Cu^{2+}-hydrate-nitrate complex, a Jahn-Teller distorted

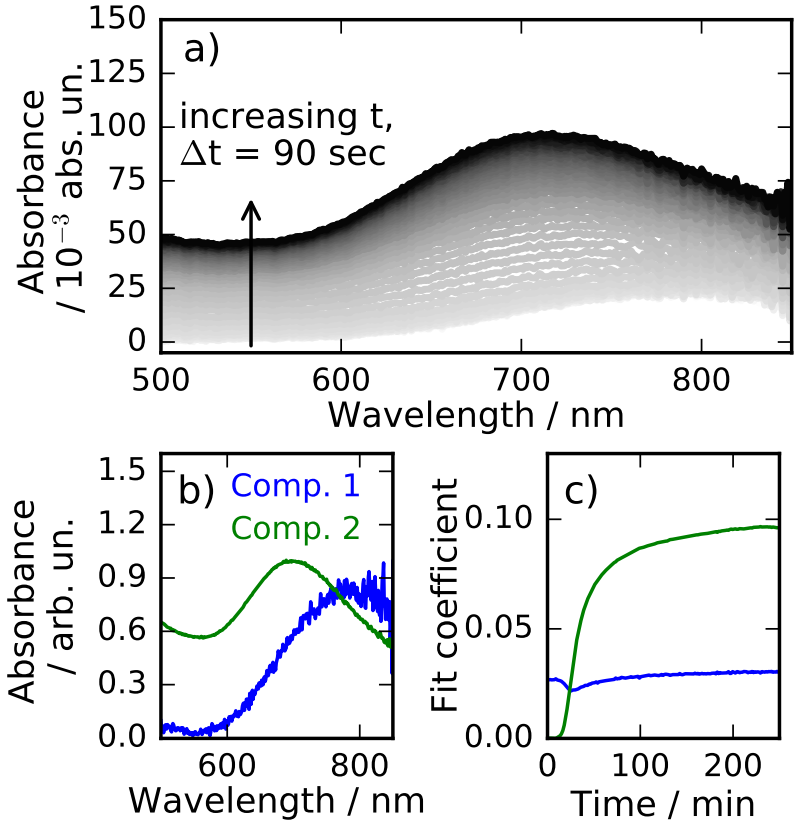

Figure 5.1 Overview over a single UV/VIS kinetic measurement. a) UV/VIS absorption spectra taken 90 seconds apart in a solution containing 1 mM Cu^{2+} and 18 mM BTC. Darker spectra were measured at later times. b) Spectra taken as the two component spectra for the non-negative least squares fit as described in equation (1) in Appendix B. c) Evolution of the fit coefficients (normalized to their maximum value) for the two components over the time of the experiment.

octahedral complex with ethanol/water in the equatorial positions and the labile nitrate in the axial positions.[151] The absorption stems from a d-d transition in Cu^{2+}. The last spectrum measured, with its absorbance peak at 710 nm matches the d-d transition of the MOF CuBTC reported in literature.[88,152] To investigate the kinetics of the synthesis of CuBTC, we deconvolute the spectral contributions of the precursor and CuBTC. Figure 5.1 b) shows the two normalized spectra that were used for a non-negative least squares (NNLS) fit on the experimental data to extract the spectral contributions. Component 1 is $Cu(NO_3)_2$ x 2.5 H_2O in ethanol. The second spectrum is taken from a separate NNLS fit with a free

floating spectral component as detailed in the Appendix section B.3. This component is identified as CuBTC.

According to Beer's law, the measured absorption is directly proportional to the concentration of a chemical species ($A = \varepsilon \cdot c \cdot d$, with ε the molar absorbance coefficient, c the concentration, and d the thickness of the cuvette). We treat the measured spectra as superpositions of the two component spectra weighted by a fit coefficient taken from the NNLS fit that is proportional to the concentration of the species in the solution.

Figure 5.1 c) shows traces of the NNLS fit coefficients taken from the experiment. The NNLS was run for every single spectrum of the experiment and the extracted fit coefficients were plotted against the time the respective spectrum was taken from starting the measurement. Starting with the coefficient of component spectrum 1 (blue), we see that the coefficient is maximum at the beginning of the experiment. After a short amount of time ($\approx$ 10 minutes), the coefficient starts decreasing with increasing speed. After 20 minutes a minimum is reached after which the contribution increases again. The coefficient for component spectrum 2 (green) is 0 in the beginning. After an induction period of 10 minutes, where almost no changes can be observed, its contribution starts increasing, reaching its maximum slope after around 25 minutes until it starts leveling off, approaching saturation at around 0.1 after 100 minutes.

The profile for the precursor (component 1) can be explained if we take into account that the spectrum of component 2 is derived as a free-floating component from a NNLS fit with a known component and experimental data as input. Our deduced CuBTC spectrum (component 2) is expected to lack intensity in the high wavelength region (800-850 nm), as the intensity in that region can mathematically also be gained by increasing the contribution of component 1. The 'true' spectrum of CuBTC will be a linear combination of component 2 with a small contribution of component 1. Therefore, the contribution of component 1 will mathematically increase as the amount of CuBTC increases in solution. Reliable information about the precursor is lost. In this example experiment the point at which the reliable information is lost is estimated to be around the time we start seeing in increase in the apparent concentration of component 1 after around 20 minutes. We will not discuss the concentration traces for component 1 (they are shown in Figure B.3) as the important information lies in the kinetics of the production of CuBTC, thus component 2 which only

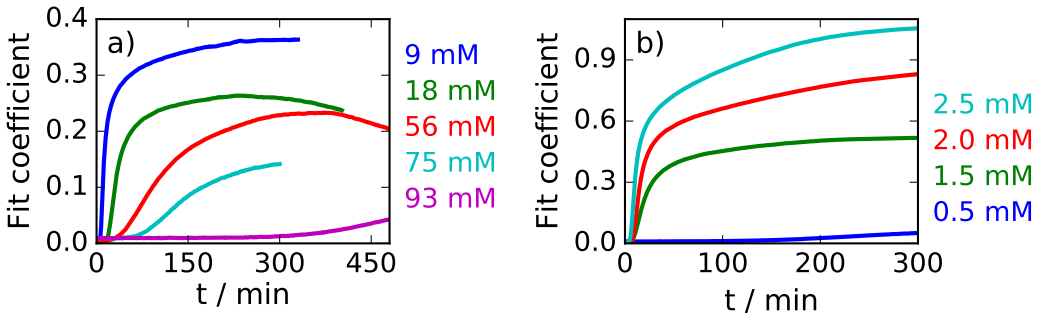

Figure 5.2 Fit coefficients for component 2, identified as CuBTC, over the time of the experiments at different concentration conditions. a) Fit coefficient vs time at different BTC concentrations as noted in the legend. The Cu^{2+} concentration was fixed at 1 mM. b) Fit coefficient vs time at different Cu^{2+} concentrations as noted in the legend. The BTC concentration was fixed at 38 mM.

describes the growth of CuBTC. It should also be noted that elastic light scattering of the growing CuBTC crystals will induce an apparent absorbance over the whole spectral range and increase the determined contribution of both components. This scattering effect is difficult to quantify. For the shape of the spectrum it means that throughout the whole spectral range the measured absorbance will be higher than the pure absorption. Towards the lower wavelengths the scattered intensity will generally increase, as elastic scattering scales with λ^{-4}. While the total determined concentration of CuBTC will be overestimated, due to the light scattering by the growing crystals, the relative kinetic information is not expected to change. Faster growing crystals will also show an earlier influence of the scattering contribution. Assuming the resulting crystal sizes are comparable between experiments (which we prove to be a reasonable assumption later in section 5.6.1), the scattering will not change the relative kinetic information we obtain from different experiments.

5.3 The inhibiting effect of BTC on CuBTC growth

To better understand the interplay of Cu^{2+} and BTC in the solution, we now want to observe how different concentrations of the two reactants change the behavior of the concentration transients of CuBTC that we observed in the previously discussed experiment. Figure 5.2

shows the fit coefficients of the CuBTC component for different BTC and Cu^{2+} concentrations over time. The spectra used for the NNLS fit are those shown in Figure 5.1 b).

Figure 5.2 a) contains growth traces at a fixed Cu^{2+} concentration (1 mM) but varying BTC concentrations. All traces generally show the same behavior. After an induction period the growth starts and increases before leveling off. As the BTC concentration increases the induction period increases as well. At 9 mM BTC, it is almost not measurable in the time frame of our experiment. At 18 mM the induction period is already $\approx$ 3 minutes long and it gradually increases to about 350 minutes in a solution containing 93 mM BTC. Secondly, the growth rate, after the induction period, also decreases as the BTC concentration in the solution increases which can be seen in the slope of the concentration transients. For the lowest BTC concentration (9 mM) the maximum slope is around $2{\cdot}10^{-2}$ min^{-1}, for the highest BTC concentration (93 mM) the maximum slope is around $2{\cdot}10^{-4}$ min^{-1}. We observe that, contrary to chemical intuition, BTC slows the formation of CuBTC by both increasing the induction period and by slowing down the growth rate. Some traces show a drop in the fit coefficient towards later times. This is due to a settling of the grown CuBTC crystals in the cuvette due to gravity, and thus out of the excitation beam which decreases the measured absorbance.

Figure 5.2 b) shows the effect of different Cu^{2+} concentrations on the growth process at a fixed BTC concentration of 38 mM. This medium BTC concentration slows down the growth sufficiently to let us measure the induction period in the time frame of our experiment. Again, the traces show the previously observed general behavior of induction, growth and saturation of the growth. This time, however, the induction periods get shorter as the Cu^{2+} concentration increases. Additionally, the maximum rate or the maximum slope of the traces, increases with the Cu^{2+} concentration. For the lowest Cu^{2+} concentration (0.5 mM) the maximum slope is around $3{\cdot}10^{-4}$ min^{-1} and for the highest Cu^{2+} concentration (2.5 mM) it is around $4{\cdot}10^{-2}$ min^{-1}. This matches the expected behavior of faster reactions at higher reactant concentration. The maximum value of the traces also increases with increasing Cu^{2+} concentration, indicating that consumption of Cu^{2+} is the limiting factor for the synthesis.

5.4 Developing a chemical reaction sequence

We want to develop a phenomenological chemical reaction model that is able to explain most of the observations pointed out in the experimental data. To explain the 'incubation' period, the increase in rate, the leveling off of the traces and the unexpected slow-down effect of BTC on the reaction, our model needs several distinct features that we will first discuss generally and then specify in detail to fit the CuBTC system.

First, the incubation period and increase in the speed of the reaction towards the middle of the growth can be explained with a nucleation-growth model, as has already been proposed for many crystal-growth mechanisms like for example by Lutsko et al. on the example of Zeolites. In essence, nucleation is usually hindered due to being thermodynamically 'uphill', while growth onto an already existing nucleus or crystal surface is energetically favorable and thus quicker. Existing crystal surface thus has a cooperative effect on further growth.[153] The actual growth can then be described by two different chemical reactions:

Assuming a system with metal ions M (we omit the charges) and linker molecules L that form a solid state material ML_y, nucleation takes place according to:

$$M + yL \xrightarrow{k_1} ML_y \tag{5.1}$$

While the elementary nucleation step/formation of a nucleus itself will be a reversible equilibrium reaction, we opted to define the species ML_y as the first thermodynamically stable species. The reversible formation and dissolution of a nucleus is therefore incorporated into the kinetic constant k_1.

The surface catalyzed growth reaction, where an existing ML_y-unit $[ML_y]$ (the square brackets indicate a surface site on the existing ML_y material) facilitates further growth by giving an anchor point to attach further ML_y units would follow:

$$M + yL + [ML_y] \xrightarrow{k_2} [ML_y] \cdots ML_y \tag{5.2}$$

The higher $[ML_y]$, thus the more crystal surface already available, the more reaction (5.2) will be favored over (5.1). These two equations are able to describe general crystal growth and nucleation on a pure concentration level and can model the general observation that

existing crystal surface catalyzes further crystal growth. The exact differences between growth and nucleation will depend on the system investigated and will manifest in differences in the kinetic rate constants k_1 and k_2. The proposed equations also explain the leveling-off effect we observe. As the amount of the metal-cation precursor M decreases, the reactions will naturally slow down and thus be limited by the overall amount of precursor available. While the same is true for the ligand L, in our experiments the concentration of the ligand was always sufficiently high as to not become the limiting factor.

The model additionally needs to explain the inhibiting behavior that the ligand has. To be able to inhibit the growth, the ligand must be part of a chemical reaction that leads to a formation of an inactive/slow-reacting species. Otherwise an increase in the linker concentration would, according to equations (5.2) and (5.1), always lead to an increase in the production rate of ML_y. A prerequisite for the formation of this inactive species is, that it must be favored over the formation of the desired product ML_y at high concentrations of L. This requirement can only be fulfilled if the stochiometric ratio of L to M is larger in the reaction that forms the inactive/slow-reacting species when compared to the formation of ML_y. Only then can an increase in the concentration of L lead to an overall decrease in the production rate of ML_y.

We therefore propose that the inhibition stems from a reaction that produces an overcoordinated species ML_x (with $x > y$) that is either slower to react to the final product ML_y or unable to react at all, but can react back to the pure precursor M. To complete our model we make both pathways accessible; a reversible reaction of M to ML_x as well as a slow reaction of ML_x to ML_y. We propose the following reactions:

The reversible formation of the slow-reacting overcoordinated species ML_x:

$$M + xL \underset{k_{3r}}{\overset{k_3}{\leftrightarrow}} ML_x \tag{5.3}$$

The attachment of the overcoordinated species to existing material, leading to crystal growth:

$$ML_x + [ML_y] \xrightarrow{k_4} [ML_y] \cdots ML_y + (x-y)L \tag{5.4}$$

With increasing L concentration, the velocity of reaction (5.3) will increase more strongly than that of equations (5.1) and (5.2) due to the higher L/M ratio in equation (5.3). More M

will be 'trapped' in the slow-reacting species ML_x, decreasing the overall production rate of ML_y.

5.4.1 Adaption of the model to the CuBTC system

We now adapt the general equations proposed so far to our system. The initial solvated Cu^{2+} species is discussed as Cu as to not make these phenomenological reaction equations confusing with respect to charge balances. As we know that the structure of CuBTC contains dinuclear Cu-paddlewheels as its fundamental building unit, the nucleation and growth reactions reflect this accordingly. Adapting equation (5.1) to our system then leads to:

$$2Cu + 4BTC \xrightarrow{k_1} Cu_2BTC_4 \tag{5.5}$$

While it is debatable if a single Cu-paddlewheel already serves as a nucleus, in the frame of our model this description suffices. Analogous to equation (5.2), for crystal growth catalyzed by existing CuBTC-MOF we then get:

$$[Cu_2BTC_4] + 2Cu + 3BTC \xrightarrow{k_2} [Cu_2BTC_4]\cdots Cu_2BTC_3 \tag{5.6}$$

Here [CuBTC] again denotes a surface site on an existing CuBTC crystal that serves as an anchor point for the next building unit. We assume that only three free BTC molecules are needed. The last BTC molecule needed to complete the paddlewheel could be a molecule that is part of an already existing CuBTC crystal and is used as an anchor for the new paddlewheel unit. The attachment of a complete dinuclear paddlewheel unit (Cu_2BTC_3) is consistent with the in-situ AFM studies of John et al. who observe that CuBTC grows in a step wise fashion. The height of one step on a growing CuBTC crystal matches the height of a single paddle-wheel unit.[73]

To investigate the possible structure and coordination number x of the overcoordinated species $CuBTC_x$ that we assume to be present based on our general model (equation (5.3)), we measured the UV/VIS spectra of solutions with different BTC concentrations at a fixed Cu concentration of 1 mM immediately after mixing the solutions as shown in Figure 5.3 a).

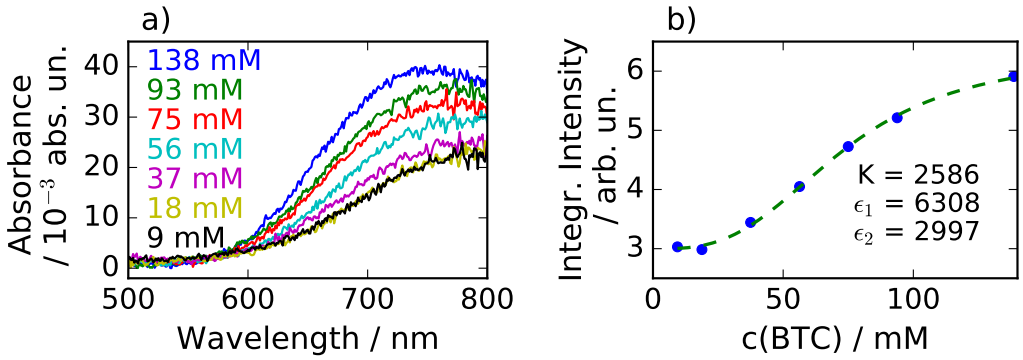

Figure 5.3 a) UV/VIS spectra taken of growth solutions at different BTC concentrations immediately after mixing the components. b) Integrated intensity of the UV/VIS spectra in a) in the range from 500 to 800 nm vs the concentration of BTC in the solution. The green line shows a fit of the data to equation (5.7). The inset text shows the resulting parameters for K, ε_1 and ε_2.

Every spectrum was measured from a freshly prepared solution within 20 seconds of mixing the solution.

While the low BTC concentration solutions (9 mM and 18 mM) show a spectrum very similar to pure $Cu(NO_3)_2$ x $2.5H_2O$ in ethanol, with its peak around 800 nm, the higher BTC concentrations show a gradual increase in the total absorbance intensity. In addition there is a slight gradually increasing blue shift of the absorbance peak with higher BTC concentrations. The spectral maximum shifts from 800 nm at 9 mM BTC to 740 nm at 138 mM. From the previous results (Figure 5.2) we know, that the blue shift cannot be due to an immediate formation of CuBTC, as the CuBTC growth is significantly slowed down at high BTC concentrations. E.g. for a concentration of 96 mM BTC we know that measurable CuBTC growth only starts after 5 hours. The blue shift therefore indicates a third spectroscopically identifiable component. The peak of this new species at 740 nm lies almost exactly between the spectra of our components 1 and 2. We cannot include the component in our kinetic fit of the data because its spectrum can also mathematically be described as a linear combination of components 1 and 2. We can, however, infer other information from those spectra. Assuming a reaction as described in equation (5.3), given concentrations of L (BTC) and M (Cu) lead to a defined equilibrium situation (before the actual growth of CuBTC starts to have a significant effect on the concentrations in the solution). According to the mathematical derivation in Appendix B (section B.4) we expect the integrated UV/VIS

absorbance over the investigated spectral range to follow the formula (5.7):

$$I_{tot} = \frac{c_0\,(\mathrm{Cu})}{1 + K c_0\,(BTC)^x} \cdot (\varepsilon_1 + \varepsilon_2 \cdot K \cdot c_0\,(BTC)^x) \tag{5.7}$$

with $c_0\,(\mathrm{Cu})$ the starting concentration of Cu-ions in solution, $c_0\,(BTC)$ the concentration of BTC in the solution, K the equilibrium constant for reaction (5.3), x the coordination number and ε_1 and ε_2 the integrated absorbance coefficients for the two components over the whole spectrum. Figure 5.3 b) shows the integrated total intensities of the measurements from a). The green line in Figure 5.3 b) shows the fit of the experimental data to equation (5.7) assuming a coordination number of x=3. The equation also fits the data reasonably well with a coordination number of 2 (shown in B.4). Assuming one BTC molecule occupying two coordination sites around the copper center via one carboxyl moiety, both coordination numbers would lead to commonly observed structures of Cu^{II} complexes, 2 being a quadratic planar configuration and 3 giving an octahedral complex that is expected to be Jahn-Teller distorted.[154] A dinuclear copper complex with 6 acetate ligands, that shows a structure similar to the CuBTC-paddlewheel, has been observed before and would fit the 1/3 ratio of Cu^{2+} to BTC as well.[155]

That we can describe the measured spectra and their integrated intensities with the above discussed equation (5.7) very well shows, that the equilibrium reaction (5.3) most likely takes place in our system with a coordination number of 3 ligands to 1 metal. We therefore propose, according to the generally discussed reactions (5.3) and (5.4), the following reactions for our model:

$$\mathrm{Cu} + 3\mathrm{BTC} \underset{\mathrm{k_{3r}}}{\overset{\mathrm{k_3}}{\longleftrightarrow}} \mathrm{CuBTC_3} \tag{5.8}$$

$$2\mathrm{CuBTC_3} + [\mathrm{CuBTC}] \xrightarrow{\mathrm{k_4}} [\mathrm{CuBTC}] \cdots \mathrm{Cu_2BTC_4} + 2\mathrm{BTC} \tag{5.9}$$

5.5 Numerical validation of the chemical reaction model

We numerically evaluate the concentration profiles that our proposed set of reaction equations ((5.5), (5.6), (5.8) and (5.9)) would yield under specific experimental conditions. For details on the setup of those numerical simulations we refer to Appendix B. We have to guess the

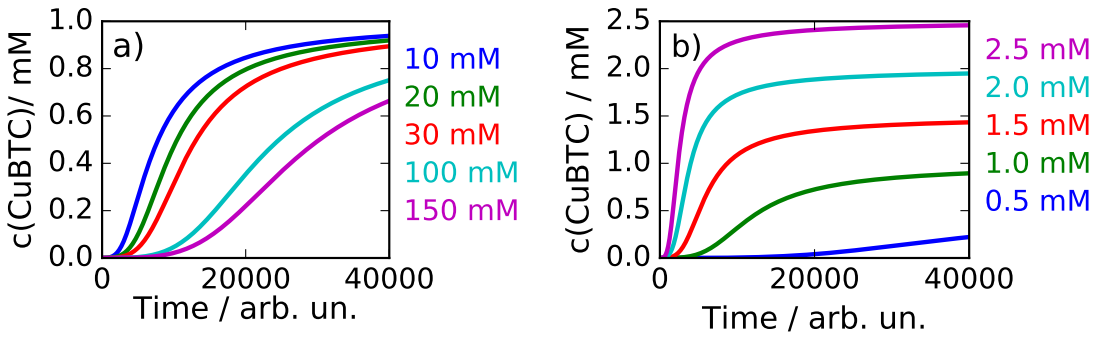

Figure 5.4 Results of the numerical evaluation of the reaction model. a) CuBTC concentration in the solution over time at different BTC concentrations. The starting Cu_2^+ concentration was fixed at 1 mM. b) CuBTC concentration in the solution over time at different starting Cu^{2+} concentrations. The BTC concentration was fixed at 30 mM.

kinetic rate constants ($k_1, k_2, k_3, k_{3r}, k_4$) thus our model is not easily fit quantitatively to the experimental data.

Figure 5.4 shows the results for the concentration traces of CuBTC in our numerical model at fixed rate constants (as detailed in the Appendix).

Figure 5.4 a) shows the concentration of CuBTC over our arbitrary timescale at different BTC concentrations (and a fixed Cu^{2+} concentration of 1 mM). We see that at the beginning of the simulation for all traces the concentration of CuBTC in the solution is close to 0. After an induction period, the length of which increases as the concentration of BTC increases, significant growth of CuBTC starts. For the 10 mM BTC solution, this induction period lasts around 2000 time units while for the highest simulated concentration (150 mM) it lasts around 15000 time units. The maximum speed (the maximum slope of the traces) decreases with higher BTC concentrations. At the lowest BTC concentration (10 mM) the maximum slope is $1{\cdot}10^{-7}$ arb.un. while it is $3{\cdot}10^{-8}$ for the highest concentration (150 mM). Towards the end the changes in CuBTC concentration level off and approach a similar maximum limit for all simulations.

Figure 5.4 shows the traces at different copper concentrations but a constant concentration of BTC (30 mM). We see the same qualitative features as with the different BTC concentrations. In this case, however, the induction periods get shorter at higher copper concentrations. In

addition, the maximum rate of the traces also increases with the Cu^{2+} concentration ($1 \cdot 10^{-8}$ at 0.5 mM and $8 \cdot 10^{-7}$ at 2.5 mM).

The simulated traces qualitatively match the behavior of the measured data very well. The model is able to reproduce all important features such as the induction period of the growth, the leveling off due to a decrease in active Cu^{2+} species towards the end, the increase in overall speed at higher Cu^{2+} concentrations and the slow-down effect of BTC on the overall growth process.

As our model is able to describe all important experimental observations, we think to have unraveled the chemical reaction sequence taking place during the production of CuBTC. Without doubt, the proposed reactions will have sub-reactions where ligands are exchanged one after the other, and transient intermediates form. For example it is known from in-situ atomic force microscopy[73] and quartz crystal microbalance[151] measurements that CuBTC generally grows layer-by-layer, meaning that complete paddle-wheel structures attach to already existing MOF. Therefore reactions (5.6) and (5.9) will, in reality, probably go through a pre-formed intermittent paddle-wheel state. Our aim here was to minimize the amount of chemical equations to the absolutely necessary ones to describe the experimental results. We thus propose for the first time a slow-reacting $CuBTC_3$ leading to a significant decrease in the speed of the formation of the MOF CuBTC at high concentrations of BTC. In section B.1.3 we show the effect on the growth rate of CuBTC, when the inhibiting reaction (5.8) is 'turned off'. We observe that when the rate for the production of the inhibiting species $CuBTC_3$ is 0, the growth rate of CuBTC increases with increasing BTC concentration.

5.6 The effect of BTC concentration on crystal morphology

Based on our model it seems beneficiary to perform MOF synthesis at low BTC concentrations if fast reaction throughput is desired. To clarify, whether the reduced amount of BTC has an adverse effect on the morphology of the synthesized CuBTC we now want to compare CuBTC samples synthesized at different BTC and copper concentrations. In addition, we

Table 5.1 Synthesis conditions for room temperature solution-based syntheses

Sample	c(Cu^{2+})	c(BTC)	mean crystal edge length	standard deviation of the size distribution
1	2.5 mM	37 mM	180 nm	70 nm
2	1.0 mM	9 mM	180 nm	70 nm
3	1.0 mM	37 mM	200 nm	80 nm
4	1.0 mM	55 mM	220 nm	90 nm
5	0.5 mM	37 mM	220 nm	90 nm

investigate the effect different BTC concentrations have on the outcome of electrochemical CuBTC synthesis.

5.6.1 Room-temperature solution based synthesis

We start with comparing CuBTC samples synthesized from homogeneous solution under concentration conditions that match some of our UV/VIS experiments. The reaction volume was increased to 10 mL to provide enough material for characterization. We performed 5 different syntheses the conditions of which are shown in Table 5.1. The conditions were chosen in such a way that a medium concentration for both reagents (Sample 3) can be compared to syntheses done at higher/lower Cu^{2+} concentration (Samples 1, 5) or higher/lower BTC concentrations (Sample 4, 2) respectively. The reactions were performed for 16 hours at room temperature and the material isolated using centrifugation. Afterwards, the blue powders that were isolated were investigated using SEM. Raman spectra confirmed the successful synthesis of CuBTC in all cases (not shown).

Figure 5.5 shows representative SEM images of the different synthesis products. All samples are dominated by large agglomorates (larger than the shown image sizes) of octahedral crystals in the size range of 100 nm to 1 µm. At first glance, the crystals in all images are of roughly the same size and size dispersion, showing that there does not seem to be a strong correlation between the concentrations of the reagents and the crystal morphology. It should be noted, that Sample 1 with the highest copper concentration in solution did visually produce more material than the other syntheses, in line with our previous conclusion that copper is the yield-limiting reagent.

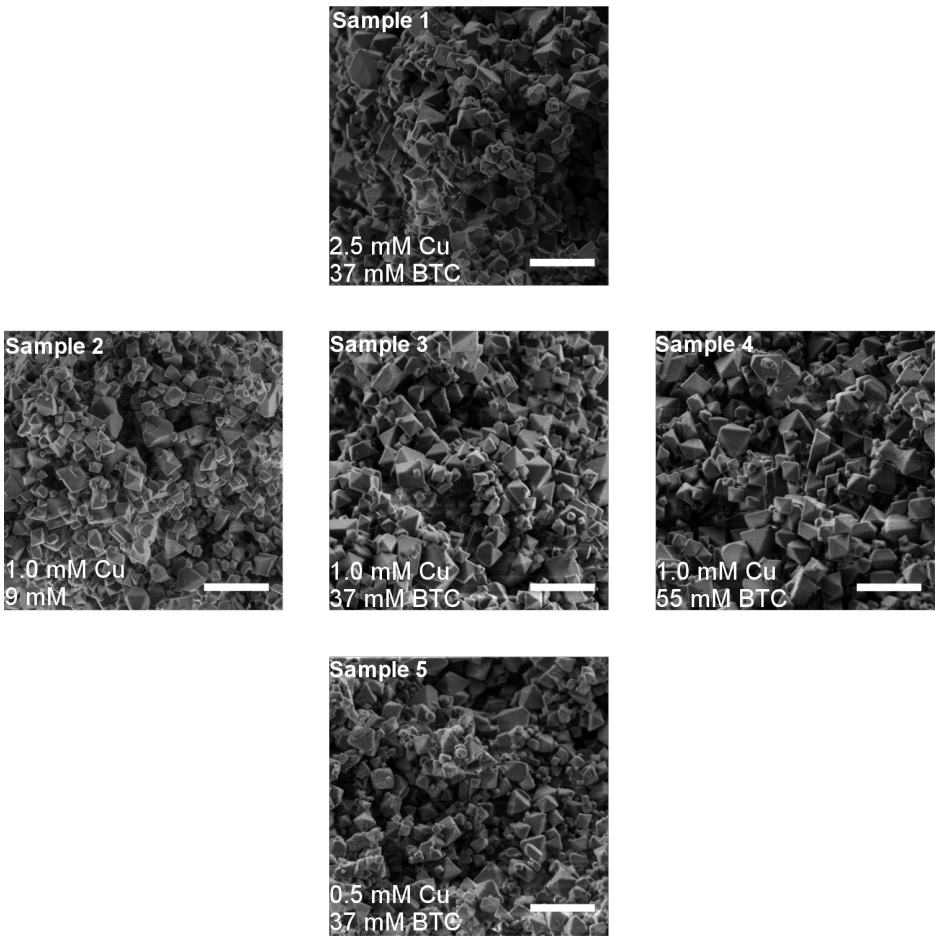

Figure 5.5 Representative SEM images of the samples synthesized for 16 hours at room temperature according to the synthesis conditions in Table 5.1. Scale bars are 1 µm.

We measured edge lengths of crystals on 2-3 SEM images per sample. The measuring was done manually using Image J. We estimate the human error of this manual measuring to be around 15 %. The right side of Table 5.1 shows the mean edge lengths of the counted crystals (at least 200 crystals per sample) as well as the standard deviation of the size distribution. All mean crystal edge lengths range around 200 nm with standard deviations around 80 nm. As the copper concentration increases the crystal size seems to drop from around 220 nm at 0.5 mM Cu^{2+} to 180 nm at 2.5 mM. For BTC the trend is opposite with 180 nm mean edge length at 9 mM BTC and 220 nm at 55 mM. The changes in the crystal sizes are miniscule, especially comparing it to the large standard deviations. Our method of determining the sizes is inherently flawed due to human error and low sample size. We would need to count a vastly larger amount of particles to narrow down statistical variances and possibly find a

correlation between concentration and crystal size. Due to the non-trivial contrast in SEM, however, automation of the crystal counting proved to be difficult and as such we cannot easily increase the sampling size. We therefore conclude that there is no statistically relevant correlation between reagent concentration and crystal morphology under our evaluation conditions. Since the BTC concentration does not have an effect on the crystal size, it is therefore overall beneficial to decrease the concentration of BTC for solvothermal synthesis of CuBTC as the concentration decrease will lead to faster production of CuBTC.

5.6.2 Electrochemical synthesis

We also want to investigate the effect of the BTC concentration on the sample morphology in the electrochemical synthesis. We performed electrochemical synthesis as described earlier with deoxidized copper plates as anodes in electrolytes containing 7 different BTC concentrations between 3 and 43 mM. Otherwise the synthesis conditions were the same as in the standard protocol, with 0.032 M MTBS in the solution, using non-degassed 98% ethanol (with 2% added water) as the solvent. The synthesis potential was 0.2 V and the synthesis was performed for 150 seconds. The synthesis potential was chosen low to mimic the conditions of our UV/VIS experiments. At low synthesis potential, the current density for copper dissolution will be low and will therefore keep the amount of available Cu^{2+} low. The copper anodes were investigated using SEM after the synthesis.

Figure 5.6 shows example SEM images at three different BTC concentrations. The SEM images represent the lowest (3 mM), an intermediate (20 mM) as well as the highest (43 mM) BTC concentration used. For all samples we observe octahedral crystals of CuBTC in the size range of 50-200 nm. As the BTC concentration increases, the crystal size decreases. In addition, the higher BTC concentrations show larger gaps between crystals leading to a significantly reduced surface coverage with CuBTC.

Figure 5.7 shows the mean crystal edge lengths as obtained from manually measuring the crystals with ImageJ. Again at least 200 crystals were measured for every sample, spread out over 2-3 different SEM images. We see that under the chosen electrochemical conditions (low synthesis potential and short electrolysis times) the crystals are generally small (< 200 nm). For the lowest BTC concentration the crystals average around 130 nm edge length with

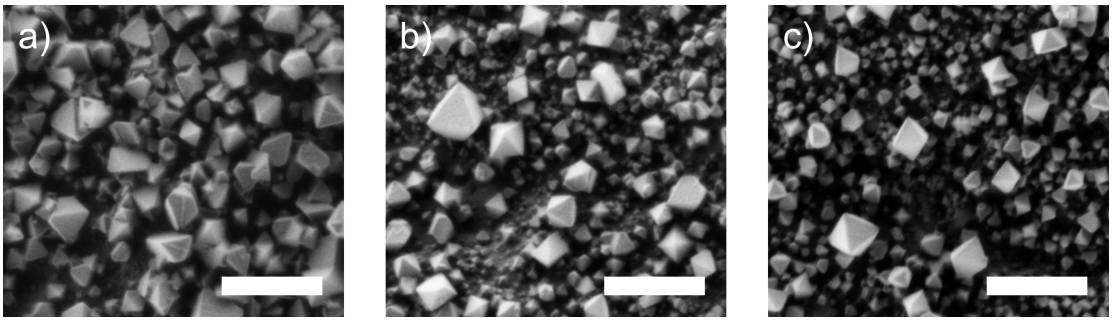

Figure 5.6 Representative SEM images of samples electrochemically synthesized at 0.2 V for 150 seconds in solutions containing: a) 3 mM BTC, b) 20 mM BTC, c) 43 mM BTC. Scale bars are 500 nm.

a standard deviation of around 45 nm. As the BTC concentration increases, the mean crystal sizes decrease (as does the standard deviation). At 25 mM BTC the crystal size dropped to 63 nm. Here a plateau builds and higher BTC concentrations up to 44 mM do not seem to noticeably decrease the crystal sizes further.

Together with our observation from the SEM images that higher BTC concentrations lead to a decrease in overall surface coverage of CuBTC on the copper electrode surface it seems that less of the Cu^{2+} that is produced electrochemically (after the cuprite intermediate) is actually converted to surface-bound CuBTC. The reason for the reduced coverage of the surface with CuBTC can be found in our model of the nucleation and growth. Following this reasoning, at higher BTC concentrations, more Cu^{2+} is immediately bound in the slow-reacting $CuBTC_3$ state according to equation (5.8). The slow reacting species can then diffuse away before it can react to CuBTC and be unavailable for surface-growth of CuBTC. The results from the electrochemical synthesis therefore support our model of an inhibiting/slow-reacting overcoordinated $CuBTC_3$ species that preferentially forms at high BTC concentrations and therefore decreases the amount of CuBTC that is formed on the surface.

5.7 Conclusion & Outlook

We were able to follow the progress of room-temperature CuBTC solution growth through UV/VIS spectroscopy. With a NNLS fitting procedure we could separate the signal of CuBTC from the signal of the precursor, obtaining kinetic information about the growth process.

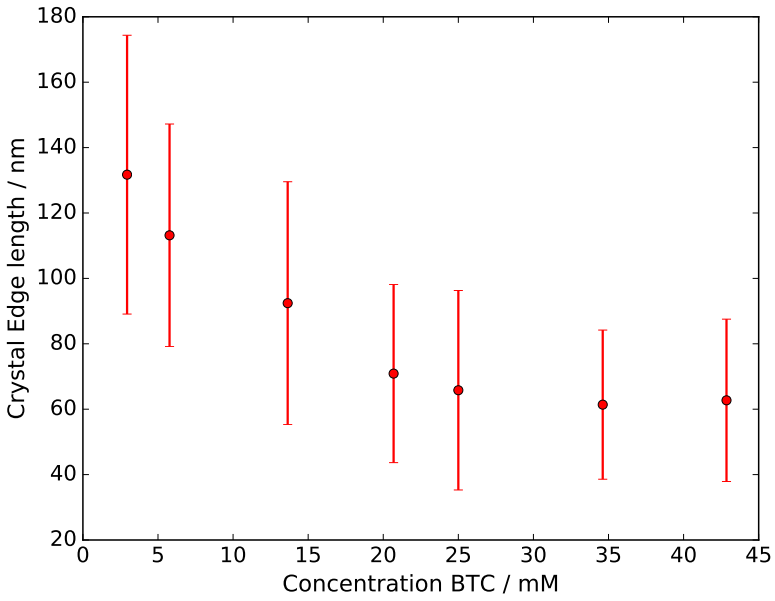

Figure 5.7 Mean measured crystal edge lengths for the electrochemical synthesis at different BTC concentrations. The error bars are standard deviations of the crystal size distributions.

Using different concentrations of reactants we observed that while an increase in the Cu^{2+} concentration as expected leads to an increase in the reaction speed, BTC actually hinders the reaction, slowing down the growth. We could disentangle a third Cu^{2+} species that is overcoordinated in BTC and very slow in reacting to CuBTC. Based on our observations we developed a chemical reaction sequence to describe the nucleation and growth, including the passivating effect of BTC. The model was numerically evaluated and compared to the measured data, finding a strong qualitative correlation.

Room-temperature solution-based synthesis of CuBTC did not show a strong correlation between the Cu^{2+} or BTC concentrations and the morphology of the synthesized crystals. In the electrochemical synthesis, however, we could observe a significant decrease of the CuBTC surface coverage and the CuBTC crystal size on the copper electrode at higher BTC concentrations. The overall reduced amount of CuBTC produced on the surface can be explained using the inhibiting species proposed in our model. At high BTC concentrations more of the electrochemically produced Cu^{2+} is immediately bound in the $CuBTC_3$ species. Its slow reaction rate allows for diffusion away from the electrode surface before it reacts to CuBTC, making it unavailable for surface-growth of CuBTC. Our model also offers an

explanation for the very fast electrochemical growth at high potentials, when compared to the classical solvothermal synthesis. As the Cu^{2+} is produced immediately in front of the electrode, the BTC/Cu ratio is locally so low, that the inhibiting $CuBTC_3$ species does not form to a large degree. Most of the Cu^{2+} can instead immediately react to CuBTC. The electrochemical synthesis thus directly overcomes the inhibiting effect that large amounts of BTC have on the kinetics of the reaction.

Summarizing, our study has shown that using lower concentrations of BTC leads to faster reactions in the room-temperature solution synthesis with minimal effect on the final crystal morphology. For the electrochemical synthesis a lower BTC concentration even increases surface coverage of CuBTC on the copper electrode. It would therefore not only be economically preferable to use low linker concentrations (due to lower amounts of waste) but it also can significantly decrease reaction times and produce better MOF thin film devices.

As we are limited in our experiment by not only the time resolution of our UV/VIS experiment but also by the maximum absorbance of the sample, our experiments had to be conducted at very low copper concentrations. While we don't expect the chemical reaction mechanism to change, it is hard to predict if the inhibiting effect of BTC is equally strong at high Cu^{2+} concentrations ($\approx$ 100 mM). It could be worth to verify our model at high Cu^{2+} concentrations to approach industrial scale processes. Additionally other MOFs with BTC as a linker and a similar coordination chemistry could show the same underlying chemical reaction sequence. A generalization of our model could help the design of industrial scale production of a large variety of different MOF materials.

Chapter 6

Summary and future directions

Metal-organic frameworks are crystalline hybrid materials that have a large variety of applications in i.e. catalysis, gas sieving and molecular sensing. Their modular structure, built from metal cations and multifunctional organic linkers, makes them in principle ready to be engineered for a specific purpose. The electrochemical synthesis using a metal anode as the metal source is a fast, energy efficient and possibly very versatile approach to MOF production. Wide-spread use of the electrochemical synthesis for the fabrication of MOF materials for industrial applications is hindered by a lack of deep understanding about the physicochemical processes during the crystal growth. In this thesis the redoxchemical and molecular mechanisms behind oxidative Cu-MOF growth have been studied with the aim of providing new tools to the synthetic chemist's toolbox.

Oxidation mechanism of Cu In order to unravel the mechanism of the oxidation of elemental copper to Cu^{2+} a combinatorial chemical approach was used. By systematically excluding specific reagents such as water, copper oxides and oxygen from the synthesis solution we were able to unravel a two-step oxidation mechanism with cuprite (Cu_2O) as a necessary oxidation intermediate. We developed an easy approach to produce patterned CuBTC devices by prepatterning a surface with copper oxide and performing the electrochemical synthesis under the exclusion of oxygen and water. Since neither water nor oxygen are available to produce cuprite in-situ, CuBTC only grows at spots on the sample that are already covered with Cu_2O.

Potential-dependent surface adsorption of BTC on Cu CuBTC is one of the few MOFs that electrochemically grow on the surface of the electrode used as the metal ion source. As surface-bound MOF coatings are interesting for membrane applications it is important to understand what makes CuBTC special in that regard. Using electrochemical surface-enhanced Raman spectroscopy and cyclic voltammetry, we investigated the potential dependent interaction between the BTC linker molecule and a copper surface at potentials below the MOF formation potential. We found that the closer the electrochemical potential is set to the synthesis potential of the MOF, the more BTC adsorbs onto the surface. After the potential threshold for MOF growth was crossed, we could spectroscopically follow the transformation of the BTC adlayer to surface-bound CuBTC. We propose that the strong interaction of BTC with the electrode prior to the actual growth of CuBTC leads to the BTC being the connecting layer between Cu and CuBTC that ultimately leads to surface attachment of the crystals. Future endeavors to produce surface-bound MOFs should therefore start with other cation-organic linker pairs that are known for strong specific interactions between the molecule and the surface of the metal.

Kinetics and complex chemistry of CuBTC growth Short synthesis times are especially important for industrial production and application of materials. In addition, it is important to know the chemical reactions during a given material synthesis as to be able to calculate energy balances and optimize synthesis routes with respect to optimal educt ratios. In order to facilitate proper planning of large-scale CuBTC productions and also unravel the origin of fast electrochemical growth we investigated the kinetics of homogeneously nucleated CuBTC. We found that, contrary to chemical intuition, an increase in the concentration of linker present in the synthesis solution leads to a decrease in the overall speed of CuBTC production. We developed a chemical reaction model that describes crystal nucleation and surface-catalyzed growth as well as the reversible formation of a slow-reacting, overcoordinated $CuBTC_3$ species. A numerical evaluation of the model shows, that it can accurately describe the experimental results. Our results therefore not only help develop faster synthesis protocols (by decreasing the amount of BTC in the solution) but also give insight into the usually hard to assess complex chemistry during the formation of CuBTC.

A series of electrochemical CuBTC syntheses at different BTC concentrations reveals that high linker concentrations lead to a decrease in the overall crystal size and coverage of the surface, which we can explain on the basis of our model. We conclude that for large-throughput syntheses of CuBTC, the linker concentration should be balanced to match the desired requirements to the synthesis in terms of overall speed and yield. Additionally lower BTC concentrations can actually be beneficial in the electrochemical production of high-coverage MOF membranes. Our model can also yield an explanation for the accelerated electrochemical growth compared to the classical solution-based method, as the locally very high concentration of Cu^{2+} ions in front of the electrode lessens the inhibiting effect of large BTC concentrations.

Summarizing we find that the sequence for the electrochemical production of CuBTC is as follows:

At potentials more anodic than 0 V versus Cu in presence of water or oxygen Cu is oxidized to cuprite in a first step. A second oxidation step, which uses the protons that dissociate from the linker molecule to oxidize the cuprite further to Cu^{2+} follows as we know from the work of Campagnol et al.[79] The BTC molecules have, at these high potentials, a large propensity to adsorb to the copper surface. As such, a layer of BTC forms on the copper electrode that can serve as an anchor point for the copper ions liberated from the electrode. The attached copper ions then serve in turn as the nucleus for CuBTC growth which happens through the attachment of complete paddlewheel units to the existing framework. High concentrations of Cu^{2+} in front of the electrode lead to a suppression of the formation of the slow-reaction $CuBTC_3$ species and thus the electrochemical growth proceeds very fast.

Some questions still remain. It is unclear, whether BTC also has a high propensity to adsorb onto the intermediate cuprite layer. Our observation that CuBTC also grows on cuprite particles would support this. However, we cannot specroscopically verify this based on our results. If BTC does not also adsorb to cuprite, it is unclear if oxidation of Cu and nucleation of CuBTC happen at the same area of the copper electrode, or if they might be spatially separated. It is hard to imagine a surface that is constantly being dissolved forming a stable basis for the attachment of the BTC linkers (and subsequent nucleation of CuBTC). A spatial

separation between the two processes, however large, could explain our observations. As we do not know at which length scales this separation would take place, in-situ spectroscopic techniques with high spatial resolution should be employed. We recommend, for example, the use of electrochemical Tip-Enhanced-Raman scattering (EC-TERS) which yields chemical information with spatial resolutions in the range of 10 nm.[145,146] Finding possibly different domains during the growth could give more information about the exact structure of the electrochemical interface during the synthesis and help us fine tune the parameters for the production of CuBTC with desired mesoscopic properties.

The insight gained in this thesis can lead the way to new and better MOF synthesis protocols. Our r can also serve as the starting point for further mechanistic studies on MOF growth. In a first step other MOFs should be investigated with our results in mind to see if CuBTC can help define the general characteristics of electrochemical MOF synthesis. To start, other copper-based MOFs with different linker molecules should be synthesized electrochemically and investigated as to whether cuprite is a universally necessary intermediate for the oxidation of Cu to Cu^{2+}. To check whether BTC is the defining factor for the surface adhesion of CuBTC and the peculiar kinetic behavior we observed, other MOFs based on BTC as a linker should be investigated in a similar way. Generalizing the mechanistic peculiarities of CuBTC will help in developing a universal model of MOF growth which will ultimately be necessary if we aim to be able to rationally plan the synthesis of any MOF material in the future.

Appendix A

Crystal growth of oxidatively synthesized CuBTC

In chapter 4 we have shown that CuBTC most likely nucleates on the BTC layer that forms on Cu surfaces under electrochemical conditions. We still need to answer the question as to how the growth proceeds afterwards.

For the conventional, solvothermal synthesis of CuBTC starting from dissolved Cu^{2+} as the copper precursor, Anderson et al. were able to investigate the growth using in-situ AFM.[72,73] They found that the steps that appear on the (111)-facet of a growing CuBTC crystal show well defined heights across the whole crystal. The heights of these steps match the distances of sublayers of the (111)-cut through the unit cell. In CuBTC's crystal structure the height of a single (111) step is 1.52 nm. A (222) step would therefore be 0.76 nm high. John et al. found these distances in their AFM measurements, showing that complete building blocks of Cu and BTC together attach to the existing crystals at once and not procedurally.[73]

As we have shown before, the electrochemical growth of CuBTC shows some peculiarities in its overall growth mechanism which call into question if the results of John et al. can be immediately transferred to the ec synthesis. We set out to reproduce John's measurements using in-situ AFM during the electrochemical growth. Due to experimental issues, we were not able to monitor the growth under electrochemical conditions. We could, however, monitor the growth starting from a copper substrate that is aerobically oxidized to CuBTC similar

to the previously discussed electroless oxidative synthesis (see chapter 3). As we assume that the aerobic oxidative mechanism is essentially the same as the electrochemical anodic mechanism we can transfer our insight to the electrochemical case.

A.1 Experimental details

We first investigated a sample that was grown electrochemically under standard conditions at 0.2 V for 80 minutes using AFM in air. The surface was searched for a single crystal with a facet almost perfectly parallel to the sample plane. This was done to reduce possible issues with distortions due to the scanned plane being at an angle with respect to the scanning direction of the AFM.

For the in-situ measurement we used 500 nm of evaporated copper on a glass slide as a substrate. The substrate was first imaged in air to establish the measuring parameters. Afterward ethanol was added to the liquid cell and the system was equilibriated for 30 minutes. The ethanol was removed through a syringe and a solution of 0.15 M BTC in 6% H_2O/94% ethanol was added. We started imaging the substrate surface at different positions until we could see CuBTC crystals growing through aerobic oxidation of the Cu substrate.

A.2 Stepwise oxidative growth of CuBTC

Figure A.1 shows an AFM image of a CuBTC crystal with a facet almost parallel to the sample plane (and thus the scan direction of the AFM). Due to the low synthesis potential of 0.2 V and the long synthesis time of 80 minutes the crystal has grown to be larger than 2 µm. The image was plane corrected so that the facet is parallel to the viewing plane. The facet is not flat but rather shows structures on its surface. We can observe elevated particle like areas on the surface in the size range of 20-100 nm. In addition two larger elevations in the size range of 500 nm are seen. These elevations are most likely CuBTC crystals that nucleated on top of the existing crystal and started growing there, similar to what Shoaee et al. saw in their in-situ AFM studies.[72] This is evident through the triangular shape of especially the bottom right large elevation as this is most likely a CuBTC(111) facet.

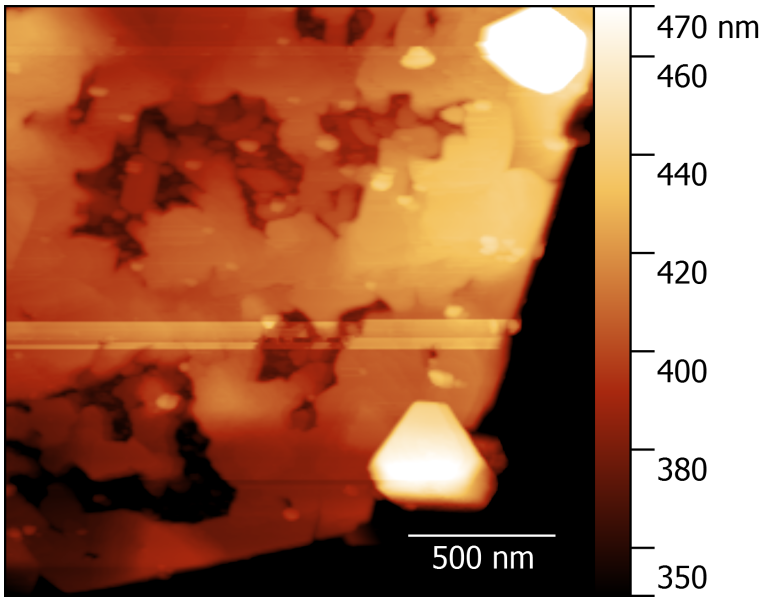

Figure A.1 AFM image of the topfacing facet of an electrochemically grown CuBTC crystal. The image was plane flattened so that the crystal facet is parallel to the image plane.

In addition a few pits can be seen on the crystal surface with no distinguishable preferred shape. These are most likely crystal 'defects' that still need to grow into a uniform layer of CuBTC. On the very top of the crystal a few step-like structures can be observed. To investigate these structures further the scan area was reduced to increase lateral resolution.

Figure A.2, left shows a zoom onto the top part of the crystal seen in Figure A.1. The previously only barely perceivable steps on the crystal surface are now more visible. It is obvious that the steps follow specific directions and generally show a three-fold symmetry as is to be expected from the (111) facet of a cubic crystal structure. The line profiles shown on right of Figure A.2 were taken at the indicated positions in the AFM image. The profiles show distinct steps preceded and followed by rather flat areas on the surface. We calculated the height of the steps by taking the difference of the median height of around 15 nm after and before the step itself. The calculated values are shown in the figure as an annotation to the corresponding step. As mentioned previously the image had to be plane corrected and especially line 3 still shows that the correction is not perfect. Thus the step heights will have a significant error that we estimate to be at least 20 %.

The step heights measured in lines 1 and 2 range around 1.8 ± 0.4 nm and the steps in line 3 are around 0.9 ± 0.2 nm. Within the errors the step heights match the steps that John and

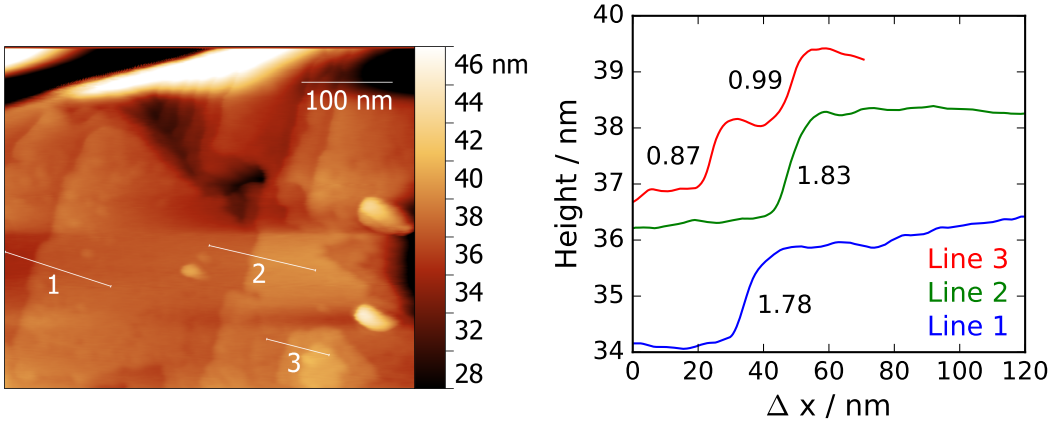

Figure A.2 left: Zoom of the facet shown in Figure A.1. The image is plane-corrected, so that the facet itself is in the scanning plane. right: height profiles taken along the lines drawn on the image on the left.

Shoaee[73,156] found in their in-situ AFM studies on the room temperature solution based synthesis, and therefore also match the (111) and (222) step heights of 1.52 nm and 0.76 nm respectively that are to be expected for CuBTC. Our ex-situ investigation therefore suggests that the electrochemical growth of CuBTC might follow the same building-block addition mechanism that has been proposed in literature.

A.3 In-situ investigation of the CuBTC growth mechanism

To check whether the observed steps really originate from an attachment of building blocks to the outer facets of an existing crystal we performed in-situ AFM. As mentioned previously we unfortunately, due to unforeseen interactions between the cantilever and the electrochemical processes on the substrate, were unable to investigate the actual electrochemical synthesis. However, as we have shown in Chapter 3 the applied electrochemical potential can be substituted by using dissolved oxygen in the synthesis solution which can oxidize the copper substrate and produce the necessary Cu^{2+} ions. A non-degassed electrolyte already provides sufficient oxygen for the synthesis.

Figure A.3 shows on the left side a non-corrected image of the Cu substrate surface after being immersed in the BTC containing synthesis solution for around 90 minutes. We see the edges of several large elevations, up to 2 µm in diameter and over 1 µm high. The one

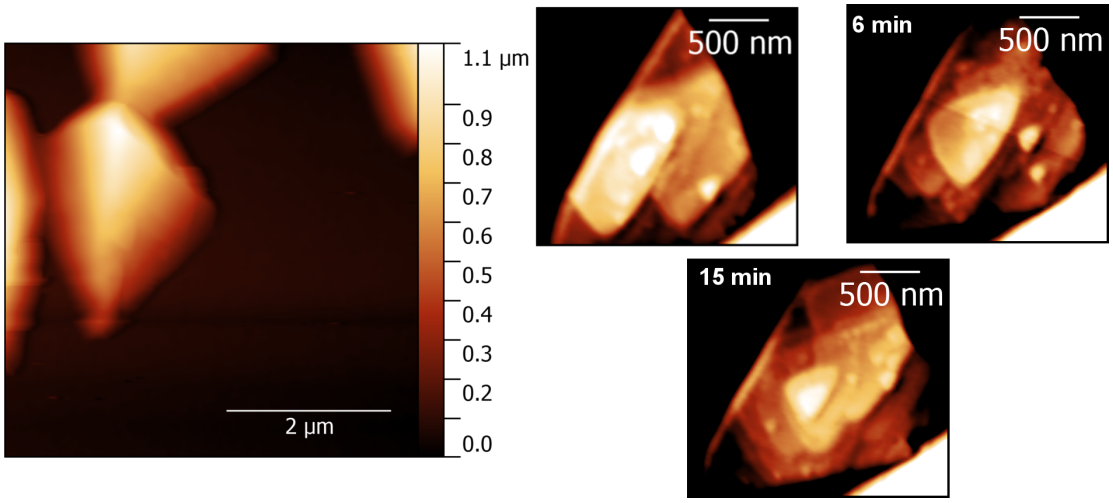

Figure A.3 left: Uncorrected AFM image of a copper surface immersed into oxygen-containing BTC solution in ethanol for 90 minutes. right: Series of images of the same crystal facet at different times. The times are denoted relative to the first image in the series. All images were plane corrected to bring the crystal facet into the imaging plane.

complete entity we see has a pyramidal shape indicating that this is most likely a CuBTC crystal. Already we can see hints of triangular shaped steps, particularly at the bottom of the facet that point towards the edges of the crystal facet. The right side of Figure A.3 shows a zoom onto this facet. The images were now plane corrected to bring the facet itself into the image plane. The three images show the same crystal facet at different times. We can see that the facet changes its local structure significantly over time. The general shape of the substructures is always triangular and the triangles are rotated by 45° compared to the facet itself.

While we cannot reasonably measure the height of the steps, since the initial inclination of the facet was too high to allow for precise measuring, we can still together with our results from Figure A.2 argue that the steps we see are the same kind of growth steps that are reported in literature. The fact that the facet's microstructure is changing over time suggests that building units are still being attached to the facet during the course of our in-situ imaging procedure. We therefore conclude that the mechanism of oxidative CuBTC growth onto existing crystals is the same as for the room-temperature solution based synthesis with preassembled Cu^{2+}-BTC building units attaching to the the existing facet to continue the crystal structure similar to what has been proposed by Campagnol et al.[79]

Appendix B

Supporting Information for Chapter 5

B.1 Details on the kinetic model and the numerical simulation

B.1.1 Kinetic rate equations

The change of all components in the reaction sequence detailed in chapter 5 was tracked through the numerical evaluation of the rate equations. Variables in square brackets are concentrations. [Area] is a measure of the exposed area of the already existing CuBTC crystals, for the derivation see section B.1.2. [N_c] is the number of crystals that nucleate and is tracked separatly from (but also added to) the overall concentration of CuBTC to allow for the determination of the average exposed area of the crystals. [MOF], the concentration of CuBTC, should be understood as a total concentration of copper ions bound in a paddle wheel structure, as such all reactions producing the MOF produce twice the amount, since they originate from two copper ions each. This keeps the overall concentration of copper-containing species in solution constant throughout the simulation.

$$\frac{d[\mathrm{Cu}]}{dt} = -2k_1[\mathrm{Cu}]^2[\mathrm{BTC}]^4 - 2k_2[\mathrm{Cu}]^2[\mathrm{BTC}]^3[\mathrm{Area}] - k_3[\mathrm{Cu}][\mathrm{BTC}]^3 + k_{3r}[\mathrm{CuBTC_3}] \quad \text{(B.1)}$$

$$\frac{d[N_c]}{dt} = k_1[\mathrm{Cu}]^2[\mathrm{BTC}]^4 \tag{B.2}$$

$$\frac{d[MOF]}{dt} = 2\frac{d[N_c]}{dt} + 2k_2[\mathrm{Cu}]^2[\mathrm{BTC}]^3[\mathrm{Area}] + 2k_4[\mathrm{CuBTC_3}]^2 \tag{B.3}$$

$$\frac{d[\mathrm{CuBTC_3}]}{dt} = k_3[\mathrm{Cu}][\mathrm{BTC}]^3 - k_{3r}[\mathrm{CuBTC_3}] \tag{B.4}$$

B.1.2 Derivation of the active area

As crystal growth is dependent on the already present area of CuBTC in solution, it is necessary to derive an expression that connects the total amount of CuBTC and the number of crystals in solution to an expression that can give a proportional area that those crystals can present to the solution. The derivation is shown in the following.

A is the active area of a single CuBTC crystal, V is the volume-equivalent of said CuBTC crystal. The crystals are approximated using spheres.

The volume of a crystal in the solution will be directly proportionate to the MOF mass in the crystal. The mean CuBTC mass ($\bar{m}(MOF)$) of a crystal in the solution can be calculated using:

$$\bar{m}(MOF) = \frac{[MOF]_{total}}{N_c} \tag{B.5}$$

With N_c as the number of crystals in the solution and $[MOF]_{total}$ the total mass of CuBTC in solution. Any proportionality factor between the mass of the crystal and its volume will be folded into the final kinetic constant which is why for the purpose of getting an active area we can equate the mass with the crystal volume and omit the proportionality factor.

$$\bar{m}(MOF) \cong \bar{V}(MOF) \tag{B.6}$$

For the surface A and volume V equations of a sphere we have:

$$A = 4\pi r^2 \tag{B.7}$$

$$V = \frac{4}{3}\pi r^3 \tag{B.8}$$

We thus obtain

$$A = 4 \cdot \pi \left(\frac{3V}{4\pi} \right)^{2/3} \tag{B.9}$$

Inserting equation (B.5) we obtain:

$$A \cong 4 \cdot \pi \left(\frac{3[MOF]_{total}}{4\pi N_c} \right)^{2/3} \tag{B.10}$$

Expression (B.10) directly links the total amount of CuBTC and the number of crystals in the solution to a mean presented area per crystal. Multiplication by the amount of crystals N_c yields the total available active area.

$$[\text{Area}] = A \cdot N_c \tag{B.11}$$

This expression can then be directly plugged into the rate equations (B.1) and (B.3). It should be noted that any proportionality between this area and the size of the unit cell and the actual activity of a certain unit area are contained in the kinetic rate constants of the corresponding reactions.

B.1.3 Details on the modelling procedure and rate constants

The numerical model was set up in custom-made Python code. After initiation of starting concentrations of the Cu^{2+} and BTC the code calculated the concentration differences between a point t_0 and a point t by inserting the current concentrations at time t_0 into the rate equations. The resulting change in concentration is added to the concentration at t_0 to obtain the concentration at t. The cycle was repeated 40000 times for every model experiment. Since the time step is not defined, the units for the kinetic constants are related to an arbitrary time unit. The kinetic constants used for all model evaluations were:

- $k_1 = 1 \cdot 10^5$ $\text{L}^5\text{mol}^{-5}$
- $k_2 = 5 \cdot 10^9$ $\text{L}^4\text{mol}^{-4}\text{m}^{-2}$
- $k_3 = 200$ $\text{L}^3\text{mol}^{-3}$
- $k_{3r} = 1 \cdot 10^{-4}$

- $k_4 = 500\ \mathrm{Lmol}^{-1}$

We know from the experiments that the equilibrium reaction between the active and less-active species forms very quickly (see discussion to Figure 5.3). If we choose k_{3r} and k_3 too high ($k_3 \approx> 2000\ \mathrm{L}^3\mathrm{mol}^{-3}$, $k_{3r} \approx> 1 \cdot 10^{-2}$) our model breaks down due to the discrete nature of the numerical evaluation. If an iteration of the loop yields negative changes in concentration that are larger than the existing concentration of the species (which can happen if the rate constants are chosen too high), the result will be a negative total concentration in the next loop and the model stops functioning. To avoid this issue, we evaluate only the back and forth reactions in equation (5.8) in the chapter 5 20000 times to allow formation of a stable equilibrium between the active and less-active copper species before starting the full simulation. As afterwards the concentration changes are small, the equilibrium in equation (5.8) forms immediately after every loop.

The issue could be prevented by scaling down all rate constants and increasing the simulation length. However, we estimate to have to increase the amount of evaluation-loops by at least 3 orders of magnitude which would increase the total time for a single simulation to around 17-20 hours (and would most likely lead to physical memory issues) whereas currently we can simulate a full experiment in around 1 min.

The simulations were performed on a commercial personal computer.

Comparison of different rate constants

Figure B.1 shows the results of models set up with rate constants different from the ones used for 5.4. The rate constants are detailed in Table B.1. In Figure B.1 a) the reactions to and from the inhibiting species $CuBTC_3$ have been turned off by setting their rate constants to 0. It can be seen that now the model follows chemical intuition. As the concentration of BTC increases, the overall rate of the CuBTC production also increases. In addition at higher BTC concentrations the induction period at the beginning of the growth gets significantly shorter.

In Figure B.1 b) the only change to the rate constants was that the rate constant for nucleation k_1 was reduced by one order of magnitude compared to the model that is shown in Figure

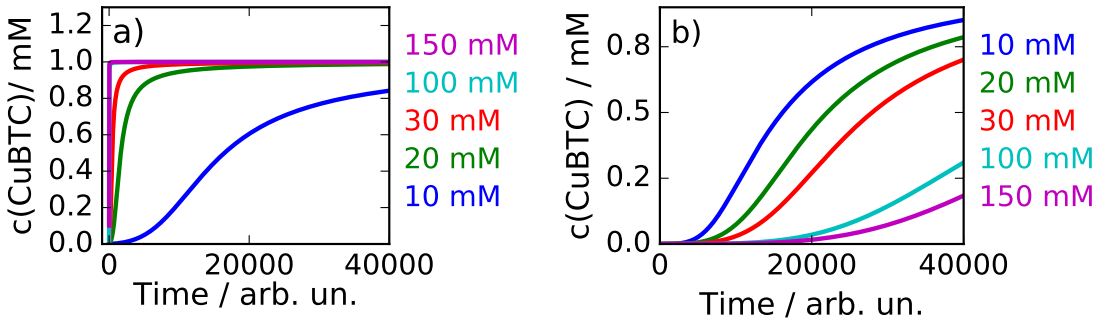

Figure B.1 Comparison of model evaluations at different BTC concentrations with kinetic rate constants that do not manage to reproduce the experimental observations (rate constants in Table B.1). a) No inhibiting reaction. b) Reduced rate constant k_1 for nucleation. The legend shows the BTC concentrations used.

5.4. We observe that while the inhibiting effect of higher BTC concentrations is still present the induction period at the beginning of the reaction is now much longer.

B.2 Comparison of the UV/VIS response of pure copper nitrate and copper nitrate with BTC

Figure B.2 shows a direct comparison of the UV/VIS response of a copper nitrate solution containing BTC and a solution not containing BTC immediately after mixing of the solution, so before a reaction to CuBTC can take place. The spectra match well, the only difference being a slight overall blue shift of the spectrum with BTC, which is discussed in Figure 5.3.

Table B.1 Rate constants for the model evaluations in Figure B.1

	k_1/L^{5}mol^{-5}	k_2 / L^{4}mol^{-4}m^{-2}	k_3 / L^{3}mol^{-3}	k_{3r}	k_4 / Lmol^{-1}
a)	$1 \cdot 10^5$	$1 \cdot 10^9$	0	0	0
b)	$5 \cdot 10^3$	$5 \cdot 10^9$	200	$1 \cdot 10^{-4}$	500

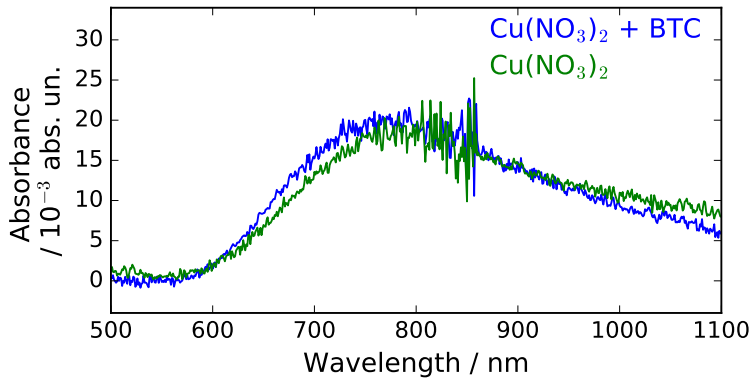

Figure B.2 UV/VIS spectra of 1 mM pure copper nitrate semipentahydrate in ethanol (green) and 1 mM copper nitrate and BTC (9 mM) in ethanol (blue) immediately after mixing of the solutions.

B.3 Non-negative least squares fit for determination of component concentrations

To devonvolute the contributions of the two chemical species from the UV/VIS spectra, we use a simple non-negative least squares procedure as it is implemented in Python as it is implemented in the scipy.optimize package using the Levenberg-Marquardt algorithm.[157]

The total spectral response S_{tot} is composed of two separate spectral components S_1 and S_2 (which are shown in Figure 5.1) which are weighted with their specific contributions c_1 and c_2 according to:

$$S_{tot} = c_1 \cdot S_1 + c_2 \cdot S_2 \tag{B.12}$$

S_1, S_{tot} and S_2 are in a data sense vectors that represent the intensity distribution of the given component over the investigated spectral range. Using a common fitting procedure (in our case in Python) with equation (B.12) as its target equation, S_{tot} as the data to be fit and S_1 and S_2 as the corresponding x-values will give the coefficients c_1 and c_2 that are shown in Figure 5.1 c).[158]

The spectral components S_1 and S_2 are determined as follows:

For S_1 we take the spectral response of a pure ethanolic solution of $Cu(NO_3)_2$ x $2.5H_2O$. Since we do not want to put any presumptions into the choice of S_2, we calculate S_2 using

the equation (B.12) as a free floating component that is the same for a set of spectra. Due to computational limitations we only used the 100 first spectra of one measurement.

Algorithmically the principle was the following: The matrix containing 100 spectra with their intensities for every wavelength (600 data points per spectrum) was flattened to one dimension, giving a data vector that is 100 times as long as one measurement has intensity values (60000 data points). The input spectrum S_1 (length 600 data points) is duplicated 100 times, to match the shape of the data vector. We then run the same fitting procedure as described before, using 800 fitting parameters. 200 of those are used for c_1 and c_2 of the 100 spectra and the 600 remaining ones are the intensity values of the to determined component S_2. The fitting guess for S_2 is again duplicated 100 times in every fitting loop, ensuring that the same S_2 will be used for all spectra.

The above described procedure yields the spectrum for component 2 (see Figure 5.1 b)), which does not contain any assumptions concerning its shape. It is then used in the NNLS algorithm that uses both S_1 and S_2 as inputs for the rest of the data. This two-step strategy overcomes the computational limitations that we meet if we try to fit the whole data set using a free-floating second spectral component.

B.3.1 Kinetic traces of component 1

Figure B.3 shows the fit coefficients of component 1 (the Cu^{2+} precursor) throughout the course of the experiments shown in Figure 5.2. We observe a similar behavior to the trace of coefficient 1 in Figure 5.1. Initially the contribution of the component decreases for almost all traces. After some time the component contribution reaches a minimum and starts increasing afterwards. The behavior can be understood as discussed in section 5.2.

Due to the scattering it can also be expected that component 2 (CuBTC) will be overestimated from the fit. This does not change our conclusions about the overall rate of CuBTC production and the relative growth acceleration at low BTC concentrations.

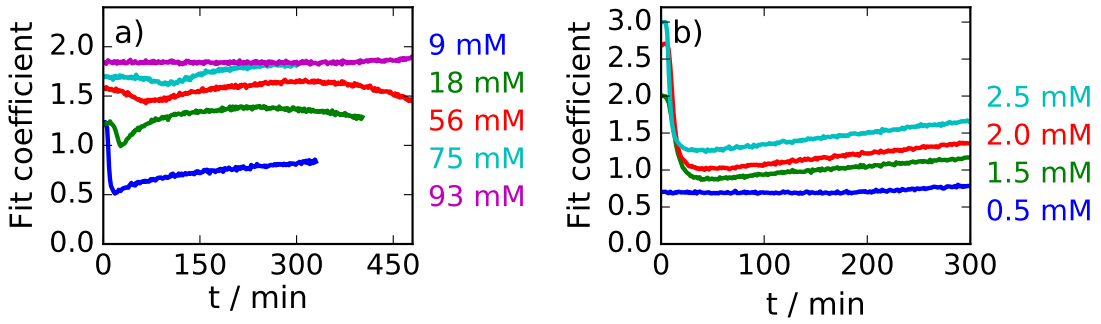

Figure B.3 Fit coefficients for component 1, identified as $Cu(NO_3)_2$ x 2.5 H_2O, over the time of the experiments at different concentration conditions. a) Fit coefficient vs time at different BTC concentrations as noted in the legend. The Cu^{2+} concentration was fixed at 1 mM. b) Fit coefficient vs time at different Cu^{2+} concentrations as noted in the legend. The BTC concentration was fixed at 38 mM.

B.4 Derivation of the fit function for the chemical equilibrium in Figure 5.3

Assume three chemical species, Cu^{2+}, BTC and $CuBTC_x$, that are connected through a chemical equilibrium reaction:

$$Cu^{2+} + xBTC \longleftrightarrow CuBTC_x \tag{B.13}$$

Their equilibrium constant K can be calculated using the concentrations of the species in equilibrium, $[Cu^{2+}]$, [BTC] and $[CuBTC_x]$.

$$K = \frac{[CuBTC_x]}{[Cu^{2+}] \cdot [BTC]^x} \tag{B.14}$$

Assuming the two Cu^{2+} containing species show different UV/VIS responses in a given spectral range, the total UV/VIS absorbance I_{tot} in the observed spectral range can be calculated using:

$$I_{tot} = \varepsilon_{tot,1} \cdot [Cu^{2+}] + \varepsilon_{tot,2} \cdot [CuBTC_x] \tag{B.15}$$

Where $\varepsilon_{tot,1}$ and $\varepsilon_{tot,2}$ are the integrated absorbance coefficients in the observed spectral range.

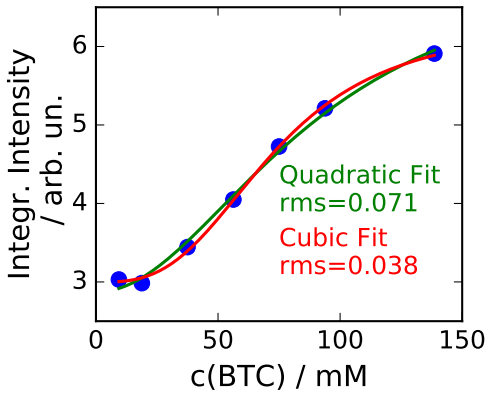

Figure B.4 Comparison of a quadratic (x=2, green) and cubic (x=3, red) fit to equation (B.22) with the data from Figure 5.3. The rms value is the root-mean-square of the fit residuals.

Equation (B.14) can be used to express $[\mathrm{CuBTC_x}]$ as follows:

$$[\mathrm{CuBTC_x}] = K \cdot \left[\mathrm{Cu^{2+}}\right] \cdot [\mathrm{BTC}]^x \tag{B.16}$$

Inserting equation (B.16) into (B.15) yields

$$I_{tot} = \varepsilon_{tot,1} \cdot \left[\mathrm{Cu^{2+}}\right] + \varepsilon_{tot,2} \cdot K \cdot \left[\mathrm{Cu^{2+}}\right] \cdot [\mathrm{BTC}]^x \tag{B.17}$$

$$= \left[\mathrm{Cu^{2+}}\right] \cdot (\varepsilon_{tot,1} + \varepsilon_{tot,2} \cdot K \cdot [\mathrm{BTC}]^x) \tag{B.18}$$

Since we assume these are the only chemical species present, the sum of the concentrations of $\mathrm{Cu^{2+}}$ and $\mathrm{CuBTC_x}$ needs to be equal to the initial concentration of $\mathrm{Cu^{2+}}$, $\left[\mathrm{Cu^{2+}}\right]_0$:

$$\left[\mathrm{Cu^{2+}}\right]_0 = \left[\mathrm{Cu^{2+}}\right] + [\mathrm{CuBTC_x}] \tag{B.19}$$

Inserting (B.16) into (B.19) yields:

$$\left[\mathrm{Cu^{2+}}\right]_0 = \left[\mathrm{Cu^{2+}}\right] + K \cdot \left[\mathrm{Cu^{2+}}\right] \cdot [\mathrm{BTC}]^x \tag{B.20}$$

$$\left[\mathrm{Cu^{2+}}\right] = \frac{\left[\mathrm{Cu^{2+}}\right]_0}{1 + K \cdot [\mathrm{BTC}]^x} \tag{B.21}$$

Inserting (B.21) into (B.18) gives:

$$I_{tot} = \frac{\left[\mathrm{Cu^{2+}}\right]_0}{1 + K \cdot [\mathrm{BTC}]^x} \cdot (\varepsilon_{tot,1} + \varepsilon_{tot,2} \cdot K \cdot [\mathrm{BTC}]^x) \tag{B.22}$$

Equation (B.22) can now be used to fit a plot of the total intensity where the two components show differences in their total absorbance coefficients ε_{tot} to calculate both $\varepsilon_{1,tot}$, $\varepsilon_{2,tot}$ and K.

Figure B.4 shows a comparison of a quadratic and a cubic fit of equation (B.22) to the experimental data. The root-mean-square of the fit residuals shows that the cubic fit indeed fits the experimental data better by a factor of ≈ 2.

References

[1] K. Satoh and K. Funatsu, "A Novel Approach to Retrosynthetic Analysis Using Knowledge Bases Derived from Reaction Databases," *Journal of Chemical Information and Modeling*, vol. 39, no. 2, pp. 316–325, 1999.

[2] K. C. Nicolaou, B. S. Safina, Mark Zak, Sang Hyup Lee, Marta Nevalainen, Marco Bella, Anthony A. Estrada, Christian Funke, F. J. Zécri, and S. Bulat, "Total Synthesis of Thiostrepton. Retrosynthetic Analysis and Construction of Key Building Blocks," *Journal of the American Chemical Society*, vol. 127, no. 31, pp. 11159–11175, 2005.

[3] G. Odian, *Principles of Polymerization*. New Jersey: John Wiley & Sons, Inc., 4 ed., 2004.

[4] J. Jagur-Grodzinski, "Functional polymers by living anionic polymerization," *Journal of Polymer Science Part A: Polymer Chemistry*, vol. 40, no. 13, pp. 2116–2133, 2002.

[5] E. Mishima, Y. Matsumiya, S. Yamago, and H. Watanabe, "Kinetics of Living Anionic Polymerization of Polystyrenyl Lithium in Cyclohexane," *Polymer Journal*, vol. 40, no. 8, pp. 749–762, 2008.

[6] E. C. Constable and C. E. Housecroft, "Coordination chemistry: the scientific legacy of Alfred Werner," *Chemical Society Reviews*, vol. 42, no. 4, pp. 1429–1439, 2013.

[7] E. Riedel, *Allgemeine und Anorganische Chemie*. de Gruyter, 10 ed., 2010.

[8] J.-M. Brégeault, "Transition-metal complexes for liquid-phase catalytic oxidation: some aspects of industrial reactions and of emerging technologies," *Dalton Transactions*, no. 17, pp. 3289–3302, 2003.

[9] S. Krompiec, M. Penkala, K. Szczubiałka, and E. Kowalska, "Transition metal compounds and complexes as catalysts in synthesis of acetals and orthoesters: Theoretical, mechanistic and practical aspects," *Coordination Chemistry Reviews*, vol. 256, no. 17, pp. 2057–2095, 2012.

[10] J. J. Eisch, "Fifty Years of Ziegler–Natta Polymerization: From Serendipity to Science. A Personal Account," *Organometallics*, vol. 31, no. 14, pp. 4917–4932, 2012.

[11] M. Grätzel, "Dye-sensitized solar cells," *Journal of Photochemistry and Photobiology C: Photochemistry Reviews*, vol. 4, no. 2, pp. 145–153, 2003.

[12] S. Kitagawa, R. Kitaura, and S.-i. Noro, "Functional porous coordination polymers.," *Angewandte Chemie International Edition*, vol. 43, no. 18, pp. 2334–2375, 2004.

[13] O. M. Yaghi, H. Li, M. Eddaoudi, and M. O'Keeffe, "Design and synthesis of an exceptionally stable and highly porous metal-organic framework," *Nature*, vol. 402, no. 6759, pp. 276–279, 1999.

[14] A. Karmakar, B. Joarder, A. Mallick, P. Samanta, A. V. Desai, S. Basu, and S. K. Ghosh, "Aqueous Phase Sensing of Cyanide Ion Using a Hydrolytically Stable Metal-organic Framework," *Chemical Communications*, vol. 53, pp. 1253–1256, 2017.

[15] P. Horcajada, C. Serre, M. Vallet-Regí, M. Sebban, F. Taulelle, and G. Férey, "Metal–Organic Frameworks as Efficient Materials for Drug Delivery," *Angewandte Chemie International Edition*, vol. 45, no. 36, pp. 5974–5978, 2006.

[16] D. Britt, D. Tranchemontagne, and O. M. Yaghi, "Metal-organic frameworks with high capacity and selectivity for harmful gases," *Proceedings of the National Academy of Sciences of the United States of America*, vol. 105, no. 33, pp. 11623–11627, 2008.

[17] J. Teufel, H. Oh, M. Hirscher, M. Wahiduzzaman, L. Zhechkov, A. Kuc, T. Heine, D. Denysenko, and D. Volkmer, "MFU-4 – A Metal-Organic Framework for Highly Effective H2/D2 Separation," *Advanced Materials*, vol. 25, no. 4, pp. 635–639, 2013.

[18] H. Liu, S. Zhang, Y. Liu, Z. Yang, X. Feng, X. Lu, and F. Huo, "Well-Dispersed and Size-Controlled Supported Metal Oxide Nanoparticles Derived from MOF Composites and Further Application in Catalysis," *Small*, vol. 11, no. 26, pp. 3130–3134, 2015.

[19] A. U. Czaja, N. Trukhan, and U. Müller, "Industrial applications of metal-organic frameworks.," *Chemical Society Reviews*, vol. 38, no. 5, pp. 1284–93, 2009.

[20] M. A. Nasalevich, M. van der Veen, F. Kapteijn, and J. Gascon, "Metal–organic frameworks as heterogeneous photocatalysts: advantages and challenges," *CrystEngComm*, vol. 16, no. 23, p. 4919, 2014.

[21] R. S. Kumar, S. S. Kumar, and M. A. Kulandainathan, "Highly selective electrochemical reduction of carbon dioxide using Cu based metal organic framework as an electrocatalyst," *Electrochemistry Communications*, vol. 25, pp. 70–73, 2012.

[22] L. Ma, C. Abney, and W. Lin, "Enantioselective catalysis with homochiral metal–organic frameworks," *Chemical Society Reviews*, vol. 38, no. 5, pp. 1248–1256, 2009.

[23] H.-C. Zhou, J. R. Long, and O. M. Yaghi, "Introduction to Metal–Organic Frameworks," *Chemical Reviews*, vol. 112, no. 2, pp. 673–674, 2012.

[24] Y.-Q. Hu, M.-Q. Li, T. Li, Y.-Y. Wang, Z. Zheng, and Y.-Z. Zheng, "An alkali-ion insertion approach to structurally transform metal–organic frameworks," *CrystEngComm*, vol. 18, no. 40, pp. 7680–7684, 2016.

[25] M.-H. Pham, G.-T. Vuong, F.-G. Fontaine, and T.-O. Do, "Rational Synthesis of Metal–Organic Framework Nanocubes and Nanosheets Using Selective Modulators and Their Morphology-Dependent Gas-Sorption Properties," *Crystal Growth & Design*, vol. 12, no. 6, pp. 3091–3095, 2012.

[26] D. Cai, B. Liu, D. Wang, L. Wang, Y. Liu, B. Qu, X. Duan, Q. Li, and T. Wang, "Rational synthesis of metal–organic framework composites, hollow structures and

their derived porous mixed metal oxide hollow structures," *Journal of Materials Chemistry A*, vol. 4, no. 1, pp. 183–192, 2016.

[27] O. K. Farha and J. T. Hupp, "Rational Design, Synthesis, Purification, and Activation of Metal-Organic Framework Materials," *Accounts of Chemical Research*, vol. 43, no. 8, pp. 1166–1175, 2010.

[28] A. U. Czaja, N. Trukhan, and U. Müller, "Industrial applications of metal–organic frameworks," *Chemical Society Reviews*, vol. 38, no. 5, pp. 1284–1293, 2009.

[29] P. Silva, S. M. F. Vilela, J. P. C. Tomé, and F. A. Almeida Paz, "Multifunctional metal–organic frameworks: from academia to industrial applications," *Chemical Society Reviews*, vol. 44, no. 19, pp. 6774–6803, 2015.

[30] J. Won, J. S. Seo, J. H. Kim, H. S. Kim, Y. S. Kang, S.-J. Kim, Y. Kim, and J. Jegal, "Coordination Compound Molecular Sieve Membranes," *Advanced Materials*, vol. 17, no. 1, pp. 80–84, 2005.

[31] B. Chen, S. Xiang, and G. Qian, "Metal-Organic Frameworks with Functional Pores for Recognition of Small Molecules," *Accounts of Chemical Research*, vol. 43, no. 8, pp. 1115–1124, 2010.

[32] S. Basu, M. Maes, A. Cano-Odena, L. Alaerts, D. E. De Vos, and I. F. Vankelecom, "Solvent resistant nanofiltration (SRNF) membranes based on metal-organic frameworks," *Journal of Membrane Science*, vol. 344, no. 1, pp. 190–198, 2009.

[33] M. F. de Lange, T. Zeng, T. J. H. Vlugt, J. Gascon, and F. Kapteijn, "Manufacture of dense CAU-10-H coatings for application in adsorption driven heat pumps: optimization and characterization," *CrystEngComm*, vol. 17, no. 31, pp. 5911–5920, 2015.

[34] D. Fröhlich, E. Pantatosaki, P. D. Kolokathis, K. Markey, H. Reinsch, M. Baumgartner, M. A. van der Veen, D. E. De Vos, N. Stock, G. K. Papadopoulos, S. K. Henninger, and C. Janiak, "Water adsorption behaviour of CAU-10-H: a thorough investigation of its structure–property relationships," *Journal of Materials Chemistry A*, vol. 4, no. 30, pp. 11859–11869, 2016.

[35] M.-S. Yao, W.-X. Tang, G.-E. Wang, B. Nath, and G. Xu, "MOF Thin Film-Coated Metal Oxide Nanowire Array: Significantly Improved Chemiresistor Sensor Performance," *Advanced Materials*, vol. 28, no. 26, pp. 5229–5234, 2016.

[36] J. Cravillon, C. A. Schroder, R. Nayuk, J. Gummel, K. Huber, and M. Wiebcke, "Fast Nucleation and Growth of ZIF-8 Nanocrystals Monitored by Time-Resolved In Situ Small-Angle and Wide-Angle X-Ray Scattering," *Angewandte Chemie International Edition*, vol. 50, no. 35, pp. 8067–8071, 2011.

[37] M. G. Goesten, E. Stavitski, J. Juan-Alcaniz, A. Martinez-Joaristi, A. V. Petukhov, F. Kapteijn, and J. Gascon, "Small-angle X-ray scattering documents the growth of metal-organic frameworks," *Catalysis Today*, vol. 205, pp. 120–127, 2013.

[38] D. J. Tranchemontagne, J. L. Mendoza-Cortés, M. O'Keeffe, and O. M. Yaghi, "Secondary building units, nets and bonding in the chemistry of metal–organic frameworks," *Chemical Society Reviews*, vol. 38, no. 5, pp. 1257–1283, 2009.

[39] M. Eddaoudi, J. Kim, D. Vodak, A. Sudik, J. Wachter, M. O'Keeffe, and O. M. Yaghi, "Geometric requirements and examples of important structures in the assembly of square building blocks.," *Proceedings of the National Academy of Sciences of the United States of America*, vol. 99, no. 8, pp. 4900–4904, 2002.

[40] O. M. Yaghi, M. O'Keeffe, N. W. Ockwig, H. K. Chae, M. Eddaoudi, and J. Kim, "Reticular synthesis and the design of new materials," *Nature*, vol. 423, no. 6941, pp. 705–714, 2003.

[41] C. Dey, T. Kundu, B. P. Biswal, A. Mallick, and R. Banerjee, "Crystalline metal-organic frameworks (MOFs): synthesis, structure and function," *Acta Crystallographica Section B*, vol. 70, no. 1, pp. 3–10, 2014.

[42] S. Qiu, M. Xue, and G. Zhu, "Metal–organic framework membranes: from synthesis to separation application," *Chemical Society Reviews*, vol. 43, no. 16, pp. 6116–6140, 2014.

[43] D. Nagaraju, D. G. Bhagat, R. Banerjee, and U. K. Kharul, "In situ growth of metal-organic frameworks on a porous ultrafiltration membrane for gas separation," *Journal of Materials Chemistry A*, vol. 1, no. 31, p. 8828, 2013.

[44] Z. Wang, J. Wang, M. Li, K. Sun, and C.-j. Liu, "Three-dimensional Printed Acrylonitrile Butadiene Styrene Framework Coated with Cu-BTC Metal-organic Frameworks for the Removal of Methylene Blue," *Scientific Reports*, vol. 4, pp. S313–S318, 2014.

[45] S. Hermes, F. Schröder, R. Chelmowski, C. Wöll, and R. A. Fischer, "Selective nucleation and growth of metal-organic open framework thin films on patterned COOH/CF3-terminated self-assembled monolayers on Au(111).," *Journal of the American Chemical Society*, vol. 127, no. 40, pp. 13744–5, 2005.

[46] E. Biemmi, C. Scherb, and T. Bein, "Oriented growth of the metal organic framework Cu3(BTC)2(H2O)3.xH2O tunable with functionalized self-assembled monolayers.," *Journal of the American Chemical Society*, vol. 129, no. 26, pp. 8054–8055, 2007.

[47] C. Scherb, A. Schödel, and T. Bein, "Directing the Structure of Metal–Organic Frameworks by Oriented Surface Growth on an Organic Monolayer," *Angewandte Chemie International Edition*, vol. 47, no. 31, pp. 5777–5779, 2008.

[48] H. Zhu and S. Zhu, "A versatile and facile surface modification route based on polydopamine for the growth of MOF films on different substrates," *The Canadian Journal of Chemical Engineering*, vol. 93, no. 1, pp. 63–67, 2015.

[49] U. Mueller, H. Puetter, M. Hesse, M. Schubert, H. Wessel, J. Huff, and M. Guzmann, "Method for electrochemical production of a crystalline porous metal organic skeleton material," 2004.

[50] R. Ameloot, L. Stappers, J. Fransaer, L. Alaerts, B. F. Sels, and D. E. De Vos, "Patterned Growth of Metal-Organic Framework Coatings by Electrochemical Synthesis," *Chemistry of Materials*, vol. 21, no. 13, pp. 2580–2582, 2009.

[51] A. Martinez Joaristi, J. Juan-Alcañiz, P. Serra-Crespo, F. Kapteijn, and J. Gascon, "Electrochemical Synthesis of Some Archetypical Zn 2+ , Cu 2+ , and Al 3+ Metal Organic Frameworks," *Crystal Growth & Design*, vol. 12, no. 7, pp. 3489–3498, 2012.

[52] H. Al-Kutubi, J. Gascon, E. J. R. Sudhölter, and L. Rassaei, "Electrosynthesis of Metal-Organic Frameworks: Challenges and Opportunities," *ChemElectroChem*, vol. 2, no. 4, pp. 462–474, 2015.

[53] M. Y. Li and M. Dinca, "Reductive Electrosynthesis of Crystalline Metal-Organic Frameworks," *Journal of the American Chemical Society*, vol. 133, no. 33, pp. 12926–12929, 2011.

[54] M. Y. Li and M. Dinca, "Selective formation of biphasic thin films of metal-organic frameworks by potential-controlled cathodic electrodeposition," *Chemical Science*, vol. 5, no. 1, pp. 107–111, 2014.

[55] Y. Sun, H.-C. Zhou, L. J. R. M, and Y. O, "Recent progress in the synthesis of metal–organic frameworks," *Science and Technology of Advanced Materials*, vol. 16, no. 5, p. 054202, 2015.

[56] T. R. Van Assche, G. Desmet, R. Ameloot, D. E. De Vos, H. Terryn, and J. F. Denayer, "Electrochemical synthesis of thin HKUST-1 layers on copper mesh," *Microporous and Mesoporous Materials*, vol. 158, pp. 209–213, 2012.

[57] C. Warakulwit, S. Yadnum, C. Boonyuen, C. Wattanakit, A. Karajic, P. Garrigue, N. Mano, D. Bradshaw, J. Limtrakul, and A. Kuhn, "Elaboration of metal organic framework hybrid materials with hierarchical porosity by electrochemical deposition–dissolution," *CrystEngComm*, vol. 18, no. 27, pp. 5095–5100, 2016.

[58] E. García-Pérez, J. Gascón, V. Morales-Flórez, J. M. Castillo, F. Kapteijn, and S. Calero, "Identification of Adsorption Sites in Cu-BTC by Experimentation and Molecular Simulation," *Langmuir*, vol. 25, no. 3, pp. 1725–1731, 2009.

[59] A. O. Yazaydın, A. I. Benin, S. A. Faheem, P. Jakubczak, J. J. Low, R. R. Willis, and R. Q. Snurr, "Enhanced CO2 Adsorption in Metal-Organic Frameworks via Occupation of Open-Metal Sites by Coordinated Water Molecules," *Chemistry of Materials*, vol. 21, no. 8, pp. 1425–1430, 2009.

[60] S. S. Y. Chui, S. M. F. Lo, J. P. H. Charmant, a. G. Orpen, and I. D. Williams, "A Chemically Functionalizable Nanoporous Material [Cu3(TMA)2(H2O)3]n," *Science*, vol. 283, no. 5405, pp. 1148–1150, 1999.

[61] B. Chen, Z. Yang, Y. Zhu, and Y. Xia, "Zeolitic imidazolate framework materials: recent progress in synthesis and applications," *Journal of Materials Chemistry A*, vol. 2, no. 40, pp. 16811–16831, 2014.

[62] J. P. Patterson, P. Abellan, M. S. Denny, C. Park, N. D. Browning, S. M. Cohen, J. E. Evans, and N. C. Gianneschi, "Observing the Growth of Metal–Organic Frameworks by in Situ Liquid Cell Transmission Electron Microscopy," *Journal of the American Chemical Society*, vol. 137, no. 23, pp. 7322–7328, 2015.

[63] M. Goesten, E. Stavitski, E. A. Pidko, C. Gücüyener, B. Boshuizen, S. N. Ehrlich, E. J. M. Hensen, F. Kapteijn, and J. Gascon, "The molecular pathway to ZIF-7 microrods revealed by in situ time-resolved small- and wide-angle x-ray scattering, quick-scanning extended X-ray absorption spectroscopy, and DFT calculations," *Chemistry - A European Journal*, vol. 19, no. 24, pp. 7809–7816, 2013.

[64] J. Grand, H. Awala, and S. Mintova, "Mechanism of zeolites crystal growth: new findings and open questions," *CrystEngComm*, vol. 18, no. 5, pp. 650–664, 2016.

[65] S. Biswas, T. Rémy, S. Couck, D. Denysenko, G. Rampelberg, J. F. M. Denayer, D. Volkmer, C. Detavernier, and P. Van Der Voort, "Partially fluorinated MIL-47 and Al-MIL-53 frameworks: influence of functionalization on sorption and breathing properties," *Physical Chemistry Chemical Physics*, vol. 15, no. 10, p. 3552, 2013.

[66] E. Haque, J. H. Jeong, and S. H. Jhung, "Synthesis of isostructural porous metal-benzenedicarboxylates: Effect of metal ions on the kinetics of synthesis," *CrystEng-Comm*, vol. 12, no. 10, p. 2749, 2010.

[67] E. Stavitski, M. Goesten, J. Juan-Alcañiz, A. Martinez-Joaristi, P. Serra-Crespo, A. V. Petukhov, J. Gascon, and F. Kapteijn, "Kinetic control of metal-organic framework crystallization investigated by time-resolved in-situ X-ray scattering.," *Angewandte Chemie International Edition*, vol. 50, no. 41, pp. 9624–9628, 2011.

[68] S. Surblé, F. Millange, C. Serre, G. Férey, and R. I. Walton, "An EXAFS study of the formation of a nanoporous metal-organic framework: evidence for the retention of secondary building units during synthesis.," *Chemical Communications*, vol. 423, no. 14, pp. 1518–1520, 2006.

[69] F. Millange, M. I. Medina, N. Guillou, G. Férey, K. M. Golden, and R. I. Walton, "Time-Resolved In Situ Diffraction Study of the Solvothermal Crystallization of Some Prototypical Metal-Organic Frameworks," *Angewandte Chemie International Edition*, vol. 49, no. 4, pp. 763–766, 2010.

[70] S. Hermes, T. Witte, T. Hikov, D. Zacher, S. Bahnmüller, G. Langstein, K. Huber, and R. A. Fischer, "Trapping metal-organic framework nanocrystals: An in-situ time-resolved light scattering study on the crystal growth of MOF-5 in solution," *Journal of the American Chemical Society*, vol. 129, no. 17, pp. 5324–5325, 2007.

[71] P. Cubillas, M. W. Anderson, and M. P. Attfield, "Crystal Growth Mechanisms and Morphological Control of the Prototypical Metal-Organic Framework MOF-5 Revealed by Atomic Force Microscopy," *Chemistry - A European Journal*, vol. 18, no. 48, pp. 15406–15415, 2012.

[72] M. Shöâeé, M. W. Anderson, and M. P. Attfield, "Crystal Growth of the Nanoporous Metal-Organic Framework HKUST-1 Revealed by In Situ Atomic Force Microscopy," *Angewandte Chemie International Edition*, vol. 47, no. 44, pp. 8525–8528, 2008.

[73] N. S. John, C. Scherb, M. Shöâeè, M. W. Anderson, M. P. Attfield, and T. Bein, "Single layer growth of sub-micron metal-organic framework crystals observed by in situ atomic force microscopy.," *Chemical Communications*, vol. 2, no. 41, pp. 6294–6296, 2009.

[74] F. Millange, R. El Osta, M. E. Medina, and R. I. Walton, "A time-resolved diffraction study of a window of stability in the synthesis of a copper carboxylate metal–organic framework," *CrystEngComm*, vol. 13, no. 1, pp. 103–108, 2011.

[75] D. Zacher, J. Liu, K. Huber, and R. A. Fischer, "Nanocrystals of [Cu3(btc)2] (HKUST-1): a combined time-resolved light scattering and scanning electron microscopy study.," *Chemical Communications*, no. 9, pp. 1031–1033, 2009.

[76] M. L. Ohnsorg, C. K. Beaudoin, and M. E. Anderson, "Fundamentals of MOF Thin Film Growth via Liquid-Phase Epitaxy: Investigating the Initiation of Deposition and the Influence of Temperature," *Langmuir*, vol. 31, no. 22, pp. 6114–6121, 2015.

[77] O. Shekhah, H. Wang, D. Zacher, R. A. Fischer, and C. Wöll, "Growth mechanism of metal-organic frameworks: insights into the nucleation by employing a step-by-step route.," *Angewandte Chemie International Edition*, vol. 48, no. 27, pp. 5038–41, 2009.

[78] V. Stavila, J. Volponi, A. M. Katzenmeyer, M. C. Dixon, and M. D. Allendorf, "Kinetics and mechanism of metal–organic framework thin film growth: systematic investigation of HKUST-1 deposition on QCM electrodes," *Chemical Science*, vol. 3, no. 5, pp. 1531–1540, 2012.

[79] N. Campagnol, T. R. C. Van Assche, M. Li, L. Stappers, M. Dincă, J. F. M. Denayer, K. Binnemans, D. E. De Vos, and J. Fransaer, "On the electrochemical deposition of metal–organic frameworks," *Journal of Materials Chemistry A*, vol. 4, no. 10, pp. 3914–3925, 2016.

[80] C. M. A. Brett and A. M. O. Brett, *Electrochemistry : Principles, Methods and Applications*. Oxford: Oxford University Press, 2005.

[81] A. J. Bard and Faulkner, *Electrochemical Methods. Fundamentals and Applications*. New York: Wiley, 2 ed., 2001.

[82] K. Sato, S. Yoshimoto, J. Inukai, and K. Itaya, "Effect of sulfuric acid concentration on the structure of sulfate adlayer on Au(111) electrode," *Electrochemistry Communications*, vol. 8, no. 5, pp. 725–730, 2006.

[83] H.-H. Perkampus, *UV-VIS Spectroscopy and Its Applications*. Berlin: Springer Laboratory, 1 ed., 1992.

[84] D. A. Skoog, F. J. Holler, and T. A. Nieman, *Principles of Instrumental Analysis*. Belmont: Saunders College Publ., 7 ed., 2007.

[85] J. H. Van Vleck, "Theory of the Variations in Paramagnetic Anisotropy Among Different Salts of the Iron Group," *Physical Review*, vol. 41, no. 2, pp. 208–215, 1932.

[86] E. Pavarini, "Crystal-Field Theory, Tight-Binding Method and Jahn-Teller Effect," in *Correlated Electrons: From Models to Materials, Vol. 2*, ch. 6, pp. 6.2–6.39, Jülich: Verlag des Forschungszentrum Jülich, 2012.

[87] C. Prestipino, L. Regli, J. G. Vitillo, F. C. Bonino, A. A. Damin, C. Lamberti, A. Zecchina, P. L. Solari, K. O. Kongshaug, and S. Bordiga, "Local structure of framework Cu(II) in HKUST-1 metallorganic framework: Spectroscopic characterization upon activation and interaction with adsorbates," *Chemistry of Materials*, vol. 18, no. 5, pp. 1337–1346, 2006.

[88] E. Borfecchia, S. Maurelli, D. Gianolio, E. Groppo, M. Chiesa, F. Bonino, and C. Lamberti, "Insights into Adsorption of NH3 on HKUST-1 Metal–Organic Framework: A Multitechnique Approach," *The Journal of Physical Chemistry C*, vol. 116, no. 37, pp. 19839–19850, 2012.

[89] C. V. Raman and K. Krishnan, "A new type of secondary radiation," *Nature*, vol. 121, pp. 501–502, 1928.

[90] C. Raman, "A change of wave-length in light scattering," *Nature*, vol. 121, p. 619, 1928.

[91] C. V. Raman and K. Krishnan, "The optical analogue of the Compton effect," *Nature*, vol. 121, p. 711, 1928.

[92] H. W. Schrötter and H. W. Klöckner, "Raman Scattering Cross Sections in Gases and Liquids," in *Raman Spectroscopy of Gases and Liquids*, ch. 4, pp. 123–166, Berlin: Springer, 1979.

[93] J. Widengren, U. Mets, and R. Rigler, "Fluorescence correlation spectroscopy of triplet states in solution: a theoretical and experimental study," *The Journal of Physical Chemistry*, vol. 99, no. 36, pp. 13368–13379, 1995.

[94] E. C. Le Ru and P. G. Etchegoin, *Principles of Surface-Enhanced Raman Spectroscopy and related plasmonic effects*. Amsterdam: Elsevier, 1st ed., 2009.

[95] P. Atkins and J. de Paula, *Physical Chemistry*. Oxford: Oxford University Press, 10 ed., 2014.

[96] M. Fleischmann, P. Hendra, and A. McQuillan, "Raman spectra of pyridine adsorbed at a silver electrode," *Chemical Physics Letters*, vol. 26, no. 2, pp. 163–166, 1974.

[97] D. L. Jeanmaire and R. P. Van Duyne, "Surface raman spectroelectrochemistry: Part I. Heterocyclic, aromatic, and aliphatic amines adsorbed on the anodized silver electrode," *Journal of Electroanalytical Chemistry and Interfacial Electrochemistry*, vol. 84, no. 1, pp. 1–20, 1977.

[98] M. G. Albrecht and J. A. Creighton, "Anomalously intense Raman spectra of pyridine at a silver electrode," *Journal of the American Chemical Society*, vol. 99, no. 15, pp. 5215–5217, 1977.

[99] D. A. Weitz, S. Garoff, J. I. Gersten, and A. Nitzan, "The enhancement of Raman scattering, resonance Raman scattering, and fluorescence from molecules adsorbed on a rough silver surface," *The Journal of Chemical Physics*, vol. 78, no. 9, pp. 5324–5338, 1983.

[100] A. Campion and P. Kambhampati, "Surface-enhanced Raman scattering," *Chemical Society Reviews*, vol. 27, no. 4, pp. 241–250, 1998.

[101] V. M. Shalaev and A. K. Sarychev, "Nonlinear optics of random metal-dielectric films," *Physical Review B*, vol. 57, no. 20, pp. 13265–13288, 1998.

[102] Y. Fang, N.-H. Seong, and D. D. Dlott, "Measurement of the Distribution of Site Enhancements in Surface-Enhanced Raman Scattering," *Science*, vol. 321, no. 5887, pp. 388–392, 2008.

[103] P. F. Robusto and R. Braunstein, "Optical measurements of the surface plasmon of copper," *Physica Status Solidi b*, vol. 107, no. 2, pp. 443–449, 1981.

[104] Z.-Q. Tian, B. Ren, and D.-Y. Wu, "Surface-Enhanced Raman Scattering: From Noble to Transition Metals and from Rough Surfaces to Ordered Nanostructures," *Journal of Physical Chemistry B*, vol. 106, no. 37, pp. 9463–9483, 2002.

[105] H. Ko, S. Singamaneni, and V. V. Tsukruk, "Nanostructured Surfaces and Assemblies as SERS Media," *Small*, vol. 4, no. 10, pp. 1576–1599, 2008.

[106] M. J. Banholzer, J. E. Millstone, L. Qin, and C. A. Mirkin, "Rationally designed nanostructures for surface-enhanced Raman spectroscopy," *Chemical Society Reviews*, vol. 37, no. 5, p. 885, 2008.

[107] M. Muniz-Miranda, C. Gellini, and E. Giorgetti, "Surface-Enhanced Raman Scattering from Copper Nanoparticles Obtained by Laser Ablation," *The Journal of Physical Chemistry C*, vol. 115, no. 12, pp. 5021–5027, 2011.

[108] D. Irish, L. Stolberg, and D. Shoesmith, "Surface enhanced Raman spectroscopy and electrochemistry at the copper/iodide, water interface," *Surface Science*, vol. 158, no. 1-3, pp. 238–253, 1985.

[109] D.-Y. Wu, J.-F. Li, B. Ren, and Z.-Q. Tian, "Electrochemical surface-enhanced Raman spectroscopy of nanostructures.," *Chemical Society Reviews*, vol. 37, no. 5, pp. 1025–1041, 2008.

[110] Z.-Q. Tian and B. Ren, "Adsorption and reaction at electrochemical interfaces as probed by surface-enhanced Raman spectroscopy," *Annual Review of Physical Chemistry*, vol. 55, no. 1, pp. 197–229, 2004.

[111] P. H. C. Eilers, "A Perfect Smoother," *Analytical Chemistry*, vol. 75, no. 14, pp. 3631–3636, 2003.

[112] L. Reimer, *Scanning Electron Microscopy - Physics of Image Formation and Microanalysis*. Berlin: Springer, 1998.

[113] G. Haugstad, *ATOMIC FORCE MICROSCOPY - Understanding Basic Mdoes and Advanced Applications*. New Jersey: John Wiley & Sons, Inc., 2012.

[114] H. Solache-Carranco, G. Juarez-Diaz, M. Galvan-Arellano, J. Martinez-Juarez, G. Romero-Paredes R., and R. Pena-Sierra, "Raman scattering and photoluminescence studies on Cu2O," in *2008 5th International Conference on Electrical Engineering, Computing Science and Automatic Control*, pp. 421–424, IEEE, 2008.

[115] G. Mahalakshmi and V. Balachandran, "FT-IR and FT-Raman spectra, normal coordinate analysis and ab initio computations of Trimesic acid.," *Spectrochimica Acta. Part A*, vol. 124, pp. 535–47, 2014.

[116] Y. Kim, K. Cho, K. Lee, J. Choo, M.-s. Gong, and S.-W. Joo, "Electric field-induced adsorption change of 1,3,5-benzenetricarboxylic acid on gold, silver, and copper electrode surfaces investigated by surface-enhanced Raman scattering," *Journal of Molecular Structure*, vol. 878, no. 1-3, pp. 155–161, 2008.

[117] Y. Deng, A. D. Handoko, Y. Du, S. Xi, and B. S. Yeo, "In Situ Raman Spectroscopy of Copper and Copper Oxide Surfaces during Electrochemical Oxygen Evolution Reaction: Identification of Cu(III) Oxides as Catalytically Active Species," *ACS Catalysis*, vol. 6, no. 4, pp. 2473–2481, 2016.

[118] H. Y. H. Chan, C. G. Takoudis, and M. J. Weaver, "Oxide film formation and oxygen adsorption on copper in aqueous media as probed by surface-enhanced Raman spectroscopy," *Journal of Physical Chemistry B*, vol. 103, no. 2, pp. 357–365, 1999.

[119] I. Platzman, R. Brener, H. Haick, and R. Tannenbaum, "Oxidation of Polycrystalline Copper Thin Films at Ambient Conditions," *Journal of Physical Chemistry C*, vol. 112, no. 4, pp. 1101–1108, 2008.

[120] Q. Min Wang, D. Shen, M. Bülow, M. Ling Lau, S. Deng, F. R. Fitch, N. O. Lemcoff, and J. Semanscin, "Metallo-organic molecular sieve for gas separation and purification," *Microporous and Mesoporous Materials*, vol. 55, no. 2, pp. 217–230, 2002.

[121] B. Panella, M. Hirscher, H. Pütter, and U. Müller, "Hydrogen Adsorption in Metal–Organic Frameworks: Cu-MOFs and Zn-MOFs Compared," *Advanced Functional Materials*, vol. 16, no. 4, pp. 520–524, 2006.

[122] K. Nishi, T. Nishiumi, M. Higuchi, and K. Yamamoto, "A High Energy Rechargeable Battery Based on a One-Step Successive Two-Electron Transfer Process," *Electrochemical and Solid-State Letters*, vol. 8, no. 8, pp. A382–A384, 2005.

[123] K. Hinkelmann and J. Heinze, "Analysis of "two-electron" transfer processes by cyclic voltammetry," *Berichte der Bunsengesellschaft für physikalische Chemie*, vol. 91, no. 3, pp. 243–249, 1987.

[124] L. C. Hall, "Cyclic Voltammetric Study of Copper Electrode Pretreatment for Metal Migration and Corrosion Rates," *Journal of The Electrochemical Society*, vol. 134, no. 8, p. 1902, 1987.

[125] B. Stypuła, J. Banas, M. Starowicz, H. Krawiec, A. Bernasik, and A. Janas, "Production of nanoparticles of copper compounds by anodic dissolution of copper in organic solvents," *Journal of Applied Electrochemistry*, vol. 36, no. 12, pp. 1407–1414, 2006.

[126] T. R. Van Assche, G. Desmet, R. Ameloot, D. E. De Vos, H. Terryn, and J. F. Denayer, "Electrochemical synthesis of thin HKUST-1 layers on copper mesh," *Microporous and Mesoporous Materials*, vol. 158, pp. 209–213, aug 2012.

[127] H. Hagemann, H. Bill, W. Sadowski, E. Walker, and M. François, "Raman spectra of single crystal CuO," *Solid State Communications*, vol. 73, no. 6, pp. 447–451, 1990.

[128] G. Majano and J. Pérez-Ramírez, "Scalable Room-Temperature Conversion of Copper(II) Hydroxide into HKUST-1 (Cu3 (btc)2)," *Advanced Materials*, vol. 25, no. 7, pp. 1052–1057, 2013.

[129] J. C. Hamilton, J. Farmer, and R. Anderson, "In Situ Raman Spectroscopy of Anodic Films Formed on Copper and Silver in Sodium Hydroxide Solution," *Journal of The Electrochemical Society*, vol. 133, no. 4, p. 739, 1986.

[130] P. E. de Jongh, D. Vanmaekelbergh, J. J. Kelly, and P. E. D. Jongh, "Cu 2 O: Electrodeposition and Characterization," *Chemistry of Materials*, vol. 11, no. 12, pp. 3512–3517, 1999.

[131] D. Singh, N. Neti, A. Sinha, and O. Srivastava, "Growth of Different Nanostructures of Cu2O (Nanothreads, Nanowires, and Nanocubes) by Simple Electrolysis Based Oxidation of Copper," *Journal of Physical Chemistry C*, vol. 111, no. 4, pp. 1638–1645, 2007.

[132] W.-J. Li, J. Lü, S.-Y. Gao, Q.-H. Li, and R. Cao, "Electrochemical preparation of metal–organic framework films for fast detection of nitro explosives," *Journal of Materials Chemistry A*, vol. 2, no. 45, pp. 19473–19478, 2014.

[133] C. Rosman, J. Prasad, A. Neiser, A. Henkel, J. Edgar, and C. Sonnichsen, "Multiplexed Plasmon Sensor for Rapid Label-Free Analyte Detection," *Nano Letters*, vol. 13, no. 7, pp. 3243–3247, 2013.

[134] B. Han, Z. Li, S. Pronkin, and T. Wandlowski, "In situ ATR-SEIRAS study of adsorption and phase formation of trimesic acid on Au(111-25 nm) film electrodes," *Canadian Journal of Chemistry*, vol. 82, no. 10, pp. 1481–1494, 2004.

[135] C. Korzeniewski, V. Climent, and J. M. Feliu, "Electrochemistry at Platinum Single Crystal Electrodes," in *Electroanalytical Chemistry. A series of Advances*, pp. 75–170, CRC Press, 2011.

[136] J. Clavilier, D. Armand, S. Sun, and M. Petit, "Electrochemical adsorption behaviour of platinum stepped surfaces in sulphuric acid solutions," *Journal of Electroanalytical Chemistry and Interfacial Electrochemistry*, vol. 205, no. 1, pp. 267–277, 1986.

[137] A. Rodes, E. Herrero, J. M. Feliu, and A. Aldaz, "Structure sensitivity of irreversibly adsorbed tin on gold single-crystal electrodes in acid media," *Journal of the Chemical Society, Faraday Transactions*, vol. 92, no. 20, pp. 3769–3776, 1996.

[138] H. Villullas and M. Lopez Teijelo, "Meniscus shape and lateral wetting at the hanging meniscus rotating disc (HMRD) electrode," *Journal of Applied Electrochemistry*, vol. 26, no. 3, pp. 353–359, 1996.

[139] E. Herrero, L. J. Buller, and H. D. Abruña, "Underpotential Deposition at Single Crystal Surfaces of Au, Pt, Ag and Other Materials," *Chemical Reviews*, vol. 101, no. 7, pp. 1897–1930, 2001.

[140] T. Hachiya, H. Honbo, and K. Itaya, "Detailed underpotential deposition of copper on gold(III) in aqueous solutions," *Journal of Electroanalytical Chemistry and Interfacial Electrochemistry*, vol. 315, no. 1, pp. 275–291, 1991.

[141] G. Gunawardena, G. Hills, and I. Montenegro, "Electrochemical nucleation: Part IV. Electrodeposition of copper onto vitreous carbon," *Journal of Electroanalytical Chemistry and Interfacial Electrochemistry*, vol. 184, no. 2, pp. 357–369, 1985.

[142] H. Matsumoto, J. Inukai, and M. Ito, "Structures of copper and halides on Pt(111), Pt(100) and Au(111) electrode surfaces studied by in-situ scanning tunneling microscopy," *Journal of Electroanalytical Chemistry*, vol. 379, no. 1-2, pp. 223–231, 1994.

[143] D. K. Schwartz, "Mechanism and kinetics of self-assembled monolayer formation," *Annual Review of Physical Chemistry*, vol. 52, no. 1, pp. 107–137, 2001.

[144] B. Han, Z. Li, and T. Wandlowski, "Adsorption and self-assembly of aromatic carboxylic acids on Au/electrolyte interfaces.," *Analytical and Bioanalytical Chemistry*, vol. 388, no. 1, pp. 121–129, 2007.

[145] Z.-C. Zeng, S.-C. Huang, D.-Y. Wu, L.-Y. Meng, M.-H. Li, T.-X. Huang, J.-H. Zhong, X. Wang, Z.-L. Yang, and B. Ren, "Electrochemical Tip-Enhanced Raman Spec-

troscopy," *Journal of the American Chemical Society*, vol. 137, no. 37, pp. 11928–11931, 2015.

[146] D. Kurouski, M. Mattei, and R. P. Van Duyne, "Probing Redox Reactions at the Nanoscale with Electrochemical Tip-Enhanced Raman Spectroscopy," *Nano Letters*, vol. 15, no. 12, pp. 7956–7962, 2015.

[147] G. Ballerini, K. Ogle, and M.-G. Barthés-Labrousse, "The acid–base properties of the surface of native zinc oxide layers: An XPS study of adsorption of 1,2-diaminoethane," *Applied Surface Science*, vol. 253, no. 16, pp. 6860–6867, 2007.

[148] R. Vaidhyanathan, S. S. Iremonger, K. W. Dawson, and G. K. H. Shimizu, "An amine-functionalized metal organic framework for preferential CO2 adsorption at low pressures," *Chemical Communications*, no. 35, pp. 5230–5232, 2009.

[149] D. N. Dybtsev, H. Chun, and K. Kim, "Rigid and flexible: A highly porous metal-organic framework with unusual guest-dependent dynamic behavior," *Angewandte Chemie International Edition*, vol. 43, no. 38, pp. 5033–5036, 2004.

[150] M. Kramer, U. Schwarz, and S. Kaskel, "Synthesis and properties of the metal-organic framework Mo3(BTC)2 (TUDMOF-1)," *Journal of Materials Chemistry*, vol. 16, no. 23, pp. 2245–2248, 2006.

[151] O. Shekhah, H. Wang, D. Zacher, R. A. Fischer, and C. Wöll, "Growth Mechanism of Metal-Organic Frameworks: Insights into the Nucleation by Employing a Step-by-Step Route," *Angewandte Chemie International Edition*, vol. 48, no. 27, pp. 5038–5041, 2009.

[152] Z.-Q. Li, A. Wang, C.-Y. Guo, Y.-F. Tai, and L.-G. Qiu, "One-pot synthesis of metal–organic framework@SiO2 core–shell nanoparticles with enhanced visible-light photoactivity," *Dalton Transactions*, vol. 42, no. 38, p. 13948, 2013.

[153] J. F. Lutsko, V. Basios, G. Nicolis, T. P. Caremans, A. Aerts, J. A. Martens, C. E. A. Kirschhock, and T. S. van Erp, "Kinetics of intermediate-mediated self-assembly in nanosized materials: A generic model," *The Journal of Chemical Physics*, vol. 132, no. 16, p. 164701, 2010.

[154] J. Gaâzo, I. Bersuker, J. Garaj, M. Kabešová, J. Kohout, H. Langfelderová, M. Melník, M. Serator, and F. Valach, "Plasticity of the coordination sphere of copper(II) complexes, its manifestation and causes," *Coordination Chemistry Reviews*, vol. 19, no. 3, pp. 253–297, 1976.

[155] P. Sharrock and M. Melník, "Copper(II) acetates: from dimer to monomer," *Canadian Journal of Chemistry*, vol. 63, no. 1, pp. 52–56, 1985.

[156] M. Shöâeé, J. R. Agger, M. W. Anderson, and M. P. Attfield, "Crystal form, defects and growth of the metal organic framework HKUST-1 revealed by atomic force microscopy," *CrystEngComm*, vol. 10, no. 6, pp. 646–648, 2008.

[157] D. W. Marquardt, "An Algorithm for Least-Squares Estimation of Nonlinear Parameters," *Journal of the Society for Industrial and Applied Mathematics*, vol. 11, no. 2, pp. 431–441, 1963.

[158] R. Bro and S. De Jong, "A fast non-negativity-constrained least squares algorithm," *Journal of Chemometrics*, vol. 11, no. 5, pp. 393–401, 1997.